New Passive Methodology

for Power Cable Monitoring and Fault Location

by

Youngdeug Kim

A Dissertation Presented in Partial Fulfillment
of the Requirements for the Degree
Doctor of Philosophy

Approved July 2015 by the
Graduate Supervisory Committee

Keith Holbert, Chair
Antonia Papandreou-Suppappola
Gerald Heydt
George Karady

ARIZONA STATE UNIVERSITY

August 2015

ABSTRACT

The utilization of power cables is increasing with the development of renewable energy and the maintenance replacement of old overhead power lines. Therefore, effective monitoring and accurate fault location for power cables are very important for the sake of a stable power supply.

The recent technologies for power cable diagnosis and temperature monitoring system are described including their intrinsic limitations for cable health assessment. Power cable fault location methods are reviewed with two main categories: off-line and on-line data based methods.

As a diagnostic and fault location approach, a new passive methodology is introduced. This methodology is based on analyzing the resonant frequencies of the transfer function between the input and output of the power cable system. The equivalent pi model is applied to the resonant frequency calculation for the selected underground power cable transmission system.

The characteristics of the resonant frequencies are studied by analytical derivations and PSCAD simulations. It is found that the variation of load magnitudes and change of positive power factors (i.e., inductive loads) do not affect resonant frequencies significantly, but there is considerable movement of resonant frequencies under change of negative power factors (i.e., capacitive loads).

Power cable fault conditions introduce new resonant frequencies in accordance with fault positions. Similar behaviors of the resonant frequencies are shown in a transformer (TR) connected power cable system with frequency shifts caused by the TR impedance.

The resonant frequencies can be extracted by frequency analysis of power signals and the inherent noise in these signals plays a key role to measure the resonant frequencies. Window functions provide an effective tool for improving resonant frequency discernment. The frequency analysis is implemented on noise laden PSCAD simulation signals and it reveals identical resonant frequency characteristics with theoretical studies.

Finally, the noise levels of real voltage and current signals, which are acquired from an operating power plant, are estimated and the resonant frequencies are extracted by applying window functions, and these results prove that the resonant frequency can be used as an assessment for the internal changes in power cable parameters such as defects and faults.

ACKNOWLEDGMENTS

I always thank God for this invaluable bonding with my Ph.D. advisor Dr. Keith E. Holbert. He guided me here with his hearty kindness and professional knowledge for this dissertation. I have learned how to think, how to approach, how to study and how to complete research challenges from his studious experiences.

I am very grateful to my committee members: Dr. George Karady, Dr. Gerald Heydt and Dr. Antonia Papandreou-Suppappola. They provided great help with their professional points of view, such as system modeling and analysis, noise estimation, frequency analysis, etc.

Even though it was for just a few months, Sudarshan Govindarajan shared and studied together in this research and gave me lots of good ideas. I would like to thank SRP (Salt River Project) for supporting this research and give special thanks to colleagues at Sihwa tidal power plant for acquiring real data.

The greatest support was an encouragement from my parents and parents-in-law and I will never forget your love. Finally, I want to express my deepest gratitude to my wife, YooLee, for constant trust on me and to my lovely kids, WooGyeom and GaYeon, for healthy gifts of big smiles and happiness.

TABLE OF CONTENTS

Page

CHAPTER Page

LIST OF TABLES

LIST OF FIGURES

Figure Page

Figure Page

Figure Page

Figure Page

Figure Page

LIST OF SYMBOLS

$C_d A_L$	Leakage Size in A Water Pipe System
A_k	Pipe Cross-sectional Area
E_i	Incident Signal Voltage
E_r	Reflected Signal Voltage
H_C	Transfer Function for Cable Power System
H_{CF}	Transfer Function for Faulted Cable Power System
H_{CL}	Transfer Function for Load Connected Cable Power System
H_T	Transfer Function for TR Connected Cable Power System
H_{TF}	Transfer Function for Faulted TR Connected Cable Power System
H_W	Transfer Function for Water Pipe System
I_0	Zero-sequence Current
I_R	Current at Load Side
I_S	Current at Source Side
I_{pre}	Pre-fault Current
I_{sup}	Superposition Current
L_{max}	Maximal Cable Length
L_{min}	Accuracy of Distance Measurement
M_{peak}	Peak Value of Reference Signal
N_L	Noise Level
N_{cyc}	Number of Cycles
N_{fr}	New Resonant Frequencies in Faulted System

N_{seg}	Number of Data Segments
P_{STD}	Percentage of Noise Standard Deviation to the Reference Signal Peak
R_{75}	Resistance at 75°C
R_{AC}	Equivalent Resistance in AC Circuit Condition
R_{DC}	Equivalent Resistance in DC Circuit Condition
R_F	Fault Resistor
R_k	Frictional Resistance Term in Pipeline
$S_{XX}(f)$	Power Spectral Density of White Noise
S_x	Power Spectral Density
V_R	Voltage at Load Side
V_S	Voltage at Source Side
X_m	Cable Reactance
Z_{0m}	Zero-sequence Cable Impedance
Z_{1m}	Positive-sequence Cable Impedance
Z_F	Impedance at The Discontinuity
Z_c	Characteristic Impedance
Z_{in}	Equivalent Impedance
Z_m	Cable Impedance
d_{bund}	Distance between Bundles
e_r	Dielectric Constant
$f_{r_{Cn}}$	n^{th} Resonant Frequency in Cable Power System
f_{rB1}	Reference the First Resonant Frequency

f_{rB2}	Reference the Second Resonant Frequency
fr_{CFn}	n^{th} New Resonant Frequency in Faulted Cable Power System
f_{rL1}	New First Resonant Frequency
f_{rT1}	The First Resonant Frequency of TR Power System
f_{rT2}	The Second Resonant Frequency of TR Power System
fr_{Tn}	n^{th} Resonant Frequency in TR Connected Cable Power System
f_{st}	Standing Wave Frequency
k_p	Proximity Effect Factor
k_s	Skin Effect Factor
r_0	Conductor Radius, Cable Radius
r_{bund}	Equivalent Radius of the Conductor
$r_{s,out}$	Sheath Outer Radius
r_{xn}	Cross-correlation between Discrete Incident Signal and Noise
r_{xx}	Autocorrelation of the Discrete Incident Signal
r_{xy}	Cross-correlation
t_d	Time Difference between t_A and t_B
v_c	Speed of Light
v_p	Propagation Velocity, Wave Speed
$x_F(\omega)$	Fourier Transform of Random Time Signal $x(t)$
ε_0	Vacuum Permittivity
ε_{se}	Relative Permittivity of Insulation between Sheath and Earth
μ_0	Vacuum Permeability

μ_k	Propagation Parameter
σ^2	Signal Variance
τ_p	Surge Propagation Time
$\otimes$	Convolution
GMD	Conductor Geometrical Mean Distance
GMR	Conductor Geometric Mean Radius
$h(n)$	Transfer Function of Cable System
npts	Number of Data Points
sft	Shift Effect of Resonant Frequency by Transformer
t	Time
ΔP_{max}	Maximum Fault Location Error
Δf	Frequency Step Size, Frequency Resolution
τ	Time Delay, Translation in Time-Frequency Analysis
E	Expected Value
D	Distance between Phases
$M(n)$	n^{th} Datum in Reference Signal, MAVG
P	Distance to Fault
P	Distance to Fault Position, Fault Location
$R(n)$	n^{th} Datum in Real Signal
STD_N	Standard Deviation of Noise Level
T	Angle between Zero-sequence Current and Fault Current
$Tan\ \delta$	Dissipation Factor
$W(t)$	Window Function

d	Distance between Conductors
g	Gravitational Acceleration
l	Cable Length, Water Pipeline Length
n	Data Point
p	Per Unit Distance to Fault Point
r	Outer Radius of Core Conductor
s	Scaled Parameter
$x(t)$	Random Time Signal
y	Constant ($y = 1$ for 1, 2, 3 Core Cables, y=1.5 for Pipe-Type Cables)
Δt	Sampling Interval or Sampling Time Interval
$\Psi(t)$	Mother Wavelet
α	Attenuation Constant
β	Phase Shift
γ	Propagation Constant
$\delta(\tau)$	Unit Impulse Sequence
ρ	Reflection Coefficient
ω	Angular Frequency, Angular Speed

LIST OF ABBREVIATIONS

CT	Current Transformer
CWT	Continuous Wavelet Transform
DFT	Discrete Fourier Transform
DWT	Discrete Wavelet Transform
EMTP	Electromagnetic Transients Program
FDR	Frequency Domain Reflectometry
FFT	Fast Fourier Transform
FRD	Frequency Response Diagram
FT	Fourier Transform
GPS	Global Positioning System
HMRA	Harmonic Modal Resonant Analysis
LPC	Linear Prediction Coding
MAVG	Reference Signal for Noise Estimation by Moving Average Method
MIM	Multiple Impulse Method
PD	Partial Discharge
PMU	Phasor Measurement Unit
PSCAD	Power Systems Computer Aided Design
PSD	Power Spectral Density
PT	Potential Transformer
SFRA	Sweep Frequency Response Analysis
STFT	Short Time Fourier Transform

TDR	Time Domain Reflectometry
TFDR	Time Frequency Domain Reflectometry
TR	Transformer
WT	Wavelet Transform

CHAPTER 1

INTRODUCTION

Today, underground power systems are increasingly becoming a reliable alternative to overhead lines with continuing development of cable diagnosis and fault location techniques.

The main technologies for cable diagnosis are evaluating partial discharge, dissipation factor (tan δ), withstand voltage, DC leakage current, polarization / depolarization current and recovery voltage [1]. Most of these methods require offline testing conditions, specific measuring devices and highly experienced technicians. Even though some online partial discharge monitoring systems have been commercialized, they still suffer from the limitation of capturing tiny signals or acoustic detection of partial discharge.

Fault location within underground power cables is relatively difficult because of their inaccessibility. To overcome this challenge, there have been various improvements in power cable fault location techniques. These methods are based on mostly time domain analysis, such as fault voltage and current detection, signal arrival time calculation, infrared imaging, radar, time domain reflectometry, acoustic and pressure waves, and a variety of high frequency characteristics [2].

Recently, researchers have focused on the frequency domain signal analysis methods for fault location, because these approaches are believed to yield high accuracy without additional measurement devices and without disconnection from the power grid [3] [4] [5]. Fault location based on travelling wave natural frequency analysis is a good

example [6] [7] [8]. But most of these approaches are at the stage of studies and have not yet been developed fully for real field application.

Now, some effective and accurate approaches that can monitor and locate cable faults using online signals are needed to satisfy the demand for high qualified power service. Based upon these needs, we turned our attention to the resonant frequencies, which are uniquely related to electrical parameters of the cable. Therefore, this dissertation introduces a new passive methodology for power cable health monitoring and power cable fault location based on analyzing the behavior of power system resonant frequencies.

First in Chapter 2, there is a short review of recent power cable diagnosis and monitoring techniques. Also, cable fault location methods are described on the basis of two main categories as on-line data based and off-line data based methods. This chapter will explain the limitations of recent technologies and differentiate our new methodology.

Chapter 3 introduces a new passive methodology with helpful examples, which use resonant frequency characteristics. This chapter studies mainly about behavior of power system resonant frequency. The basic theoretical background on the transmission system model and the transfer function is reviewed then the behaviors of resonant frequency under various load conditions and fault positions are studied with theoretical approaches. Primarily, these studies model the power cable transmission system, then they are expanded to a transformer connected power cable transmission system, which can be considered as a better representation of a real power system.

Chapter 4 verifies theoretical studies about resonant frequency behaviors by frequency-impedance calculation and frequency analysis on power signals using PSCAD

computer simulations. This chapter shows the contribution of noise in the signals to frequency analysis and the effectiveness of window functions for improving resonant frequency discernment.

The resonant frequencies of the power system are validated with real data in Chapter 5. The noise level in the real data is estimated and it proves that the resonant frequency can be monitored effectively in the real power system by applying the proper window function. Finally, Chapter 6 gives conclusions and proposes future works.

CHAPTER 2

REVIEWS OF POWER CABLE DIAGNOSIS AND FAULT LOCATION

With increasing demand for underground power cable transmission and distribution systems, power cable diagnosis and fault location has become an attractive subject in power system engineering. This chapter presents widely used cable diagnosis techniques such as the dissipation factor (Tan δ) test and partial discharge test. Also, a power cable temperature monitoring system using fiber optics is described as an example of cable monitoring technology. The cable fault location methods are reviewed on the basis of two main categories as on-line and off-line data based methods. In addition, their theories and limitations are presented.

2.1 Power Cable Diagnosis

The proper measurement of defects can reduce the failure rate of power cables. The cable diagnostic technologies capable of assessing defect characteristics are partial discharge, dissipation factor (Tan δ), withstand voltage, DC leakage current, polarization / depolarization current and recovery voltage. Some of these are described below.

2.1.1 Dissipation Factor (Tan δ) Test

Tan δ measures the degree of real-power dissipation, i.e., losses in a dielectric material. The value of tan δ increases with increasing insulation losses by the spreading water trees. The Tan δ is measured by the phase difference between input AC voltage and resulting current, and the test is carried out in the offline condition with an energizing source of 0.1 Hz or 60 Hz [1].

The equivalent circuit and phasor diagram are shown in Fig. 2-1 and their parameters are testing voltage V, resistance R (represents the insulation losses), capacitance C, leakage current I, loss current I_R, charging current in I_C, and δ is the phase angle between I_C and I.

$$\text{Tan } \delta = \frac{I_R}{I_C} = \frac{V/R}{V/(1/\omega C)} = \frac{1}{\omega RC} \tag{2-1}$$

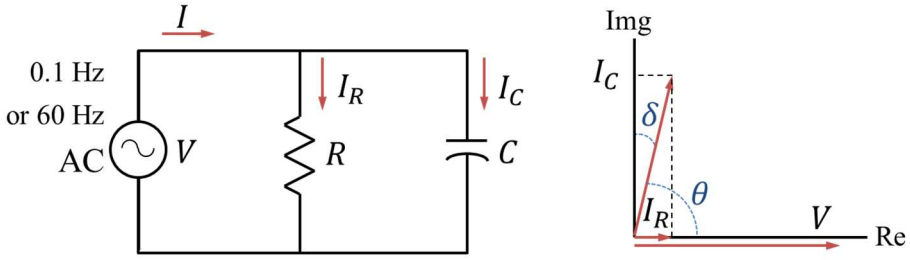

Fig. 2-1 Equivalent Circuit for Tan δ Test and Phasor Diagram [9].

The Tan δ of a new cable is quite small, typically less than 0.0001 [10], and increases during the lifetime due to the natural degradation or the increment of water tree defects.

As a limitation, the Tan δ gives information only about the average condition of cable. Thus, when the high density of water trees exist only in a partial region of the cable, their effect will be diminished in an overall measurement. The records of several years Tan δ test should be kept for the trend analysis, and decision for the replacement of cable.

2.1.2 Partial Discharge Testing

The partial discharge is an evidence of the cable degradation, and the test equipment detects its transient electrical or acoustic signals.

The electrical detection method measures μV and μA signals from the discharge site using potential transformers in form of capacitive dividers. Fig. 2-2 shows an example of an electrical partial discharge measurement, whose red colored parts represent partial discharge and others are noises.

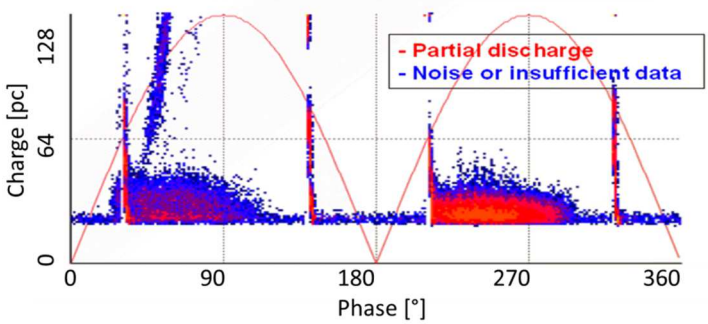

Fig. 2-2 Example of a Partial Discharge Measurement [11].

The acoustic detection method measures the emitted high frequency sound wave using ultrasonic microphone sensors that are placed close to the possible partial discharge sites, such as joints or terminations of the cable.

Because the cable acts as a low pass filter, the pulse signal from partial discharge can be attenuated and large parts of its frequency content can be lost in the propagation to the detector. The typical bandwidth of testing equipment is several hundreds of kHz up to several tens of MHz [12] [13].

The measurement of partial discharge requires specialized devices and trained technicians. It can be affected by the type and location of defects, testing voltage and frequency, type of insulation and ambient noise. Even small noises can affect the proper measurement due to the intrinsic tiny magnitude of the partial discharge signal [14].

The partial discharge test is a stochastic process, thus it is difficult to interpret. Unfortunately, the indication from interpretation is simply “good” or “very bad”

conditions as a pass or fail test. Even in some proposed methods, such as recorded PD, signal pattern analysis and comparison can improve their assessment precision, but they do not give an exact answer about where defects exist.

2.2 Power Cable Monitoring

There are a few online cable monitoring systems based on partial discharge detection in the vicinity of the cable joints or terminations. These systems detect the acoustic waves by ultrasonic sensors or light flash by the fluorescent sensors, but these signals are vulnerable to noise and are attenuated easily over long distances. Therefore, some methods use optic networks and sensors.

Distributed temperature monitoring is one commercialized power cable monitoring system. Continuous overload produces overheating and deformation of a power cable and leads to a breakdown, thus the temperature of a cable is a good factor for monitoring power cable operational conditions.

The typical optical temperature sensor is based on stimulated Brillouin scattering and its mechanism is illustrated in Fig. 2-3. The input signal is called a pump wave and its scattering process generates a Stokes wave. The pump wave produces an acoustic wave in the medium by the electrostriction process, and the interaction between pump wave and acoustic wave creates the back propagating Stokes wave.

When the input power reaches a Brillouin scattering threshold level, a significant portion of the optical signal is back-scattered because of the changed refractive index. An example of the measured Brillouin gain spectra in a single mode fiber at different temperatures is shown in Fig. 2-4.

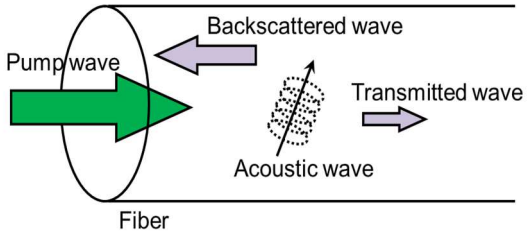

Fig. 2-3 Mechanism of Stimulated Brillouin Scattering [15].

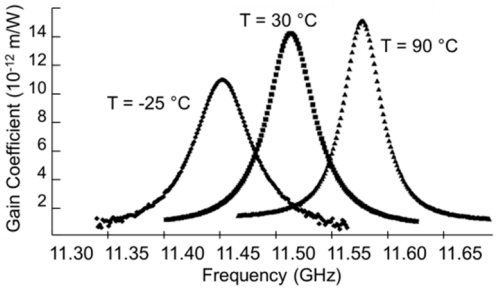

Fig. 2-4 Brillouin Gain Spectra at Different Temperatures [16].

The gain coefficient increases with temperature increment with a good linear dependency and this feature is used for the temperature monitoring system. The optical sensor can have an accuracy of ±1°C and its range is more than 20 km [16]. Fig. 2-5 shows the embedded optical fibers in a screen layer of the power cable.

The dielectric property, immunity to electromagnetic interface and low marginal cost has led to increased usage of the fiber optic in power cable monitoring and optical communication. An example of temperature monitoring is shown in Fig. 2-6, and this displays distinct features of distributed temperature, but it is hard to assess the cable health based on defects such as water trees, voids, partial discharge, etc.

Fig. 2-5 Fiber Optic Embedded XLPE Cable [17].

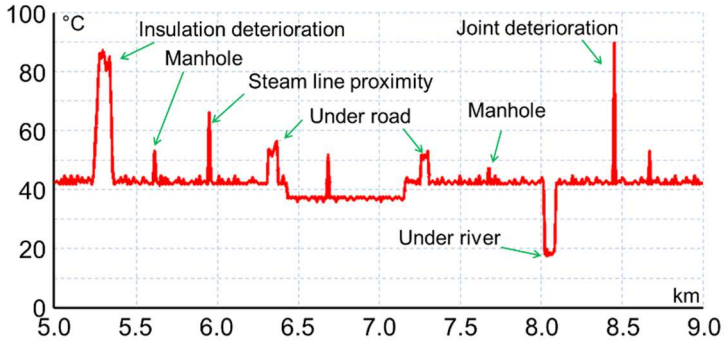

Fig. 2-6 Example of Power Cable Temperature Traces [18].

2.3 Cable Fault Location

There has been continuous interest in power cable fault location technology with remarkable improvements in accuracy and diverse methods are proposed with different theoretical background and mechanisms.

These methods can be classified as on-line data based methods and off-line data based methods in terms of how the signal for fault location is obtained. The on-line data based method uses recorded fault signals while the power cable is connected to the power system. In contrast, the off-line data based method injects an external testing signal (e.g. impulse, sine wave, etc.) into a power cable to locate faults and sometimes this method is called post fault circuit analysis.

Most of the off-line data based methods ensure high accuracy for fault location and appropriate methods can be selected depending on the condition of the power cable installation, size, structure, length, etc. Some methods (e.g., TDR (Time Domain Reflectometry), FDR (Frequency Domain Reflectometry) and MIM (Multiple Impulse Method)) require highly experienced skills. Some methods, like the thumpers method, can cause serious damage to the cable. These methods can be used together to attain higher accuracy.

2.3.1 Off-line Data Based Methods

Usually, the A frame method, bridge method, TDR method, MIM method, and thumpers method are used for cable fault location and these ensure a high accuracy. But these methods require additional measurement devices and time consuming processes.

This document reviews some widely used fault location methods such as TDR, FDR, TFDR (Time Frequency Domain Reflectometry) and PD (Partial discharge) method.

(a) TDR method

TDR is more convenient and accurate for cables in the duct where the path to ground may not be at the fault point but rather at the unrelated duct damage (i.e., crack or joint). TDR transmits a pulse of energy that propagates along a cable, and a portion of this energy will reflect back to the sending end whenever it passes a relative change in the impedance of the cable [19].

The transmission cable is assumed to consist of a continuous structure of R, L and C's, and the phase shift and attenuation are defined by the propagation constant, γ as

$$\gamma = \alpha + j\beta = \sqrt{(R + j\omega L)(G + j\omega C)} \tag{2-2}$$

Where, α is attenuation in nepers per unit length, and β is phase shift in radians per unit length. The voltage travels down the line at the propagation velocity v_p, which can be defined in terms of β

$$v_p = \frac{\omega}{\beta} \tag{2-3}$$

The propagation velocity approaches the speed of light for air dielectric. When the dielectric constant is e_r, the propagation velocity is

$$v_p = \frac{v_c}{\sqrt{e_r}} \tag{2-4}$$

The basic TDR setup and its functional block diagram are shown in Fig. 2-7. The step generator produces a positive-going incident wave that is applied to the cable under test. If the load impedance is equal to the characteristic impedance of the cable, no wave is reflected and only the incident voltage step is recorded [19].

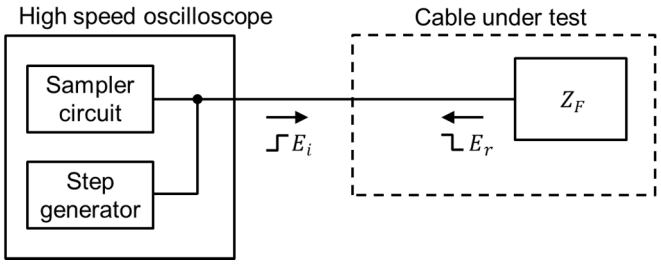

Fig. 2-7 Functional Block Diagram for TDR [19].

The reflected voltage wave will appear on the oscilloscope display algebraically added to the incident wave as right side of Fig. 2-8. The ratio of the reflected wave to the incident wave, called the voltage reflection coefficient, ρ is related to the cable impedance as

$$\rho = \frac{E_r}{E_i} = \frac{Z_F - Z_c}{Z_F + Z_c} \tag{2-5}$$

where E_i is incident signal voltage, E_r is reflected signal voltage, Z_c is the characteristic impedance of the cable and Z_F is impedance at the discontinuity. At the limits: $\rho = 1$ for an open circuit, and $\rho = -1$ for a short circuit.

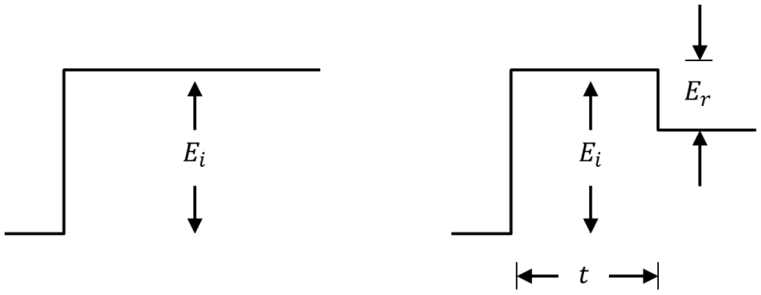

Fig. 2-8 Oscilloscope Display when $E_r = 0$ (left) and $E_r \neq 0$ (right) [20].

The reflected wave can be easily identified, since it is separated in time from the incident wave. This time interval of incident and reflected signal, t can be used to determine the distance, P to the point of the impedance discontinuity as follows

$$P = v_p \frac{t}{2} \tag{2-6}$$

A wider pulse will have more energy and be able to test longer distances and resolve smaller faults. A narrower pulse which has a higher fundamental frequency gives a more useable resolution, but no more accuracy [21].

A commercial TDR device and its application are shown in Fig. 2-9. The graph shows two traces and one channel that has 2 peaks indicates an open circuit at approximately 1200 meters and the other an open circuit at 629.6 meters.

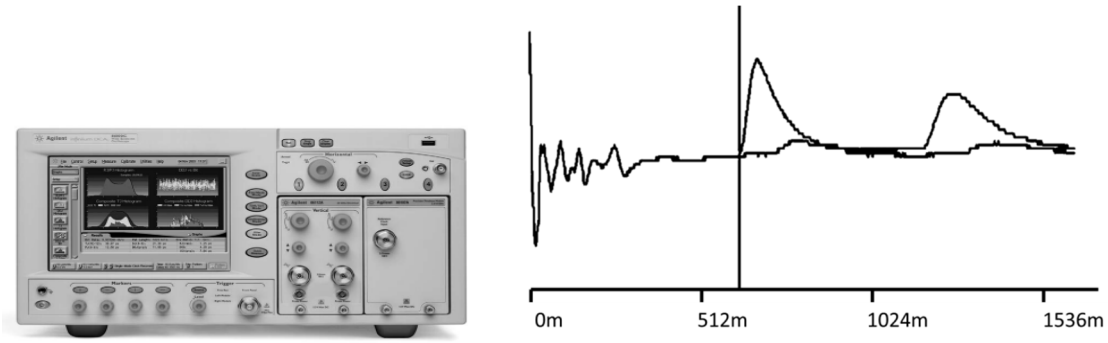

Fig. 2-9 Commercial TDR Device and its Application [20].

As a limitation of TDR, if the fault impedance is not small enough compared to the insulation impedance of the healthy parts, the low voltage impulse sent out by the TDR is not reflected at the fault position. Also, the accuracy of distance is greatly dependent on the accuracy of propagation velocity selected.

These drawbacks of the TDR method can be improved by the MIM method, which injects multiple (usually five) low voltage pulses. The simultaneous displays of multiple fault graphs are compared to a healthy trace and it leads to the highest precision for fault location. This method is known as so efficient as to locate up to 98% of cable faults [22].

(b) FDR method

The FDR and TDR method are based on the same basic ideas except the way for estimating the time interval between incident and reflected signal. The FDR measures phase shift between the incident and reflected signals to determine the cable length and the fault position. Owing to developments of filtering and digital signal processing techniques, The FDR method is regarded as more accurate than the TDR method [23].

A portion of the transmitted sweep signal will be reflected back to the transmitter with the same frequency as the sweep signal but different in phase. The resulting signal will appear as standing waves on the frequency sweep, and the peaks of individual cycles can be translated to distance to the fault through the following equation [24]:

$$P = \frac{1}{f_{st}} \frac{v_p}{2} v_c \tag{2-7}$$

Where f_{st} is the frequency of the standing wave.

Because of the round trip delay, the reflected signal has a phase difference to the transmitted signal and the phase difference increases with frequency increment.

The range of the system is limited by the Nyquist Criterion, meaning that the decaying sinusoid trace must be sampled more than twice per period in order to obtain an accurate Discrete Fourier Transform (DFT). The maximal cable length, L_{max} can be defined by the frequency step size Δf,

$$L_{max} = \frac{v_p}{4\Delta f} \tag{2-8}$$

The accuracy of the distance measurement (L_{min}) is decided by the resolution of the DFT (number of points in the DFT, npts) as [23],

$$L_{min} = \frac{v_p}{2 \cdot \text{npts} \cdot \Delta f} \tag{2-9}$$

For instance, when Δf = 20 kHz, npts = 2^{11} = 2048 and $v_p = 2/3$ of the speed of light, the accuracy of this system is 2.44 m.

By Fourier transform, the reflection distance can be determined from the variation rate of the trace including reflection magnitude and phase angle. As an example of a measured reflectogram of the FDR method, Fig. 2-10 demonstrates the reflection phase of a bad splice at 1230 m and open circuit at the end (2033 m) of the cable [25].

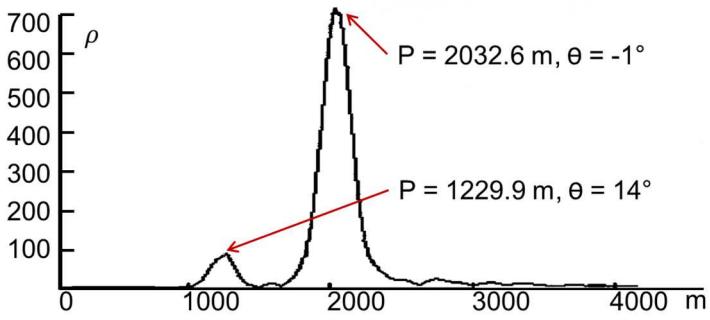

Fig. 2-10 Example of a Reflectogram for the FDR Method [25].

The FDR method uses the expensive directional coupler to separate the incident and reflected signals and the fault type cannot be exactly distinguished.

(c) TFDR method

The idea of the TFDR method originates from a similar principle as the TDR method except the incident signal used is a linear chirp signal with a Gaussian envelope which is suitable for the time-frequency domain analysis. A coupler is used to separate the received signal coming from the cable.

For locating faults, the cross-correlation between the incident and reflected signals, r_{xy} can be employed as computed via [23]

$$r_{xy}(n) = r_{xx}(n) \otimes h(n) + r_{xn}(n) = r_{xx}(n) \otimes h(n) \tag{2-10}$$

where $\otimes$ denotes convolution; n is the shift parameter number; r_{xx} is the autocorrelation of discrete incident signal; $h(n)$ is the transfer function of the cable system, which is modeled as a linear filter; r_{xn} is the cross-correlation between discrete incident signal and noise, its value is zero in this case.

The TFDR method is not sensitive to noise and it is able to detect the weak reflected signals better than TDR, but the additional equipment such as the coupler and ultra-wide band signal generator makes it more expensive. Because the attenuation is greater for higher frequencies, the TFDR method is not suitable for long length cable fault location and this method hardly distinguishes fault types.

(d) Partial discharge (PD) method

PD is caused by various defects in a cable such as voids, shield protrusions, contaminants, advanced stages of water tree, electrical tree, etc., and these are known to be the main causes of the breakdown in insulation materials [26].

The PD can be modeled as parallel capacitors for bulks of insulation (C_a', C_a'') and a defect (C_c for void and C_b', C_b'' for parts of insulation in series) as shown in Fig. 2-11(a), and its equivalent circuit is shown in Fig. 2-11(b).

By increasing the terminal voltage V_a, the capacitor C_c is charging and the voltage across the void, V_c, increases. When the V_c reaches an electric breakdown voltage inside the void, the switch S is closed and the discharge current i_c flows for a very short time and the resistor R_c limits the magnitude of i_c. After i_c is extinguished, the C_c starts to charge up and the same process repeats for a next partial discharge [27].

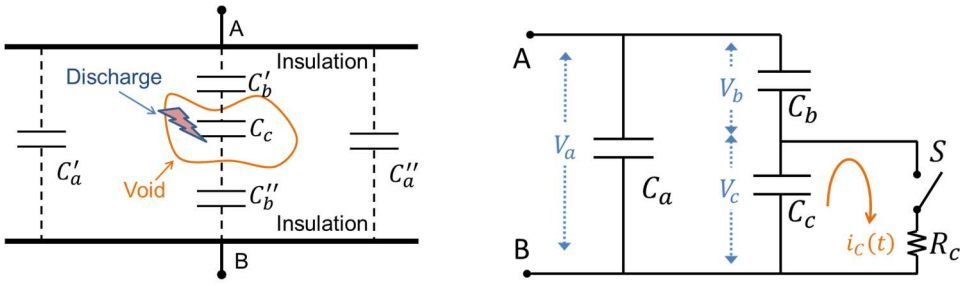

(a) (b)

Fig. 2-11 PD Model (a) and Equivalent Circuit (b) [27].

Usually PD lasts for only a few nanoseconds and results in electromagnetic spectrum emissions including visible light, heat, sound and high radiofrequency. The magnitude of the apparent charge of each PD and the frequency of occurrence are important factors for evaluating the severity of PD activity. The trending of these factors over time can be an indicator for electrical failure or necessity of preventative maintenance [28].

The PD measurements are taken at the point where the cable shields are grounded, such as each termination and splice. In certain cases that do not have shield groundings, we can select a relative PD location, where the highest magnitude and frequency pulses are found or simply by acoustic detection, which is tuned to detect 10 to 1000 kHz ultrasonic sounds. The accuracy can be improved by applying special noise reduction filters to the measurement system.

2.3.2 On-line Data Based Methods

Usually, the off-line data based fault location methods are slow, demand human control and cannot detect intermittent faults. Therefore, the usage of fault generated signals in fault location, which is categorized as on-line data based fault location methods, are highly reasonable.

Most electrical fault detection methods are based on analyzing different characteristics of currents and voltages in time, frequency, and time-frequency domains. To make the detection algorithm reliable, these currents and voltages must be sampled at a sufficiently high rate, at least several samples per cycle.

Recently, most microprocessor-based network protectors contain such data processing abilities. For example, one phasor measurement unit (PMU) SIMEAS R-PMU (a product from Siemens) has 192 samples per cycle (86.8 μs sampling interval) and one digital protection relay for ultra-high voltage distribution system GIPAM 2000 (a product from LS industrial) has 32 samples per cycle (520.83 μs sampling interval).

There are many categories of cable fault location methods based on the adopted transmission system and fault models, signal measurement, data analysis, and so on [29] [30] [31]. They can be classified into two main categories as impedance-based methods and traveling-wave methods [32]. Sometimes they are subdivided as one-end and two-end methods, or five types (A, B, C, D, and E) [33] [34].

(a) Impedance-based methods

The impedance-based fault location methods are widely used because of their fast response, simple and easy application, stability and economic benefits. These methods use the measured voltage or current data with already known the cable impedance parameters and can be divided into one-ended methods and two-ended methods.

One-ended impedance-based methods use a simple algorithm. They do not require communication channels and remote data. The simple reactance method, Takagi method and the modified Takagi method that use zero-sequence current with angle corrections are commonly used in the field.

Two-ended methods can be more accurate, but require data from both terminals. The two-ended negative-sequence method is commonly used in the field [35].

Simple reactance method

The simple reactance method calculates the fault location from the apparent impedance seen from one end of the cable. This method is based on the measurement of a short circuit loop at the power frequency, in a solidly grounded network.

After measuring the apparent impedance, the ratio of the measured reactance to the total reactance of the whole power cable transmission system is determined. This ratio is proportional to the fault distance. It is assumed that the fault resistor is in phase, the fault current flows from the measurement station, and the load prior to the fault is zero. The phase-to-ground voltages and currents in each phase must be measured to locate all fault types, and a one-line diagram of line fault is provided in Fig. 2-12.

From Fig. 2-12, the voltage drop at the A side V_A is

$$V_A = pZ_m I_A + R_F I_F \tag{2-11}$$

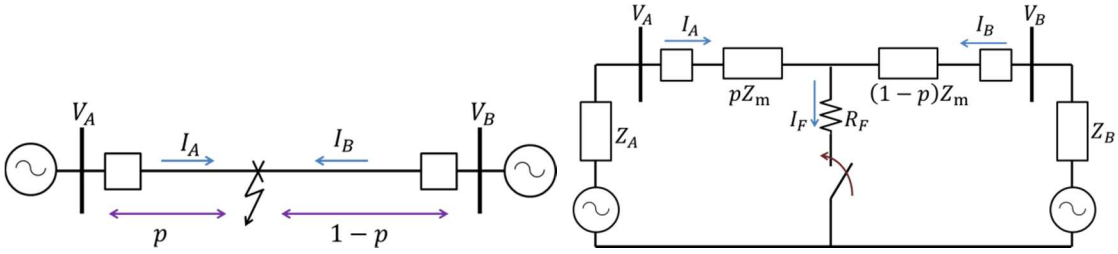

Fig. 2-12 One-line Diagram and Circuit for Line Fault [35].

The simple reactance method divides all terms by the current I_A that the fault locator measured and ignores the $(R_F \cdot I_F/I_A)$ term. Then it takes the imaginary part to solve for fault point p,

$$\mathrm{Im}(V_A/I_A) = \mathrm{Im}(pZ_m) = pX_m, \qquad p = \frac{\mathrm{Im}(V_A/I_A)}{X_m} \tag{2-12}$$

If $\angle I_A = \angle I_F$ or $\angle R_F = 0$, the error will be 0.

For an R-phase to ground fault

$$V_A = V_{r-g}, \qquad I_A = I_r + k \cdot 3I_0 \tag{2-13}$$

where k is $(Z_{0m} - Z_{1m})/3Z_{1m}$, Z_{0m} is the zero-sequence cable impedance, Z_{1m} is the positive-sequence cable impedance, p is the per unit distance to fault, I_0 is the zero-sequence current, and the voltage and current on R-phase are V_r and I_r respectively.

The accuracy of fault location is highly dependent on the impedance calculation of the transmission system. Commonly this impedance is calculated based on equations developed by J.R. Carson, et al. in 1926 [36] and an accuracy within 1% has been claimed for the calculated impedances (Eriksson, et al. [37]). The accuracy of the impedance calculation can be improved by using a high sampling rate recorder.

In spite of the accurate impedance calculation, the fault location accuracy can be affected by unknown variables, such as the combined effect of fault resistance and load, zero-sequence mutual coupling, system nonhomogeneity, system infeeds (remote or the third terminal infeed, tapped load with zero-sequence source), inaccurate relay measurement, inaccurate instrument transformer or line parameters, most notably the amount of fault resistance [33].

It is often difficult to obtain accurate zero-sequence impedance, because it is affected by earth resistivity. A 20% error in the zero-sequence impedance can cause a 15% error in the fault location. In addition, this impedance is not uniformly distributed along the transmission system length [35].

Takagi method

Takagi method provides an improved solution compared to the simple reactance method by removing the fault resistance effect. The Takagi method is based on pre-fault and fault data. Define superposition current, I_{sup} to find a term in phase with the pre-fault current, I_{pre}

$$I_{sup} = I_A - I_{pre} \tag{2-14}$$

multiply the two sides of Eq. (2-14) with the conjugate of I_{sup}, that is I_{sup}^*, and only take the imaginary part,

$$\mathrm{Im}\left(V_A I_{sup}^*\right) = \mathrm{Im}\left(pZ_m I_A I_{sup}^*\right) + \mathrm{Im}\left(R_F I_F I_{sup}^*\right) \tag{2-15}$$

When I_{sup} is in the same phase with I_F, the part related to I_F is zero and can be removed,

$$p = \frac{\mathrm{Im}\left(V_A I_{sup}^*\right)}{\mathrm{Im}\left(Z_m I_A I_{sup}^*\right)} \tag{2-16}$$

The accuracy depends on this assumption, that the angle of I_A and I_F is the same. In other words, the accuracy of Takagi method is mainly determined by the angle difference between the sending end current and the fault current [35] [38].

Modified Takagi method

The modified Takagi method can improve the Takagi method by using zero-sequence current ($3 \cdot I_{0A}$) for ground faults instead of the superposition current. This method does not require pre-fault data and allows for angle correction.

If the system source impedances are known, the zero-sequence current can be adjusted by angle T to correct for a non-homogeneous system and result in an improvement of fault location [35].

According to Fig. 2-13, the equation for the current angle correction T can be derived based on the current division rule as

$$\frac{I_F}{3I_{0A}} = \frac{Z_{0A} + Z_{0m} + Z_{0B}}{(1-p)Z_{0m} + Z_{0B}} = A\angle T \tag{2-17}$$

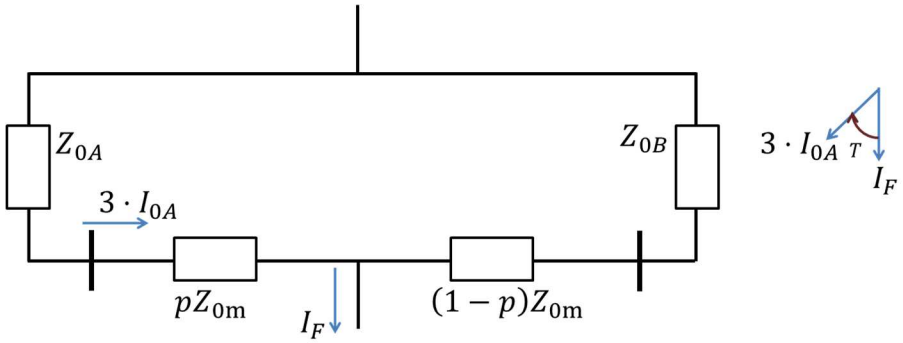

Fig. 2-13 Zero-sequence Current Angle Correction [35].

where T is the angle between zero-sequence current I_{0A} and fault current I_F. The distance to the fault can be calculated as follows,

$$p = \frac{\mathrm{Im}\left(3V_A I_{0A}^* e^{-jT}\right)}{\mathrm{Im}(3Z_{1m} I_A I_{0A}^* e^{-jT})} \tag{2-18}$$

Negative-sequence method

The negative-sequence method is more precise compared with the one-ended method and the effects of zero-sequence impedance infeed can be eliminated. This approach uses negative-sequence quantities from all cable terminals to locate unbalanced faults.

The negative sequence circuit is shown in Fig. 2-14. Unlike one-end methods, the negative-sequence method requires the source impedance, but data alignment is not required because the algorithm employed at each line end uses following quantities from the remote terminal (which do not require phase alignment) [35]

- Magnitude of negative-sequence current I_2, and
- Calculated negative-sequence source impedance $Z_2\angle\theta_2$.

At sources A and B,

$$V_{2F} = -I_{2A}(Z_{2A} + pZ_{2m}) \tag{2-19}$$

$$V_{2F} = -I_{2B}(Z_{2B} + (1-p)Z_{2m}) \tag{2-20}$$

From Eq. (2-19) and Eq. (2-20),

$$I_{2B} = I_{2A}\frac{Z_{2A} + pZ_{2m}}{Z_{2B} + (1-p)Z_{2m}} \tag{2-21}$$

By taking the magnitude of both sides to avoid alignment of relay A and B data sets, and simplifying to a quadratic equation, the fault location p can be calculated.

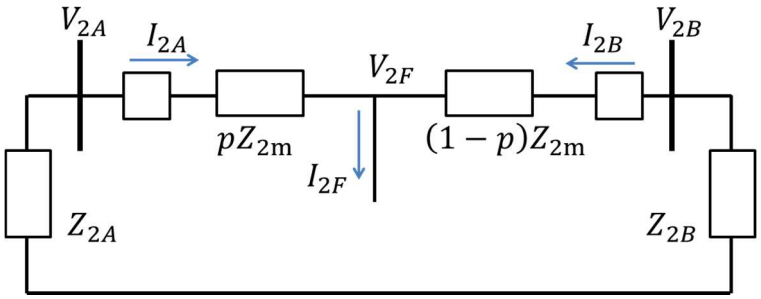

Fig. 2-14 Negative Sequence for Faulted Power Transmission System [38].

(b) Traveling-wave methods

An electromagnetic wave propagates along a transmission system with certain characteristic impedance and there is a fixed relation between the voltage and current waves.

When the wave arrives at a discontinuity, where the characteristic impedance changes (e.g., an open circuit, a short circuit, or a fault), a part of the energy is reflected and travels back. If losses are neglected, the total amount of energy in the wave remains constant.

The traveling wave-based method measures the relative time that the voltage/current wave arrives at one or two terminal ends of the power cable. The fault point is located through multiplying the relative time by the wave speed. Therefore the main challenge for a traveling wave-based method is how to effectively find this relative time component from the signals using time domain, frequency domain, or time-frequency domain analysis.

Based on signal measurement points, this method is divided into two categories as one-ended and two-ended methods.

The one-ended method measures time difference from front arrivals of the wave at one terminal end of the cable. The traveling wave caused by a fault will propagate along the cable to the terminal A with wave speed v_p as shown in Fig. 2-15. When the first arrival time of the wavefront at terminal A is t_1 and the second arrival time is t_2, the distance to the fault point is calculated as

$$P = v_p \frac{(t_2 - t_1)}{2} \tag{2-22}$$

The two-ended method measures signals at both ends of cable terminals, as shown in Fig. 2-16. The traveling waves propagate along the cable (length = l) toward the two terminal ends (A and B) with velocity of v_p. When the wave front arrival time is t_1 at terminal A and t_2 at terminal B, the distance of fault point is [39]

$$P = \frac{l - v_p(t_2 - t_1)}{2} \tag{2-23}$$

With the development of PMU (Phasor Measurement Unit), many protection schemes for transmission system are showing up including fault detection and location methods which utilize the time synchronization and telecommunication.

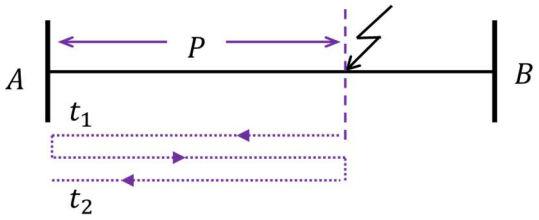

Fig. 2-15 One-ended Traveling Wave Scheme [39].

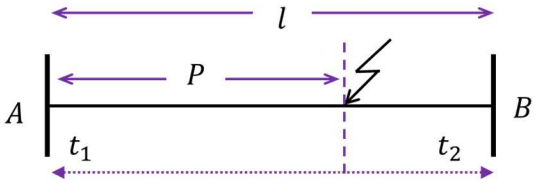

Fig. 2-16 Two-ended Traveling Wave Scheme [39].

For the accurate time tagging of events, the measurement units are synchronized to a GPS (Global Positioning System) clock, which can provide time synchronization accuracy as less than 1 μsec for all weather conditions [34], [40], [41], [42]. This equates to a fault location accuracy of ±152.4 m irrespective of line length [33].

In addition to GPS time synchronization, the advanced capability of data acquisition, signal processing techniques and communication systems motivated great interest in the traveling wave based fault location method.

As a drawback, the traveling wave is difficult to separate from oscillating noisy signal data. Furthermore, extracting accurate relative time difference of traveling wave arrivals is highly dependent on the sampling rate.

Time domain approach

Usually, the traveling wave based method uses modal decomposition (also termed as modal analysis or phase-mode transformation) techniques, which can decompose the coupled voltages and currents into a new set of modal voltages and currents. Each of the modal components can be treated independently as a single-phase line.

The Clarke's transformation matrix T can be used to obtain the ground and aerial mode signals from the three-phase transients for a fully transposed three-phase line as [34] [43]

$$T = \frac{1}{3}\begin{bmatrix} 1 & 1 & 1 \\ 2 & -1 & -1 \\ 0 & \sqrt{3} & -\sqrt{3} \end{bmatrix}, \qquad \begin{bmatrix} V_A \\ V_B \\ V_C \end{bmatrix} = T \begin{bmatrix} V_0 \\ V_\alpha \\ V_\beta \end{bmatrix}, \qquad \begin{bmatrix} I_A \\ I_B \\ I_C \end{bmatrix} = T \begin{bmatrix} I_0 \\ I_\alpha \\ I_\beta \end{bmatrix} \tag{2-24}$$

where the subscript denotes as A, B, C for phases, 0 for a ground (or earth) mode, α and β for an aerial mode.

The ground mode current I_0 is defined as the zero sequence components of the symmetrical component of the transmission system. The aerial mode current component I_α flows in phase A and one half returns in phase B and one half in phase C. I_β the aerial mode current component is circulating in phases B and C.

Each mode has different propagation velocity and different surge impedance. The ground mode is the most dependent on ground resistivity and has the lowest propagation velocity. The aerial modes are frequency invariant and favored for fault location.

The following fault location case is based on the aerial mode traveling current and cross correlation function. The correlation between samples at different distances apart can be measured by the auto-correlation coefficient as Eq. (2-25), for n pairs of samples on two variables x and y [44].

$$r_{xy}(\tau) = \frac{1}{n}\sum_{k=1}^{n}(x_{k\Delta t+\tau} - \bar{x})(y_{k\Delta t} - \bar{y}) \tag{2-25}$$

where r_{xy} is the cross correlation function of the signals x and y, n is the number of samples, $\bar{x}$ is x mean, $\bar{y}$ is y mean, Δt is sampling interval, and τ is time delay of the correlation function maximum.

The similarity between the traveling wave shapes of the forward and backward currents is compared and the correlation output exhibits the peak. The distance to the fault point can be obtained at the maximum time index of r_{xy} as

$$P = \frac{v_p \tau}{2} \tag{2-26}$$

Fig. 2-17 shows an example of a traveling wave signal, where the x axis is converted to distance and the result of the auto-correlation function is shown in Fig. 2-18 with small peak at 6.3 km [34].

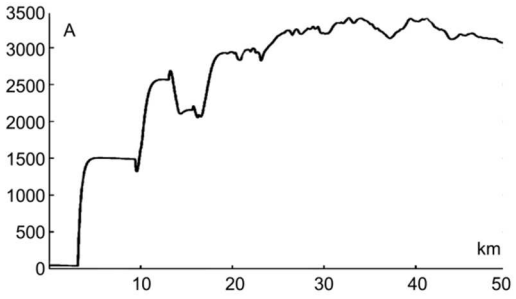

Fig. 2-17 Traveling Wave Signal as a Function of Distance [34].

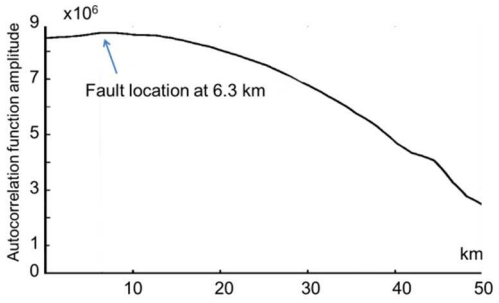

Fig. 2-18 Auto-correlation for a Fault Current as a Function of Distance [34].

Frequency domain approach

The Fourier transform (FT) is known as the most popular and easy transformation to obtain frequency components in traveling wave signals. The FT breaks a signal down into constituent sinusoids of different frequencies and infinite duration.

The FT and its inverse give a one-to-one relationship between the time domain $x(t)$ and the frequency domain $X(\omega)$ and it is defined as follows for given signal $I(t)$,

$$FT(\omega) = \int_{-\infty}^{+\infty} I(t) \cdot e^{-j\omega t}\, dt \tag{2-27}$$

where $\omega(= 2\pi f)$ is the angular frequency. This transform is suitable for stationary signals, whose frequency components are constant at all time. The discrete Fourier transform (DFT) can be written as follows.

$$DFT(k) = \frac{1}{N}\sum_{n=1}^{N} I[n] \cdot e^{-\frac{j2\pi kn}{N}} \tag{2-28}$$

Because the FT performs the integration for all time intervals as shown in Eq. (2-27), the FT gives frequency information by the integral corresponding to all time instances. In other words, the FT cannot tell us that which frequency component exists at what time instant. This is the main reason why the FT is not suitable for non-stationary signals.

The use of dominant frequencies from the transient signal caused by a fault is proposed by V. Faybisovich in 2008 [45]. The surge current will be reflected with the same sign and goes back to the source side, and then reflected again from the source side end it returns back to the fault point.

This process will be completed in $4\tau_p$, where τ_p is the surge propagation time from the source side to the fault point. Therefore, the dominant frequency f_1 in the current signal after the circuit breaker opening is equal to

$$f_1 = \frac{1}{4\tau_p} \tag{2-29}$$

The relationship between the fault location, P and f_1 is

$$P = \frac{v_p}{4f_1} \tag{2-30}$$

The accuracy of this one-ended method depends on the accuracy of propagation speed v_p, which is affected by ground resistivity. This can be improved in a double-ended frequency method. When the circuit breaker CB1 and CB2 at both ends of the cable are opened to remove a fault, they generate dominant frequencies f_1 and f_2 respectively.

$$f_2 = \frac{v_p}{4(l - P)} \tag{2-31}$$

Given l is the known total cable length, the distance to the fault can be calculated as

$$P = l\frac{f_2}{(f_1 + f_2)} \tag{2-32}$$

This expression eliminates the unknown propagation speed v_p.

This method is verified by field testing and results in comparable accuracy to the impedance based fault location method, which is typically within 3% of the total length of the non-compensated line [45].

Time-frequency domain approach

Short time Fourier transform (STFT)

One of the dominant analytical tools for frequency domain is the DFT. The DFT assumes the signal as stationary, but the traveling wave is always non-stationary, nonperiodic and transient. Also, the DFT does not give any information about the spectrum changes with respect to time.

To overcome this deficiency of the DFT, the short time Fourier transform (STFT) and the wavelet transform (WT) can be used for analyzing the traveling wave in both the time and frequency domains.

The STFT divides the signal into small segments which can be assumed to be stationary. The window function is multiplied to the signal within the Fourier integral. Narrower windows give better time resolution and better stationarity, but causes poorer frequency resolution.

One defect of the STFT is that we can obtain only the time intervals, but not an exact time point in which a certain band of frequencies exist. The STFT is defined as

$$STFT(t,\omega) = \int_{-\infty}^{+\infty} I(t) \cdot W(t-\tau) \cdot e^{-j\omega t} \tag{2-33}$$

where $W(t-\tau)$ is a window function, τ is the translation, and t is time.

Because the resolution of frequency and time is directly opposite to each other, a compromise is made between the time and frequency resolutions by adjusting the size of the windows, and the precision of time and frequency information is determined by the size of the window.

Wavelet transform (WT)

The WT is regarded as a powerful and well suited method for traveling wave signal analysis [46]. It uses short time intervals for high frequency components and long time intervals for low frequency components. Therefore, the WT meets the requirements of both time and frequency localization.

For given a function $x(t)$, its continuous wavelet transform (CWT) is defined as

$$CWT_x^{\psi}(\tau, s) = \Psi_x^{\psi}(\tau, s) = \frac{1}{\sqrt{|s|}} \int_{-\infty}^{+\infty} x(t) \cdot \Psi^* \left(\frac{t - \tau}{s} \right) dt \tag{2-34}$$

Two variables: τ and s are the translation (parameter of location) and the scaled parameter, respectively; $\Psi(t)$ is the mother wavelet, which is a band-pass filter and prototype for generating the other window functions, Ψ^* is its conjugate. The term translation, τ refers to the location of the window, the scale parameter, s is inversely proportional to frequency. High scales give global information, whereas low scales give detailed information about the signal.

The wavelet transform of sampled waveforms can be obtained by discrete wavelet transform (DWT), which is given as

$$\mathrm{DWT}(k, n, m) = \frac{1}{\sqrt{|s_0^m|}} \sum_n x[n] \cdot \Psi \left(\frac{k - n\tau_0 s_0^m}{s_0^m} \right) \tag{2-35}$$

The scaling and translation parameters s and τ, in Eq. (2-34) are replaced by s_0^m and $n\tau_0 s_0^m$, respectively; n and m are integer variables.

The DWT analyzes a signal at different frequency bands with different resolutions by decomposing the signal into a coarse approximation and detailed information with scaling functions and wavelet functions, which are associated with low-pass and high-pass filters.

As one of main features, the WT implements a multi-stage filter bank using the low-pass mother wavelet $H_0(n)$ and its half-band high-pass filter, $H_1(n)$ [47], [48]. After the filtering, half of the samples can be eliminated according to Nyquist theorem [49].

The output of the low-pass filter is filtered again in high and low-pass filters with down sampling by 2 until the DC value is reached as shown in Fig. 2-19.

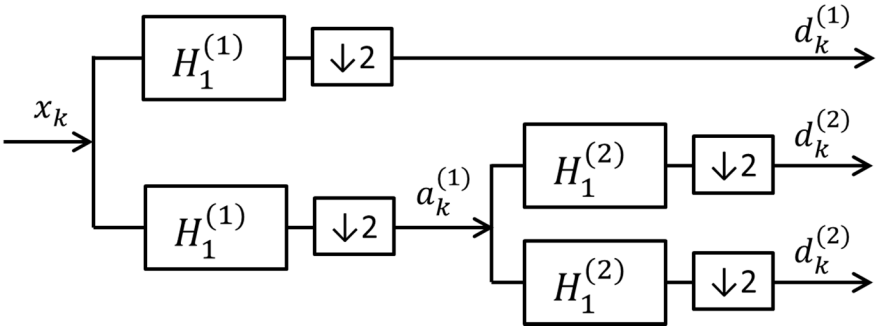

Fig. 2-19 Wavelet Transform Filter Bank [50].

At the lowest scale like scale 1, the mother wavelet is the most localized in time and oscillates most rapidly within a very short period of time, and for higher scales it becomes less localized in time and oscillates less due to the dilation nature of the wavelet. Therefore, fast and short transient disturbances will be detected at lower scales, whereas slow and long transient disturbances will be detected at higher scales [51].

Fig. 2-20 shows an example of WT based fault location. When a fault occurs at point P (36 km from bus A), traveling waves are recorded on both sides of the system.

The WT analysis on these voltage signals reveals their travel times between the fault points and relay locations. A disturbance will be seen at bus A at time t_A, similarly a wave will reach bus B at time t_B, and the difference of these times is $t_d = t_A - t_B$.

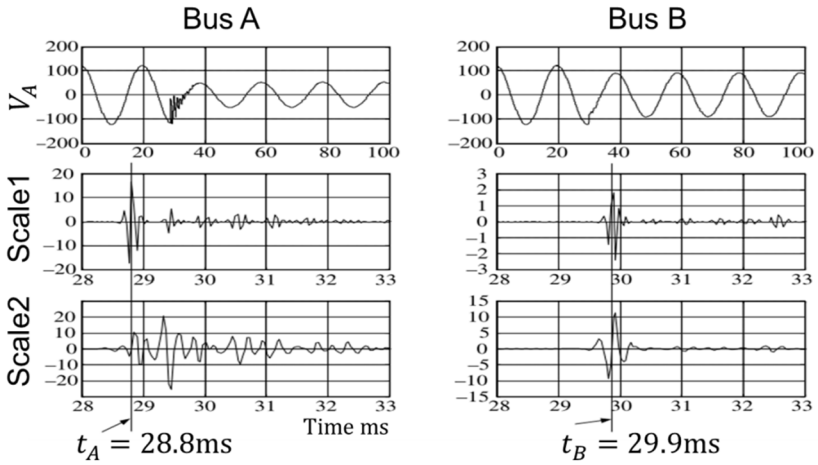

Fig. 2-20 Illustrations of Distorted Voltage Analyses using WT [5].

The WT performs decomposition of incoming voltage signals and the obtained wavelet coefficient at different scales ensures finding the traveling wave occurrence times; peaks can be observed on the waveform and the very first received waves that directly correspond to the times t_A and t_B. The distance to the fault point is calculated as

$$P = \frac{l - v_p t_d}{2} \tag{2-36}$$

Assume the velocity of the traveling wave, $v_p = 1.175 \times 10^5$ km/s, and $t_A = 29.81\ ms$, $t_B = 29.90\ ms$, then distance to the fault point $P = 35.96\ km$.

In fact, the main problem is not to detect the traveling wave but to select the correct WT. The WT will display not only desirable traveling waves from the internal

faults, but also undesirable slight disturbances from the outside of the power system. Thus, how to distinguish correct traveling waves from other disturbances is very important.

(c) Partial discharge (PD) method

The following gives an example of an on-line PD monitoring system which has been deployed on a trial basis in typical urban 350 m 11 kV network in mainland Spain. The capacitive coupling units are used for PD detection using data acquisition systems with 8 nanoseconds sampling interval. The calibration system injects calibration pulses (2 negative and 2 positive) continuously and charges at a third point in the system.

Fig. 2-21 shows some behavior of parameters in relation to the variation of system voltage and some unusual step changes that indicate a real rise in PD activity. A gradual rise in the PD event count was observed over a 3 day period with abrupt changes in the maximum apparent charge. Using this information, the power cable has been maintained without failure [28].

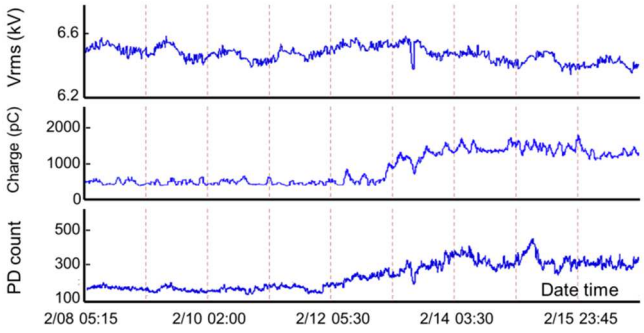

Fig. 2-21 Trending of Line Voltage, PD Charge and PD Event Count [28].

When PD is encountered at the fault location, there are two major problems. One is the significant reduction of the reflected pulse by traveling a long distance in the cable

and broadening, but this can be improved by the appropriate selection of sensor bandwidth [26].

The second problem is the external disturbance during the on-site measurement such as radio and television stations broadcasting, corona, PDs that are produced by other equipment, etc. Some noise reduction methods, such as correlation and adaptive filtering have been developed and proven successful in on-line and off-line PD measurements. However, these closed-loop noise reduction methods need to measure the reference noise prior to the actual measurement, thus computational time increases dramatically.

Faster computational time of signal data processing and analysis is necessary for on-line measurement. For this purpose, the open-loop noise reduction techniques such as linear prediction coding (LPC) and DWT have been proposed. The LPC predicts the following sample with an optimum predictor that minimizes the mean square prediction error by valuing the previous samples [26].

This chapter reviewed widely used technologies for power cable health assessment and fault location. All the techniques give a good solution for their purpose with specific advantages and disadvantages, but the industry still lacks an effective approach for online power cable monitoring, which can accomplish cable diagnosis and fault location. The new passive methodology developed in this dissertation for power cable monitoring and fault location will provide a fundamental solution for this need and the background knowledge in this chapter will help to differentiate our methodology from recent technologies.

CHAPTER 3

NEW PASSIVE METHODOLOGY

This chapter introduces a new passive methodology for power cable monitoring and fault location with theoretical studies about resonant frequency behaviors.

First, the basic concept of the methodology is explained and two example applications, specifically water pipeline leakage detection and transformer deformation detection, using the resonant frequency characteristics are described.

Next, the theoretical bases of the frequency dependent transmission system model, electrical parameters of the power cables, and the resonant frequency with transfer function are reviewed.

Mostly, the behavior of resonant frequencies in a power cable transmission system is studied with analytical derivations under various loads conditions and fault positions. In addition, similar studies are carried out for a power transformer connected cable transmission system in order to provide an accurate representation of the real site conditions.

3.1 New Passive Methodology

The resonant frequencies are determined by the electrical parameters (i.e., resistance, inductance and capacitance) of the power cable. When these parameters are changed by some reason (e.g., load change, capacitor banks switching and fault occurrences), the resonant frequencies will change in accordance with the status of the transmission system.

3.1.1 Passive Methodology for Cable Monitoring and Fault Location

The main idea of the new passive methodology for power cable monitoring and fault location is based on the behavior of resonant frequencies under change of cable conditions. The resonant frequencies of the normal steady state can be used as a fingerprint to detect fault conditions of power cables. In other words, the changes of power cable parameters can be monitored by on-line resonant frequency analysis with comparison to the reference resonant frequencies, which are obtained during fault-free normal conditions.

The power cable is modeled based on the equivalent pi (Π) circuit, which shows good consistency with the frequency dependency of the power cable, and the resonant frequencies are determined using the transfer function between source and load side voltages.

Additional modified equivalent circuits are modeled to study the resonant frequency behaviors for various load conditions and fault positions. The graphical analyses using Matlab are added for comprehensive understanding. Also, similar studies are implemented for the power transformer connected cable system.

Because complete experimental trials of this new passive methodology have not been carried out, we can evaluate the feasibility of this methodology by examining similar applications that use the resonant frequency for water leakage location in a water pipeline and fault detection in a power transformer.

3.1.2 Hydraulic Leakage Location by Resonant Frequency

Hydraulic systems can be represented by electrical parameters as resistance, inductance and capacitance. Based on similar principles to the power system, water leakage can be detected and located by analyzing the resonant frequencies of a water pipeline.

When the water pipe has a periodic excitation due to pressure fluctuations, the pipe system will oscillate at the frequency of the excitation (known as steady-oscillatory). If the excitation is at a resonant frequency, the response becomes larger and can cause pipeline failures from high pressures [52].

For small transient signals, the impact of nonlinearity is negligible and the pipeline can be considered as a linear system with frequency dependence. Whereas resonant frequencies reinforce and transmit input signals, other frequencies are absorbed within the system. In this respect, pipeline systems are similar to frequency filters, whose characteristics are determined by system properties such as boundary conditions, friction, and wave speed.

The degree that each frequency component is absorbed or transmitted within the pipeline can be described by a frequency response diagram (FRD), also known as the transfer function for the system. The FRD is determined by the measurement of the input transient signal and the pressure response from the pipeline. This FRD relates both magnitude and phase between the system output and input for different frequencies [53] [54].

The following numerical analysis example shows the resonant peak sequencing method. The FRD is extracted at the downstream valve boundary of the pipeline in Fig. 3-1.

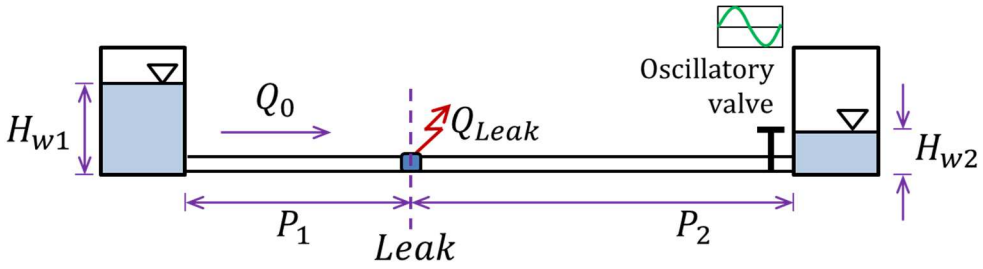

Fig. 3-1 Single Pipeline with a Leakage [54].

For a linearized pipeline system with asymmetric boundary conditions, the FRD shows a series of evenly spaced peaks and troughs as shown in Fig. 3-2(d). The peaks are at the odd multiples of ω_{th}, which is the fundamental angular frequency of the pipeline and is defined with length of the pipeline l

$$\omega_{th} = \frac{v_p \pi}{2l}, \qquad \mu_k = \frac{1}{v_p}\sqrt{jR_k A_k g\omega - \omega^2} \tag{3-1}$$

where v_p is the wave speed, μ_k is the propagation parameter, R_k is a linearized frictional resistance term, g is gravitational acceleration, and A_k is pipe cross-sectional area.

Fig. 3-2 shows that the order of the resonant peaks ranked in terms of the magnitude of the peaks has changed from [3,1,4,5,2] to [2,5,3,1,4] when the leak point changed from 700 m (a) to 1400 m (c) from the base of the upper boundary. The numbers in the square brackets indicate the "nth" peak in the FRD. When the leak size ($C_d A_L$) increased from 0.00014 m^2 (a) to 0.00028 m^2 (b), the magnitudes of all resonant peaks

are reduced, but the overall relative sizes are not changed. Therefore, ranking the sizes of resonant peaks in order of magnitude can be defined as the shape of FRD and can be used as a leak location method in single pipeline [54].

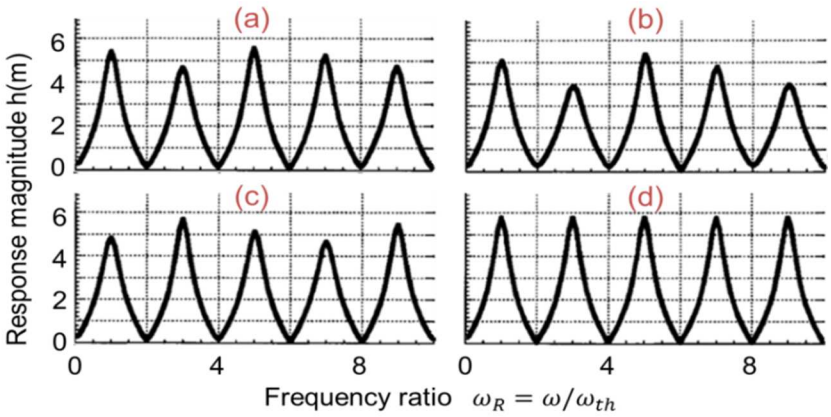

Fig. 3-2 Frequency Responses for Different Leak Size and Location (A) Leak at 700 M C_dA_L=0.00014 m^2, (B) Leak at 700 M C_dA_L=0.00028 m^2, (C) Leak at 1,400 M C_dA_L=0.00014 m^2, and (D) No Leak [54].

3.1.3 Transformer Fault Detection by Resonant Frequency

The visual inspection of a power transformer is costly and does not always provide the desired results and it requires oil drainage and entering a confined space to inspect. An alternative method is sweep frequency response analysis (SFRA) which can implement field-diagnostic techniques.

SFRA is a well-known testing method in the industry to find a transformer winding deformation, e.g. coils, turns, layers, HV (high voltage) leads, resulting from short circuit current (faults) or impacts during transportation and aging [55]. This method measures the frequency response of the output signal from the winding terminal by injecting low voltage input sine signals with various frequencies.

The core and winding assembly of a transformer can be treated as a complex electrical network as shown in Fig. 3-3. The frequency response of such a network is unique, therefore it can be considered as a fingerprint. The geometrical changes of the network elements cause deviations in its frequency response, and the differences between an SFRA fingerprint and the measurement are an indication of deformation [56].

Typically, plots range from 10 Hz to 10 MHz in a single graph, and the interesting frequency is between 20 Hz and 2 MHz in response for a high voltage star connected winding [57]. The gain $A(dB)$ of transfer function $H_W(j\omega)$ is defined as

$$A(dB) = 20\log_{10}\left(H_W(j\omega)\right) \tag{3-2}$$

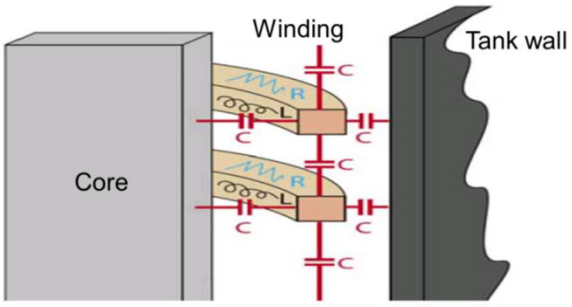

Fig. 3-3 Simplified Network of a Transformer [56].

Two examples for SFRA are shown in Fig. 3-4. The left side SFRA compares HV winding signals from a 36-year-old transformer (40 MVA) after a refurbishment. Both traces show good congruity between winding conditions before and after refurbishment. The right side SFRA is HV winding test results for two 63-MVA sister transformers. The variations between two traces are clearly visible, and one transformer (red one) has turned out to have shorted turns [56].

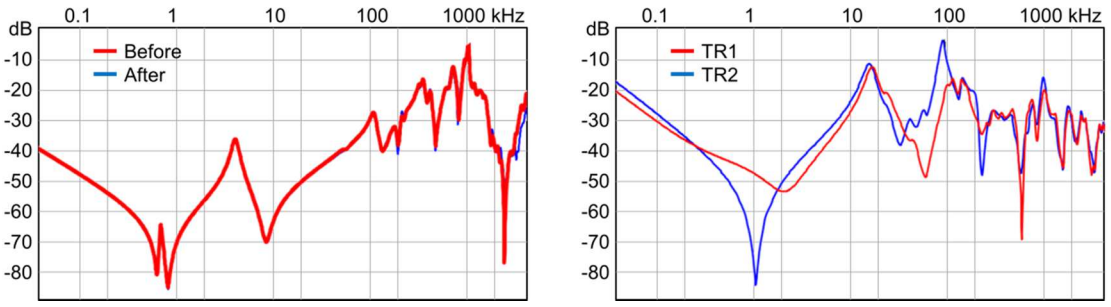

Fig. 3-4 Examples of Transformer SFRA, Healthy (left) and Faulty (right) Condition [56].

3.2 Power System Parameters and Resonant Frequency

The power transmission system can be characterized by its distributed electrical parameters as resistance, inductance and capacitance.

3.2.1 Overhead Transmission Line

The electrical parameters of a transposed three phase overhead transmission line can be expressed as [58],

$$\text{Resistance,} \qquad R_x = R_{75}\ [\Omega/\text{km}] \tag{3-3}$$

$$\text{Inductance,} \qquad L_x = \frac{\mu_0}{2\pi}\ln\left(\frac{GMD}{GMR}\right)\ [\text{H/km}] \tag{3-4}$$

$$\text{Capacitance,} \qquad C_x = \frac{2\pi\varepsilon_0}{\ln\left(\frac{GMD}{r_{bund}}\right)}\ [\text{F/km}] \tag{3-5}$$

Here, the conductor geometrical mean distance $GMD = \sqrt[3]{D_{ab}\cdot D_{bc}\cdot D_{ca}}$ where D_{ab}, D_{bc}, D_{ca} are distance between phases.

The conductor geometric mean radius $GMR = \sqrt{d\cdot GMR_c}$ for 2 bundled conductors

where GMR_c is GMR of conductor d is the distance between conductors.

The equivalent radius of the conductor $r_{bund} = \sqrt{d_{bund} \cdot r_0}$ where d_{bund} is the distance between bundles and r_0 is the conductor radius.

ε_0 is vacuum permittivity and μ_0 is vacuum permeability. R_{75} is resistance at 75°C.

3.2.2 Underground Cable

Compared to the overhead line, the power cable has a higher capacitance. This capacitance causes a larger reactive power and complicated electromagnetic phenomenon that may result in energizing or de-energizing overvoltage in the power system.

The resistance of the power cable can be defined as

$$R_x = R_{AC} = R_{DC}\left[1 + y\left(k_s + k_p\right)\right] \ [\Omega/\text{km}\ ] \tag{3-6}$$

Where R_{AC} and R_{DC} are equivalent resistance in AC and DC circuit conditions respectively.

k_s is the skin effect factor, k_p is the proximity effect factor, and y is a constant ($y = 1$ for 1, 2 and 3 core cables, $y = 1.5$ for pipe-type cables) [59].

The inductance for these layouts can be calculated as [60]

$$L_x = 2 \cdot 10^{-4} \ln\left(\frac{D\ (or\ D')}{0.778 \cdot r}\right) \ [\mu\text{H/km}] \tag{3-7}$$

where D is the distance between phases in a trefoil layout ($D' = \sqrt[3]{2}D$ for a flat layout), and r is the outer radius of the core conductor.

The capacitance between the sheath and earth is [60]

$$C_x = 0.0556 \frac{\varepsilon_{se}}{\ln\left(\frac{r_o}{r_{s,out}}\right)} \quad [\mu F/km/phase] \tag{3-8}$$

Where ε_{se} is the relative permittivity of insulation between sheath and earth (polyethylene $\varepsilon_{PE} = 2.3$), r_o is the cable radius and $r_{s,out}$ is the sheath outer radius.

3.2.3 Equivalent Pi (Π) Circuit and Resonant Frequency

Many literatures on transient analysis verify that the equivalent pi model is the best fit to the frequency dependent behavior of the transmission system [61]. As the transmission system supplies energy to the load, electrical parameters are distributed along the line and this line is divided into small dx sections as shown in Fig. 3-5.

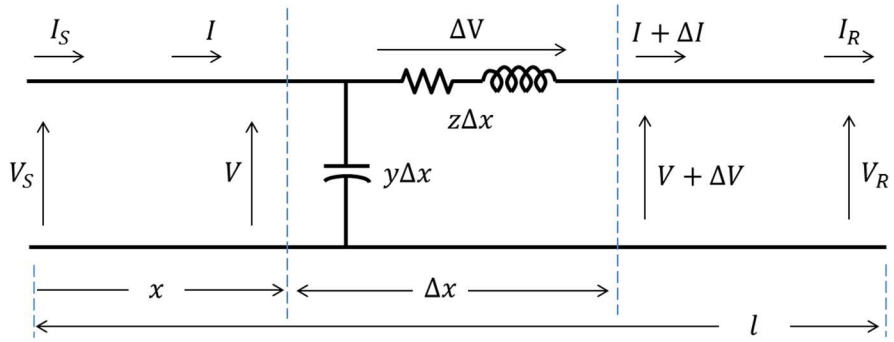

Fig. 3-5 Equivalent Network of Δx Sections for Transmission System.

The line impedance and capacitive reactance are

$$z = R_x + j\omega L_x, \qquad y = j\omega C_x \tag{3-9}$$

The transmission line equations are

$$V(x) = V_R \cosh(\gamma x) + Z_c I_R \sinh(\gamma x) \tag{3-10}$$

$$I(x) = \frac{V_R}{Z_c}\sinh(\gamma x) + I_R\cosh(\gamma x) \tag{3-11}$$

where γ is the propagation constant, α is the attenuation constant (Np/m), and β is the phase constant (rad/m), and Z_c is the characteristic impedance (or surge impedance),

$$\gamma = \sqrt{z \cdot y} = \sqrt{(R_x + j\omega L_x) \cdot (j\omega C_x)} = \alpha + j\beta \tag{3-12}$$

$$Z_c = \frac{z}{\gamma} = \sqrt{\frac{z}{y}} = \sqrt{\frac{1}{j\omega C_x}(R_x + j\omega L_x)} \tag{3-13}$$

When l is the length of the transmission system, its ABCD parameters are

$$\begin{bmatrix} A & B \\ C & D \end{bmatrix} = \begin{bmatrix} \cosh(\gamma l) & Z_c\sinh(\gamma l) \\ \dfrac{\sinh(\gamma l)}{Z_c} & \cosh(\gamma l) \end{bmatrix} \tag{3-14}$$

The equivalent circuit for the transmission line is shown in Fig. 3-6, which called an equivalent pi model.

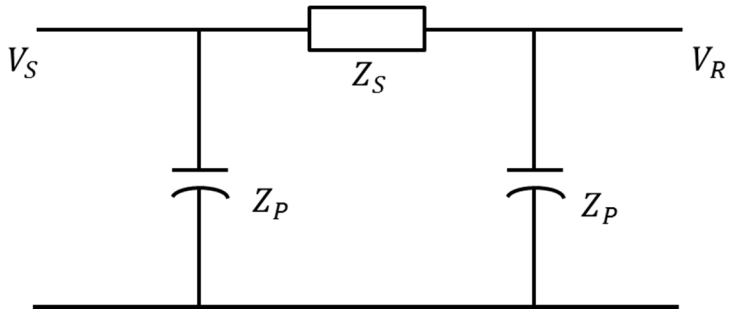

Fig. 3-6 Equivalent pi model.

Let $zl = Z$, $yl = Y$, the parameters of this equivalent pi model are

$$Z_S = Z_c \sinh(\gamma l) = Z \frac{\sinh(\gamma l)}{\gamma l} \tag{3-15}$$

$$\frac{1}{Z_P} = \frac{Y}{2} \frac{\tanh\left(\frac{\gamma l}{2}\right)}{\frac{\gamma l}{2}} \tag{3-16}$$

These equations give the voltage and current distribution along the line. The transfer function for a power cable transmission system without a load is

$$H_C = \frac{V_R}{V_S} = \frac{Z_P}{Z_S + Z_P} = \frac{1}{\cosh(\gamma l)} \tag{3-17}$$

In the s-domain,

$$H_C(s) = \frac{V_R(s)}{V_S(s)} = \frac{1}{\cosh\left(\sqrt{(R + sL)sC}\right)} \tag{3-18}$$

where, $R = R_x l$, $L = L_x l$ and $C = C_x l$.

The resonant frequencies of this model are roots of the denominator in Eq. (3-18).

$$s_{Cn} = -\frac{R}{2L} \pm j\sqrt{\frac{\left((2n-1)\pi\right)^2}{4LC} - \frac{R^2}{4L^2}}, \qquad n = 1, 2, 3, \ldots \tag{3-19}$$

Typically, $1/(LC) \gg (R/L)^2$, so that the approximate roots are

$$s_{Cn} \cong -\frac{R}{2L} \pm j\frac{(2n-1)\pi}{2\sqrt{LC}}, \qquad n = 1, 2, 3, \ldots \tag{3-20}$$

The gain peak appears when the frequency is equal to the imaginary part of Eq. (3-20). Therefore, the approximate resonant frequencies are [62]

$$\omega_{r_{Cn}} \cong \frac{(2n-1)\pi}{2\sqrt{LC}}, \qquad fr_{Cn} \cong \frac{(2n-1)}{4\sqrt{LC}}, \qquad n = 1, 2, 3, \ldots \tag{3-21}$$

These resonant frequencies follow the odd order multiple sequences, which mean that the second resonant frequency is 3 times the first resonant frequency, the third resonant frequency is 5 times the first resonant frequency, and so forth.
The detailed derivation of the resonant frequencies is given in Appendix A.

3.3 Behavior of the Resonant Frequencies

3.3.1 Resonant Frequency Estimation

The resonant frequencies are known as the critical frequencies of power systems where the system could be sensitively excited. Therefore, it is helpful to have prior knowledge about the resonant frequency behaviors under operational and abnormal conditions.

Recently, increasing interest in risks from harmonic overvoltage and distortion from renewable power facilities (especially in wind farms) have led to great improvements in harmonic frequency estimation and analysis.

The resonant frequencies are divided into series and parallel resonant frequencies. When a series RLC circuit resonates at the series resonant frequency, the equivalent impedance becomes a minimum and causes maximum current. In contrast, the parallel

resonant frequency maximizes the equivalent parallel impedance in the circuit and causes maximum voltage.

The parallel resonant frequencies are observed at the peak positions in nodal impedance-frequency curves. When harmonic current excitations are close to these parallel resonant frequencies, particularly high magnifications of voltage occur at the resonant critical positions and these result in worsening power quality, malfunction or in the worst case destruction of power system elements.

On the contrary, a series resonance causes a high harmonic current that causes excessive heat on the devices at the resonant frequency. Therefore, analysis of resonances is an important issue to avoid critical effects of harmonics in the power systems [63].

The widely used methods for resonant frequency identification are the "impedance scan" method and the "harmonic modal resonant analysis (HMRA)" method. The idea of HMRA is that when the admittance matrix approaches a singularity, the nodal voltages go high with occurrence of harmonic resonance. The singularity of the admittance matrix is due to the very small eigenvalue which approaches zero. Through eigenvalue decomposition, the HMRA can perform further analysis on the resonant point and the sensitivity, which can reveal the true resonant location and the potential point of the most influenced bus in the network [64], [65], [66].

The impedance scan, also known as the frequency scan, is the most prevalent method for resonance identification [67]. The nodal admittance matrix Y_h is evaluated for every harmonic current I_h at every specific frequency.

$$[V_h] = [Y_h]^{-1} \cdot [I_h], \qquad for\ h \neq 1 \tag{3-22}$$

The nodal harmonic impedance is obtained from the inverse of the nodal admittance matrix. The diagonal elements of this matrix are harmonic self-impedances of the respective buses and the non-diagonal elements are transfer impedances, related to the effect on the voltage of bus i when the harmonic current (usually 1A) is injected at bus j [66].

The characteristics of the resonant frequencies in a power system can be simulated by the EMTP (Electro Magnetic Transients Program) PSCAD. The frequency scan tool in PSCAD generates the system impedance matrix in the phase domain for a given network. This matrix is then collapsed into an equivalent matrix as seen from the measuring point. This is repeated for a specified range of frequency [68].

The harmonic impedance solution uses RLC data directly, avoiding integration or curve fitting errors. The equations are solved at each frequency in the phase domain without using sequence networks, thus it gives accurate representations for an unbalanced transmission system, Y-Δ transformers, etc. [68].

This dissertation studies mainly about parallel resonant frequencies under various load and fault conditions.

3.3.2 Cable Power System

(a) Resonant frequencies in a cable power system

When the power cable system has a load as shown in Fig. 3-7, the transfer function is

$$H_{CL} = \frac{V_R}{V_S} = \frac{Z_P Z_L}{Z_S Z_P + Z_S Z_L + Z_P Z_L} \tag{3-23}$$

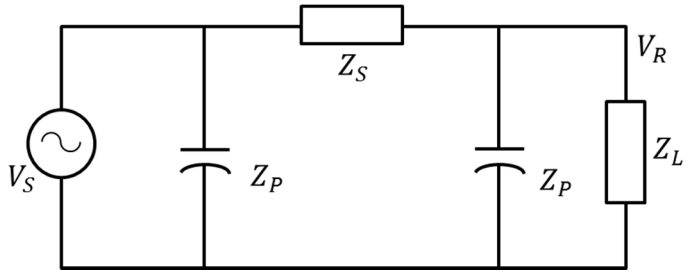

Fig. 3-7 Equivalent Pi Model with Load.

Also the resonant frequencies can be obtained from a frequency-impedance calculation at the load voltage. The equivalent impedance of system at the load side Z_{in} is

$$Z_{in} = \frac{Z_S Z_P Z_L}{Z_S Z_P + Z_S Z_L + Z_P Z_L} \tag{3-24}$$

We can expect the same resonant frequency solutions from Eq. (3-23) and Eq. (3-24), because they have identical denominators.

However, the transfer function for a load connected cable power system, Eq. (3-23) can be simplified as Eq. (3-25) where the detailed derivation is in Appendix B.

$$H_{CL} = \frac{V_R}{V_S} = \frac{1}{\frac{1}{Z_L} Z_c \sinh(\gamma l) + \cosh(\gamma l)} \tag{3-25}$$

The power load can be expressed by a RLC parallel circuit as shown in Fig. 3-8.

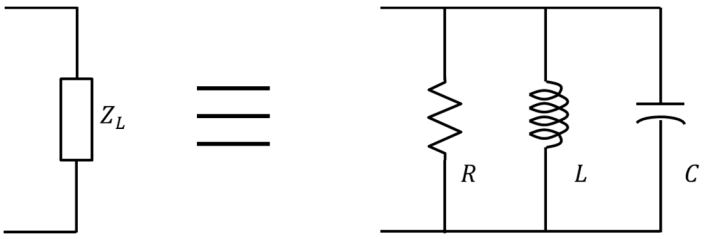

Fig. 3-8 Power Load with Parallel RLC Circuit.

For given load voltage V_{load}, apparent load power S_{load} and power factor angle ϕ, the equivalent resistance and reactance of the load are

$$R_{eq} = \frac{{V_{load}}^2}{S_{load}}, \qquad X_{eq} = R_{eq}\tan(\phi) \tag{3-26}$$

The equivalent impedance of the load is

$$Z_L = R_{eq} + jX_{eq} \tag{3-27}$$

For the parallel circuit, it is more efficient to use the load admittance Y_L as

$$Y_L = \frac{1}{Z_L} = \frac{1}{R} + j\left(\omega C - \frac{1}{\omega L}\right) = G + jB \tag{3-28}$$

When the load is purely capacitive or inductive, its maximum values are

$$C_{max} = \frac{B}{\omega}, \qquad or \;\; L_{max} = -\frac{1}{\omega B} \tag{3-29}$$

Again, the transfer function, Eq. (3-25) is written as

$$H_{CL} = \frac{V_R}{V_S} = \frac{1}{\left(\frac{1}{R} + j\left(\omega C - \frac{1}{\omega L}\right)\right) Z_c \sinh(\gamma l) + \cosh(\gamma l)} \tag{3-30}$$

The behavior of the resonant frequencies for various load conditions is studied by analyzing the contribution of each term in Eq. (3-30) using Matlab. The selected power cable electrical parameters are R_x = 0.0184 Ω/km, L_x = 0.116 mH/km, C_x = 417.97 nF/km with cable length 10.5 km. These values are commonly used in this dissertation.

Fig. 3-9 shows absolute values of all parts in transfer function (Eq. (3-30)) for a load connected cable power system. The power load is 270 MVA with power factor cos(15°) and consists of a 94.14 Ω resistor, 904 mH inductor and 233.5 μF capacitor. It can be seen that the term $\omega C - 1/\omega L$ is close to the term ωC for high frequency, which means that the capacitor component gives the dominant effect on load impedance and resonant frequency. The first resonant frequency is 3240 Hz.

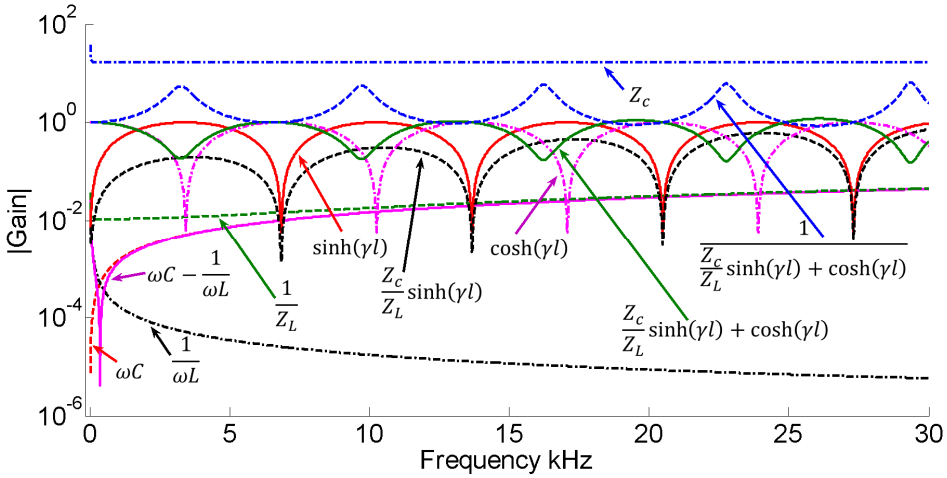

Fig. 3-9 Resonant Frequency under Load; 270 MVA, Power Factor cos(15°).

When the load is reduced to 108 MVA (40% of 270 MVA) with the same power factor cos(15°), the first resonant frequency is 3345 Hz. The small changes from the previous case are shown in Fig. 3-10. The load consists of a 235.36 Ω resistor, 2.26 H inductor and 93.4 nF capacitor. The overall shape and resonant frequencies are very similar to the previous case, but the magnitude of each gain is decreased.

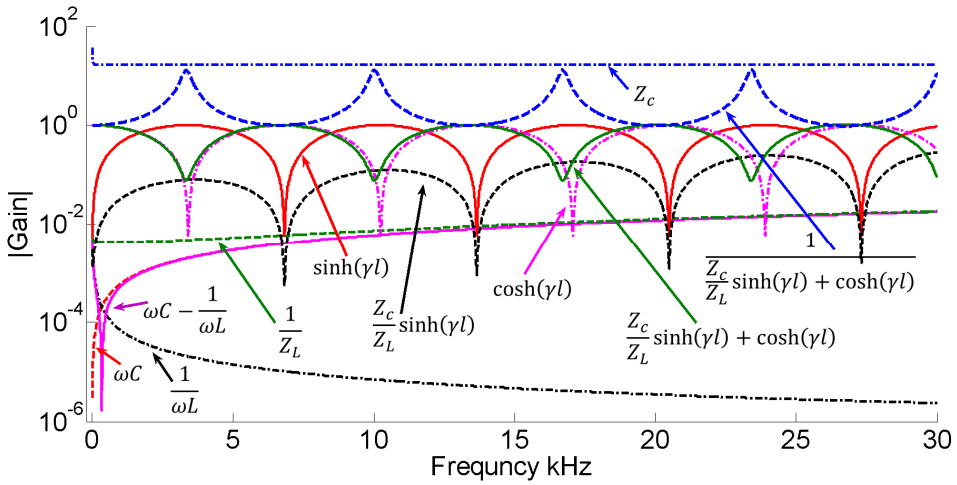

Fig. 3-10 Resonant Frequency under Load; 108 MVA, Power Factor cos(15°).

As another load condition, the power factor is changed from cos(15°) to cos(35°) with the same load 270 MVA, and each term of the transfer function equation is shown in Fig. 3-11. The composition of the load is R = 130.9 Ω, L = 481 mH and C = 438.83 nF. The first resonant frequency is 3105 Hz, and this case shows similar curve shapes as the previous load condition cases. Because the change of positive power factor is caused by change of inductance rather than capacitance, the variance of positive power factor does not affect resonant frequency behavior significantly.

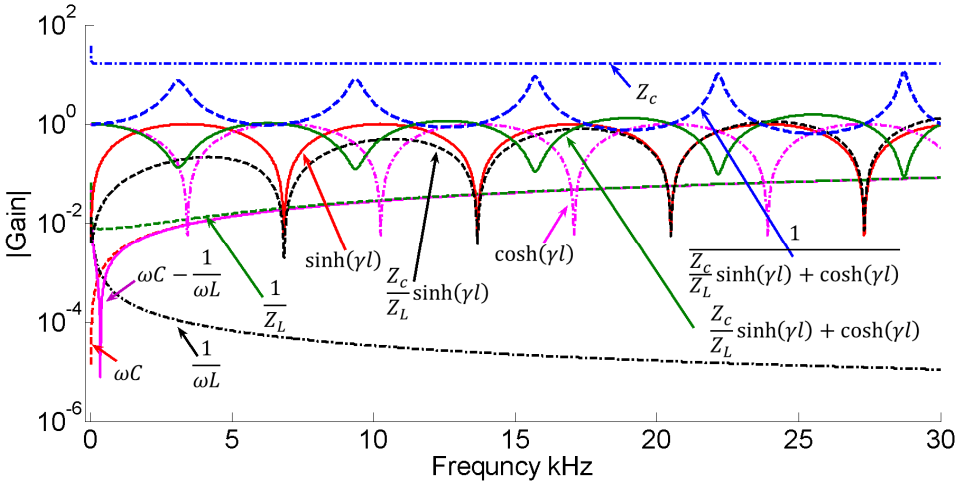

Fig. 3-11 Resonant Frequency under Load; 270 MVA, Power Factor cos(35°).

Fig. 3-12 shows the resonant frequency behavior under a negative power factor load condition. The first resonant frequency is 1135 Hz, which shows significant movement from the previous cases. It can be found that the change of capacitance, ωC affects the term $Z_c \sinh(\gamma l)\,/Z_L$ and eventually it moves the resonant frequencies. The load consists of a 130.9 Ω resistor, 16 H inductor and 14.63 μF capacitor.

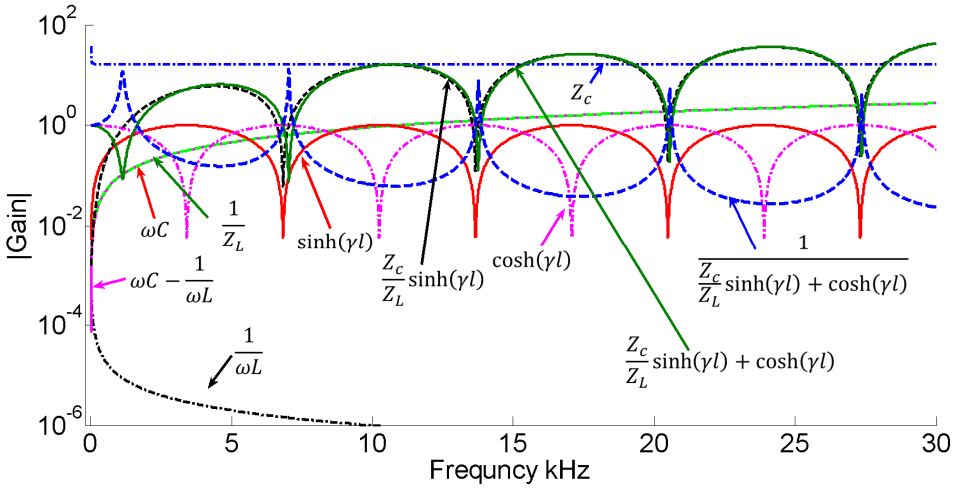

Fig. 3-12 Resonant Frequency under Load; 270 MVA, Power Factor -cos(35°).

In summary, the resonant frequencies are dominantly dependent on the value of capacitance. Most changes in the load condition (magnitude and power factor) are caused by variance of inductive loads, therefore the resonant frequencies are not influenced significantly, but the addition of the capacitive loads, which cause negative power factor operation, makes considerable movement in the resonant frequencies.

The first two resonant frequencies and composition of loads for the four cases are summarized in Table 3-1.

Table 3-1 Resonant Frequencies for Various Load Conditions.

	Case 1	Case 2	Case 3	Case 4
Load (MVA)	270	108	270	270
Power factor	cos(15°)	cos(15°)	cos(35°)	-cos(35°)
R (Ω)	94.14	235.4	130.9	130.9
L (H)	0.904	2.26	0.481	16.034
C (μF)	0.234	0.093	0.439	14.63
Resonant frequencies (Hz)	3240; 9720	3345; 10030	3105; 9350	1135; 7030

(b) Resonant frequencies for various fault positions

In fault conditions, the composition of the power cable impedance will be affected. To represent fault conditions, a fault resistor R_F is inserted in the middle of the equivalent pi model as shown in Fig. 3-13.

Let p be the fault location in terms of the fractional cable length from the source side ($0 < p < 1$),

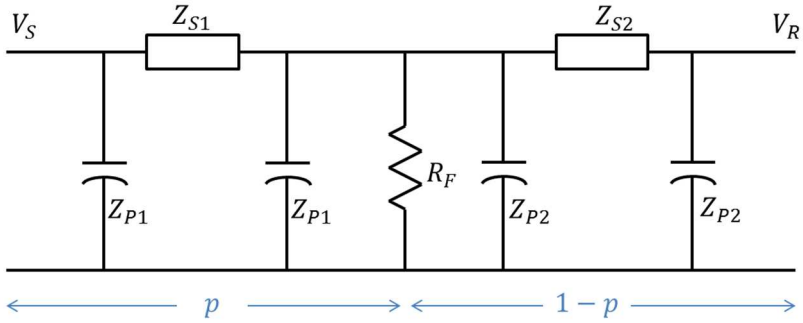

Fig. 3-13 System Model for Faulted Cable Power System.

The transfer function for a faulted cable power system is

$$H_{CF} = \frac{V_R}{V_S} = \frac{\frac{Z_{S2}}{Z_{P2}+Z_{S2}}}{Z_{S1}\left(\frac{1}{Z_{P1}}+\frac{1}{Z_{P2}}+\frac{1}{R_F}+\frac{1}{Z_{P2}+Z_{S2}}\right)+1} \tag{3-31}$$

This equation can be simplified using hyperbolic trigonometric relations,

$$H_{CF} = \frac{1}{\cosh(\gamma l) + \frac{Z_c}{R_F}\sinh(p\gamma l)\cosh(\gamma(1-p)l)} \tag{3-32}$$

The new resonant frequencies in a faulted cable power system are related to the denominator of transfer function, Eq. (3-32).

When the fault resistor R_F is very large, as for the fault-free normal condition, the second term of the denominator approaches zero and the remaining $\cosh(\gamma l)$ is identical to that for the normal condition cable power system, Eq. (3-17).

Therefore, the new resonant frequencies are derived from the second term of the denominator,

$$\sinh(p\gamma l)\cosh(\gamma(1-p)l) \tag{3-33}$$

This gives two valid sets of solutions for the resonant frequencies. The first part, $\sinh(p\gamma l)$, produces the new resonant frequencies as

$$fr_{1CFn} \cong \frac{n}{2p\sqrt{LC}}, \qquad n = 1, 2, 3, \ldots \tag{3-34}$$

And from the second part, $\cosh(\gamma(1-p)l)$

$$fr_{2CFn} \cong \frac{(2n-1)}{4\sqrt{LC}(1-p)} \tag{3-35}$$

The new resonant frequencies from Eq. (3-34) are large, in excess of our range of interest, thus Eq. (3-35) gives moderate resonant frequencies that can be monitored. The detailed derivation of transfer function and the new resonant frequencies is in Appendix C.

The quick way to understanding this behavior for different fault positions is evaluation of equivalent impedance on the load side. Usually, the fault resistor is so small as to diminish other parallel connected impedances to nearly zero, then only Z_{S2} and Z_{P2} will produce new resonant frequencies. When considering the part $Z_{S2}/(Z_{P2}+Z_{S2})$ in Eq. (3-31),

$$\frac{Z_{\mathrm{P2}}}{Z_{S2}+Z_{P2}} = \frac{\dfrac{Z_c}{tanh\left(\dfrac{\gamma(1-p)l}{2}\right)}}{Z_C\, sinh(\gamma(1-p)l) + \dfrac{Z_c}{tanh\left(\dfrac{\gamma(1-p)l}{2}\right)}} = \frac{1}{2sinh^2\left(\dfrac{\gamma(1-p)l}{2}\right)+1} = \frac{1}{cosh(\gamma(1-p)l)} \tag{3-36}$$

This is identical to a part of the faulted cable power system transfer function in Eq. (3-32).

3.3.3 Transformer Connected Power Cable System

This section studies resonant frequencies for a transformer connected power cable transmission system. In this document, TR denotes power transformer; hence, the TR connected power cable transmission system is written as “TR power system” whereas “cable power system” denotes the power cable transmission system without a TR.

(a) Resonant frequencies in TR power system

The system model for a TR power system is shown in Fig. 3-14. The TR impedance, $Z_{TR} = R_{TR} + j\omega L_{TR}$, is inserted between the power source and cable.

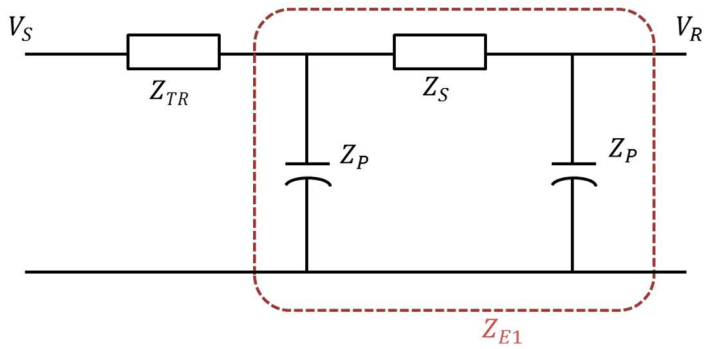

Fig. 3-14 Equivalent circuit for TR power system.

Let, $H_{S1} = Z_P/(Z_S + Z_P)$. The equivalent impedance of Z_{E1} is

$$Z_{E1} = \frac{1}{\frac{1}{Z_S + Z_P} + \frac{1}{Z_P}} = \frac{Z_P Z_P}{Z_P H_{S1} + Z_P} \tag{3-37}$$

The transfer function of the TR power system can be obtained as

$$H_T = \frac{V_R}{V_S} = \frac{Z_{E1}}{Z_{TR} + Z_{E1}} H_{S1} = \frac{1}{\frac{Z_{TR}}{Z_c}\sinh(\gamma l) + \cosh(\gamma l)} \tag{3-38}$$

The detailed derivation of the TR power system transfer function is in Appendix D.

The absolute value of each term in transfer function Eq. (3-38) when using power cable parameters and TR impedance (R_{TR} = 0.013 Ω, L_{TR} = 59.4 mH) is shown in Fig. 3-15.

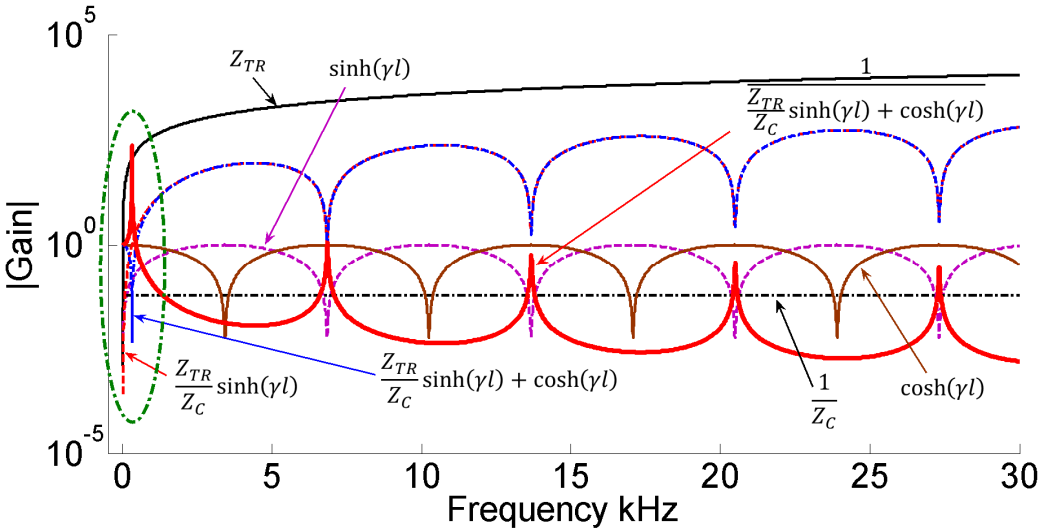

Fig. 3-15 Resonant Frequency for TR Power System.

It is found that the plot of term $Z_{TR}\frac{1}{Z_c}\sinh(\gamma l)$ and term $Z_{TR}\frac{1}{Z_c}\sinh(\gamma l)+\cosh(\gamma l)$ are very close except in the low frequency range (lower than about 500 Hz), which means the contribution of $\cosh(\gamma l)$ is so small as to ignore it in the high frequency range (higher than about 500 Hz).

As $Z_{TR}\frac{1}{Z_c}\sinh(\gamma l) \gg \cosh(\gamma l)$, the transfer function is simplified as

$$H_T \cong \frac{1}{Z_{TR}\frac{1}{Z_c}\sinh(\gamma l)} \tag{3-39}$$

Similar to the solution of Eq. (3-21), the resonant frequencies in the TR power system are

$$\omega_{r_{Tn}} \cong \frac{n\pi}{\sqrt{LC}}, \qquad fr_{Tn} \cong \frac{n}{2\sqrt{LC}}, \qquad n = 1, 2, 3, \ldots \tag{3-40}$$

Recall that the transfer function for a cable power system is $1/\cosh(\gamma l)$ in Eq. (3-17). Comparing it with Eq. (3-39), the denominators, which define the resonant

frequencies, are $\cosh(\gamma l)$ for the cable power system and $\sinh(\gamma l)$ for the TR power system. The difference between the TR and cable power system resonant frequencies (Eq. (3-40) and Eq. (3-21)) is the same as the first resonant frequency of the cable power system.

$$fr_{Tn} - fr_{Cn} \cong \frac{n}{2\sqrt{LC}} - \frac{(2n-1)}{4\sqrt{LC}} = \frac{1}{4\sqrt{LC}} \tag{3-41}$$

Therefore, when the resonant frequencies of the cable power system are shifted down in frequency by the same amount as its first resonant frequency, they are very close to those of the TR power system. In other words, the connected TR affects the power cable resonant frequencies to move as much as the cable-only first resonant frequency.

Because the term $\cosh(\gamma l)$ in the TR power system transfer function appears in the low frequency range, it produces the small first resonant frequency (100 Hz for this case) as indicated with dotted green ellipse shape in Fig. 3-15. This frequency will be ignored as the first TR power system resonant frequency for convenient comparison with the cable power system.

(b) Resonant frequencies under various fault positions

The model for a fault condition in the TR power system can be illustrated by combining the cable power system fault model and TR impedance as shown in Fig. 3-16.

Let p be the relative fault point from the source side ($0 < p < 1$) and the voltage V_{S2} is determined by the equivalent impedance Z_{E1}. The voltage V_{S2} plays the same role as the source voltage (V_S) in the faulted cable power system in Fig. 3-13 and the

circuit components of the faulted TR power system are identical with those of the faulted cable power system except Z_{TR}.

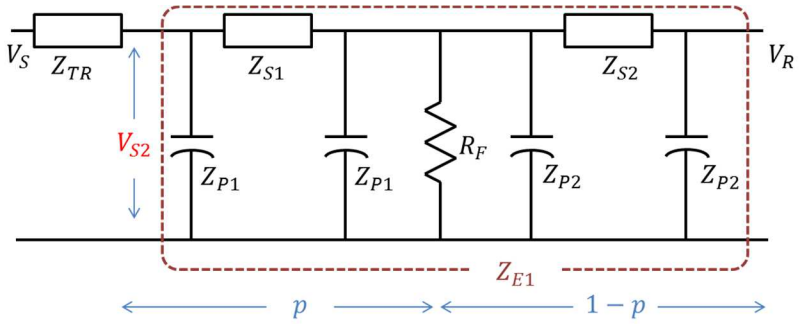

Fig. 3-16 System Model for Faulted TR Power System.

In other words, the transfer function of the faulted TR power system (H_{TF}) can be expressed by that of faulted cable power system, H_{CF} in Eq. (3-31),

$$V_R = V_s H_{TF} = V_{S2} H_{CF} = \frac{Z_{E1}}{Z_{TR} + Z_{E1}} V_S H_{CF} \rightarrow H_{TF} = \frac{Z_{E1}}{Z_{TR} + Z_{E1}} H_{CF} \tag{3-42}$$

Again,

$$H_{TF} = \frac{Z_{E1}}{Z_{TR} + Z_{E1}} \frac{1}{\cosh(\gamma l) + \frac{Z_c}{R_F} \sinh(p\gamma l) \cosh(\gamma(1-p)l)} \tag{3-43}$$

Therefore, the new resonant frequencies for the TR power system faults include the same values as the cable power system with faults case. The additional new resonant frequencies, which result from the $Z_{E1}/(Z_{TR} + Z_{E1})$ term in Eq. (3-43), are not found in this research.

CHAPTER 4

VERIFICATION BY POWER SYSTEM SIMULATION

This chapter verifies the resonant frequency behaviors, which are studied in the preceding chapter. A real power cable transmission system is utilized in the simulations. Real data for this same system have been acquired and will be analyzed in Chapter 5.

First, the frequency impedances under various power system conditions are analyzed using the frequency scan tool in PSCAD and this gives a clearer verification of resonant frequency characteristics. Secondly, the frequency analysis is performed for artificial voltage and current signals, which are obtained from simulation.

4.1 Sample Power System and Resonant Frequency

An installed 154 kV, 1200 mm^2, 10.5 km transmission underground power cable is selected for the simulation and its main parameters are listed in Table 4-1.

Table 4-1 Parameters of Sample Transmission Power Cable.

- Conductor diameter: 39.1 mm
- Outer radius of main insulator: 38.54 mm
- Propagation constant: 5.391×10^{-7} + j2.68×10^{-6}
- Inner radius of main insulator: 21.54 mm
- Resistance: 0.0184 Ω/km
- Inductance: 0.116 mH/km
- Capacitance: 417.97 nF/km
- Characteristic impedance: 17.031 – j3.422 Ω
- Spacing between conductors: 0.3 m (flat formation)

The selected underground power cable transmission system consists of a generator, power cable, electrical load and fault resistor as shown in Fig. 4-1. The cable configuration is shown in Fig. 4-2.

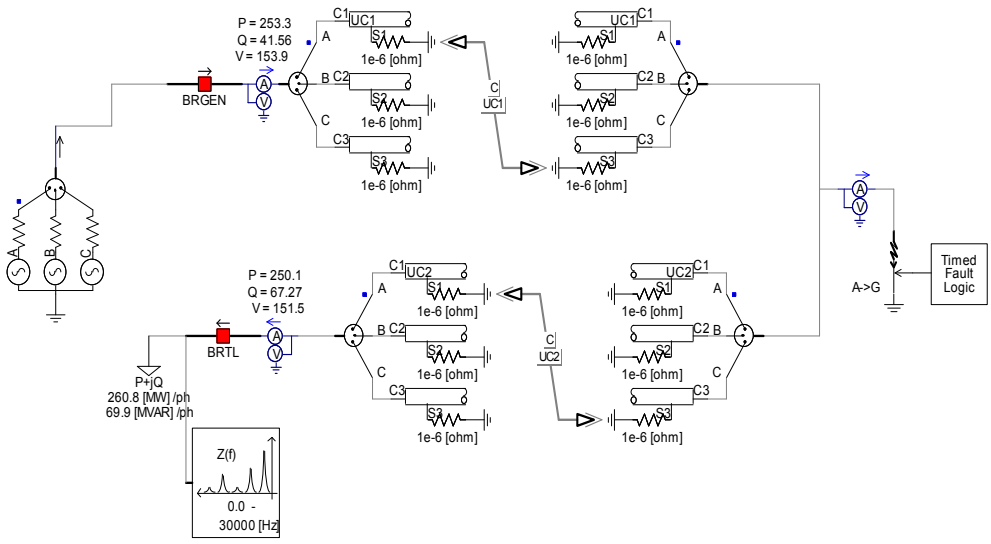

Fig. 4-1 Power Cable Transmission System with A Phase-Ground Fault.

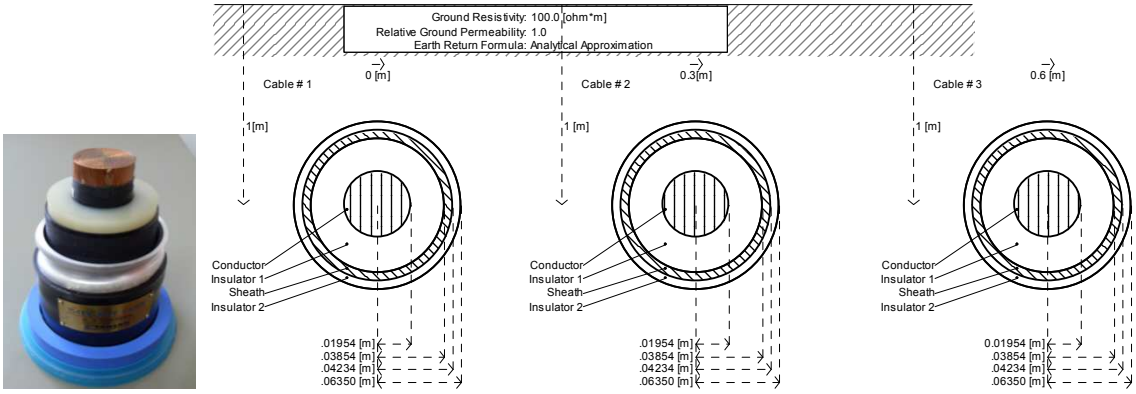

Fig. 4-2 Power Cable (Manufactured by Taihan Electric Wire) and its Configuration.

The 154 kV and 270 MVA generator is connected to the left end of the power cable. The 3-phase XLPE 1200 mm2 power cables are depicted using a frequency dependent phase mode model. This model is the most accurate to represent frequency dependent characteristics of a transmission system for all frequency ranges and improves the constant transformation problem by direct formulation in the phase domain. The modal domain approach transforms the phase-domain terminal voltages to the modal domain using the constant transformation matrix, which ignores imaginary parts for

simplifying calculation, but it causes an accuracy problem for the low frequency range and unbalanced cable geometry [69].

Therefore, the frequency-dependent phase model is accurate for all transmission configurations, including unbalanced cable geometry and strongly recommended for all transmission system cases, unless another model is chosen for a specific reason [70] [71]. The power cable length is 10.5 km and a fault resistor is inserted in the middle of power cable. The electrical load, which is expressed in terms of real and reactive power, is connected to the end of cable. The measuring point for the frequency scan is placed on the end terminal of the power cable.

The resonant frequencies obtained from PSCAD simulation are 3378 Hz and 10236 Hz for a 270 MVA load with a power factor of 0.966 (= cos15°) as shown in Fig. 4-3. These values are slightly different from values calculated by Eq. (3-21), which are 3414 Hz and 10243 Hz. This is caused by an approximate calculation method for cable RLC parameters used in Eq. (3-21) whereas PSCAD uses a more detailed treatment and the PSCAD model includes an electrical load. The PSCAD values are used as the reference values to identify the characteristics of resonant frequencies for various loads and fault conditions.

The frequency scan tool in PSCAD is used for frequency impedance analysis for a scan range of 0 to 30 kHz with frequency interval 2 Hz.

The length of the power cable is the strongest factor in determining the resonant frequencies. When the cable length is doubled, the resonant frequencies reduce to 1686, 5076, and 8496 Hz, which are nearly half of the reference values as shown in Fig. 4-4.

Consequently, the simulation result shows good agreements with the resonant characteristics asserted by Eq. (3-21).

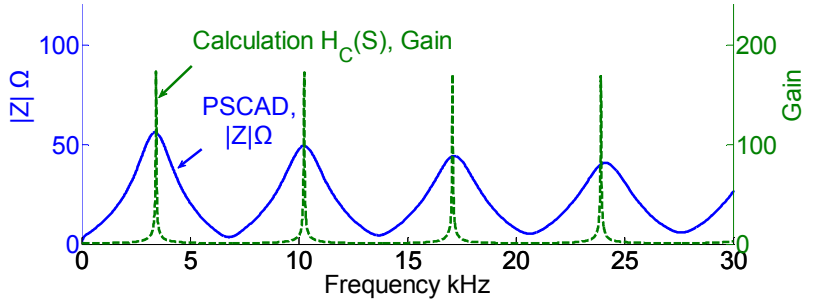

Fig. 4-3 Resonant Frequencies by Eq. (3-21) and PSCAD Simulation.

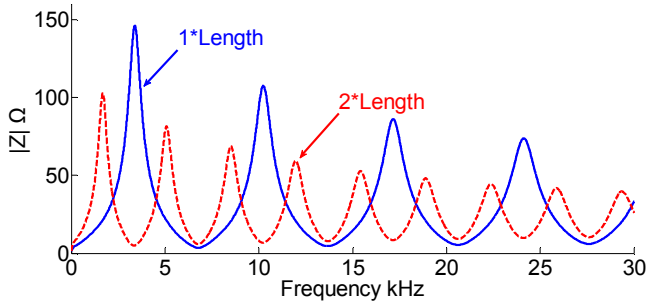

Fig. 4-4 Resonant Frequencies for Different Cable Lengths (10.5 and 21 Km, PSCAD).

4.2 Frequency Impedance Analysis

4.2.1 Cable Power System

(a) Resonant frequencies under various load conditions

The behavior of cable resonant frequencies for various loads is investigated by using the frequency scan tool, which provides frequency-impedance calculation at the measuring point. The loads are specified as 10% to 100% of the generator capacity (= 270 MVA), with a power factor of 0.966 (= cos15°).

As revealed in Fig. 4-5, the change of loads does not have a significant effect on the resonant frequencies. The numerical results are summarized in Table 4-2.

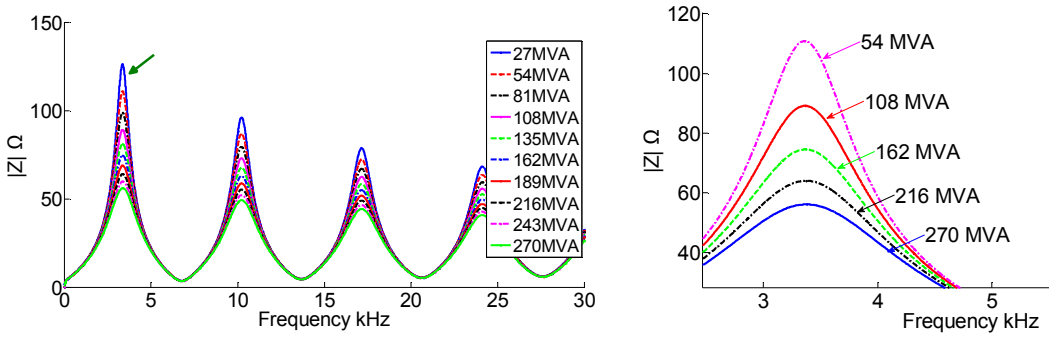

Fig. 4-5 Resonant Frequencies for Various Loads (20% to 100%).

Setting the 100% load as the reference case, the fundamental resonant frequency decreases with descending load magnitude with the change reaching –20 Hz for a 10% load compared to the reference case. In addition, they follow the odd order multiple sequences as asserted in Eq. (3-21).

For comparisons, the 'shift' is defined to represent the percentage movement of the first new resonant frequency from the reference first resonant frequency on the basis of the interval between the first and second reference resonant frequencies.

$$Shift(\%) = \frac{f_{rL1} - f_{rB1}}{f_{rB2} - f_{rB1}} \cdot 100\% \tag{4-1}$$

where f_{rB1} and f_{rB2} are the first and second reference resonant frequencies, and f_{rL1} is the new first resonant frequency from any changed system conditions (e.g., load or fault).

Because the load is connected in parallel at the measuring point, the load impedance is inversely related to the total equivalent impedance of system. Therefore, the magnitude of the system impedance $|Z|$ is larger for a smaller load.

However, these various loads can reflect the normal power system operating conditions, and these conditions affect the gain of the transfer function but not the resonant frequencies.

Table 4-2 Resonant Frequencies (Hz) for Various Loads.

Loads	270 MVA 260.8 MW	243 MVA 234.7 MW	216 MVA 208.6 MW	189 MVA 182.6 MW	162 MVA 156.5 MW
1st Peak	3,378	3,376	3,374	3,372	3,370
2nd Peak	10,236	10,234	10, 234	10, 234	10,232
3rd Peak	17,160	17,160	17,160	17,160	17,160
4th Peak	24,124	24,124	24,124	24,124	24,124
Shift	reference	-0.03%	-0.06%	-0.09%	-0.12%

Loads	135 MVA 130.4 MW	108 MVA 104.3 MW	81 MVA 78.2 MW	54 MVA 52.2 MW	27 MVA 26.1 MW
1st Peak	3,368	3,364	3,362	3,360	3,358
2nd Peak	10,232	10,232	10,232	10,230	10,230
3rd Peak	17,160	17,158	17,158	17,158	17,158
4th Peak	24,122	24,122	24,122	24,122	24,120
Shift	-0.15%	-0.20%	-0.23%	-0.26%	-0.29%

As an additional load condition, the load magnitude is fixed at 100%, but the power factor is varied from -cos(45°) to cos(45°). The numerical results for the resonant frequencies are listed in Table 4-3.

This result shows stationary resonant frequencies for the positive power factors, but noticeable changes in the resonant frequencies and the magnitudes of the impedance (|Z| Ω) for the negative power factors as shown in Fig. 4-6. Note that all figures express

power factors by angles for positive ones and adding '-' symbols to angles for negative ones for easier illustration; e.g., 35° means cos(35°) and -35° means -cos(35°).

The magnitude of the impedance decreases with decreasing power factor, because the smaller reactance (i.e., inductance and capacitance) component causes a total impedance decrement.

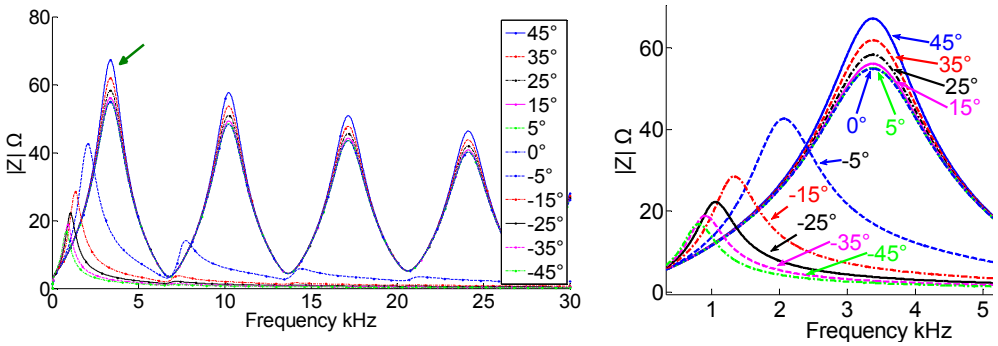

Fig. 4-6 Resonant Frequencies for Various Power Factors (-cos(45°) to cos(45°)).

Table 4-3 Resonant Frequencies (Hz) for Various Power Factors.

Power factor	cos(45°)	cos(35°)	cos(25°)	cos(15°)	cos(5°)	cos(0°)	-cos(0.5°)
1st Peak	3376	3378	3378	3378	3376	3376	3152
2nd Peak	10236	10236	10236	10236	10234	10236	9594
3rd Peak	17162	17162	17162	17160	17162	17160	16170
4th Peak	24124	24124	24124	24124	24124	24124	22856
Shift	-0.03%	0.00%	0.00%	0.00%	-0.03%	-0.03%	-3.30%

Power factor	-cos(1°)	-cos(3°)	-cos(5°)	-cos(15°)	-cos(25°)	-cos(35°)	-cos(45°)
1st Peak	2964	2410	2068	1338	1060	908	812
2nd Peak	9116	8122	7752	7308	7208	7158	7130
3rd Peak	15556	14668	14436	14180	14104	14058	14026
4th Peak	22220	21516	21354	21140	21060	21004	20962
Shift	-6.04%	-14.11%	-19.10%	-29.75%	-33.80%	-36.02%	-37.42%

When the power factor is cos(45°), the resonant frequency moves only 2 Hz from reference resonant frequency (cos(15°) case), but it moves 2,566 Hz (-37.42% shift) for

the power factor -cos(45°) case. As studied in Chapter 3, the large change of the capacitance causes significant impact on resonant frequencies when in negative power factor conditions.

The main capacitive load is a capacitor bank, which controls the power factor in a power system. Most electrical loads consist of inductive loads such as electrical motors and transformers, thus the power system operates in positive power factor condition with compensation by capacitor banks. But this power factor can be over compensated at nighttime with loads decrement, which turns to the negative power factor operation.

(b) Resonant frequencies under various fault positions

A power cable phase-grounding fault condition is simulated by fault resistor R_F insertion in the middle of cable as shown in Fig. 4-1. The R_F is varied from 1 mΩ to 1 kΩ. Fault points are 10% to 90% of the cable length from the source side and the reference load condition (270 MVA, power factor 0.966) is used.

Fig. 4-7 shows resonant frequencies for the 60% fault point with different fault resistors. When the fault resistor is smaller than 1 Ω, new resonant frequencies appear between the first and second resonant frequencies. These new resonant frequencies become more pronounced with lower fault resistance. On the other hand, resonant frequencies are not changed for higher fault resistors (higher than 10 Ω).

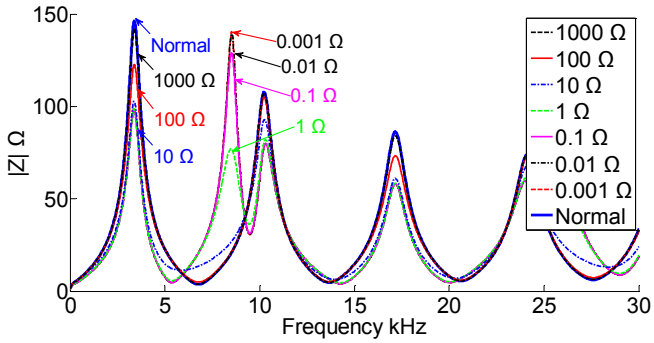

Fig. 4-7 Frequency Responses for Different Fault Resistors (60% Fault Position).

During an actual fault, the R_F is variable with fault current changes and eventually it approaches zero until the circuit breaker cuts the fault current as shown in Fig. 4-8. Variable R_F is known to lead to fault location errors in the impedance based method [72], but this is not an issue in the new passive methodology, because once various fault resistors are small enough to produce discernable new resonant frequencies, they produce identical unique new resonant frequencies for a given fault position.

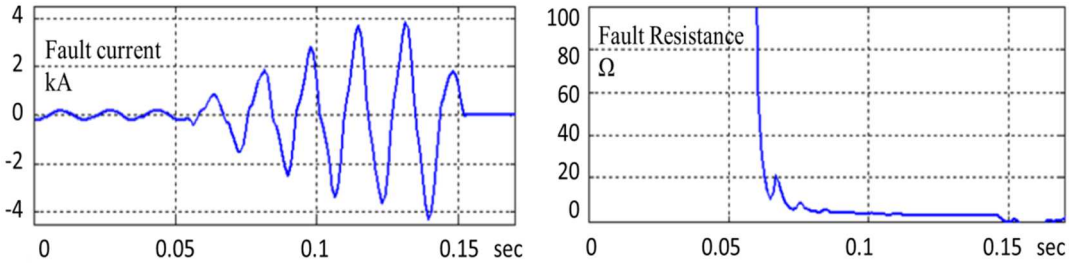

Fig. 4-8 Fault Current (left) and Resistance (right) for a Phase-to-Ground Fault [72].

The behavior of resonant frequencies under different fault points is verified by using the frequency scan for a grounding-faulted cable power system. The fault resistor is set to 1 mΩ for better distinction from the normal case and its point is varied from 0.1 to 0.9.

The frequency-impedance calculation results for different fault points are illustrated in Fig. 4-9 and it shows different new resonant frequencies in accordance with

different fault points. The new resonant frequencies lay between the first and second reference resonant frequencies for 0.1 to 0.5 fault points. However, when the fault points are closer to the load side, the new resonant frequencies are located after the second reference resonant frequency.

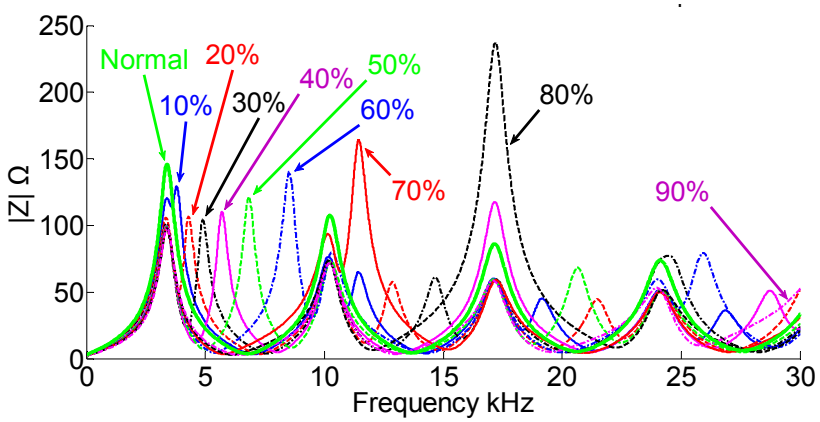

Fig. 4-9 Frequency Responses for Different Fault Positions (R_F = 1 mΩ).

The behavior of the resonant frequencies for different fault positions can be better understood by referring to the 3-D surface plot presented in Fig. 4-10, which places frequency on the x-axis, fault location on the y-axis and the impedance magnitude on the z-axis.

The fault locations are divided into 19 positions for easier analysis and new resonant frequencies are spawn off from the reference resonant frequencies as the fault location moves away from the source.

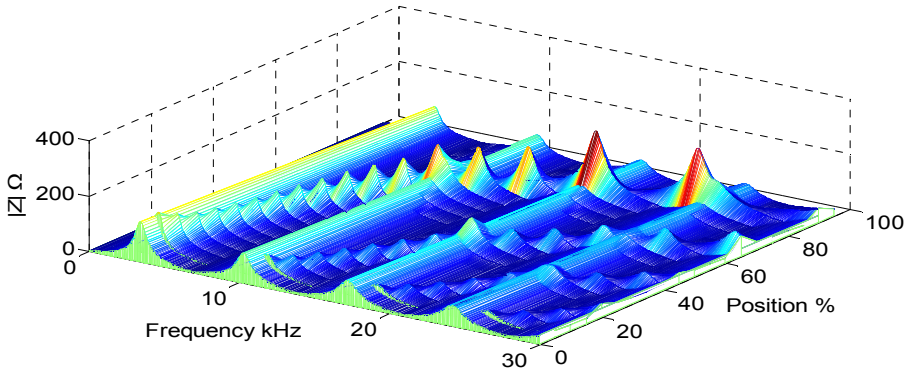

Fig. 4-10 Behavior of Resonant Frequencies as a Function of Cable Fault Position.

For some fault positions, the new resonant frequencies overlap the reference ones, but the combined resonant frequencies have larger gain magnitudes, which enable us to readily recognize the new resonant frequencies as shown in Fig. 4-11.

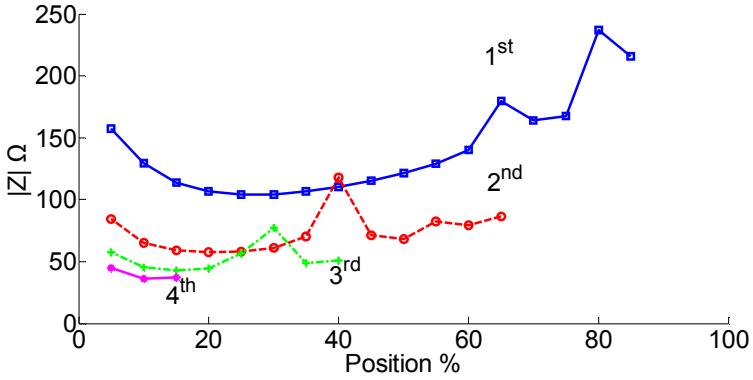

Fig. 4-11 Gain Magnitude of New Resonant Frequencies as a Function of Fault Position.

The collection of these new resonant frequencies is plotted in Fig. 4-12. Because the new resonant frequency at fault position 90% and 95% exceed 30 kHz, they are not shown in this case. To detect hidden new resonant frequencies at positions greater than 80%, the expansion of the frequency bandwidth by shortening the sampling interval is necessary. But if the cable length is long enough, the new resonant frequencies from all

fault points can be detected since a longer cable has smaller resonant frequencies as demonstrated in Fig. 4-4.

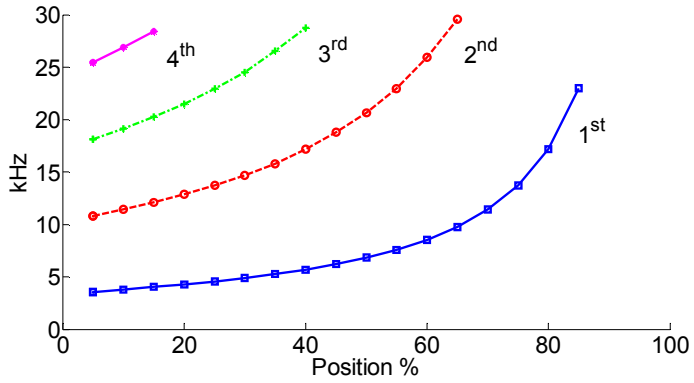

Fig. 4-12 New Resonant Frequencies as a Function of Fault Position.

A fault introduces new resonant frequencies as seen in Fig. 4-12 and the frequencies follow an odd harmonic order behavior much like that exhibited by the reference resonant frequencies. This feature can assist to identify new resonant frequencies among mixed frequency components. Table 4-4 summarizes the resulting new resonant frequencies for different fault positions.

Table 4-4 New Resonant Frequencies (Hz) for Various Fault Locations.

Location	10%	20%	30%	40%	50%	60%	70%	80%	90%
1st Peak	3792	4294	4896	5698	6826	8524	11446	17192	-
2nd Peak	11450	12862	14664	17170	20652	25922	-	-	-
3rd Peak	19156	21484	24484	28740	-	-	-	-	-
4th Peak	26878	-	-	-	-	-	-	-	-

These results verify the theoretical analysis of Eq. (3-35) in the prior chapter, and the first new resonant frequency for this system can be derived as

$$fr_{CF1} \cong \frac{1}{4(1-p)\sqrt{LC}} = \frac{3419}{(1-p)} \tag{4-2}$$

The second new resonant frequency is

$$fr_{CF2} \cong \frac{3}{4(1-p)\sqrt{LC}} = \frac{10258}{(1-p)} \tag{4-3}$$

These equations are in good agreement with simulation results of Table 4-4 with subtle differences, which result from neglecting the load.

However, it is obvious that the power cable fault can be located by comparison between measured (or calculated using known parameters) reference resonant frequencies and detected new resonant frequencies.

On the aspect of accuracy, the matrix of fault locations $P(k)$ can be calculated using the first new resonant frequencies $N_{fr}(k)$ and referring to Eq. (4-2),

$$P(k) \cong \left(1 - \frac{1}{N_{fr}(k)4\sqrt{LC}}\right) l = \left(1 - \frac{3419}{N_{fr}(k)}\right) 10500 \tag{4-4}$$

where, l is cable length (= 10500 m) and $k = 1, 2, 3$ ....

When the new resonant frequency is 3419 Hz, the fault location becomes zero and has a negative distance for resonant frequencies smaller than this value. Therefore, the fault location can be obtained when the new resonant frequencies are higher than $1/\sqrt{LC}$.

For $k = 1$, the first appearing new resonant frequency $N_{fr}(1)$ is 3419 Hz and the corresponding fault location $P(1)$ is zero. Let the fault location step (ΔP), which is the difference between calculated fault locations for frequency step Δf, be

$$\Delta P(k+1) = P(k+1) - P(k), \qquad \Delta f = N_{fr}(k+1) - N_{fr}(k) \tag{4-5}$$

In this case, the Δf is 2 Hz and the $\Delta P(k+1)$ has its maximum value (= 6.14 m) at the second appearing new resonant frequency, $N_{fr}(2) = 3419 + \Delta f = 3412$ Hz, as shown in Fig. 4-13.

Therefore, 6.14 m is the theoretical maximum error for fault location, and this error is dependent on frequency step and cable parameters L and C. In addition, the minimum fault location error is 7.98 cm at 30 kHz; $P(30000 \text{ Hz}) - P(29998 \text{ Hz}) = 9303.35 - 9303.27 = 0.00798$ m.

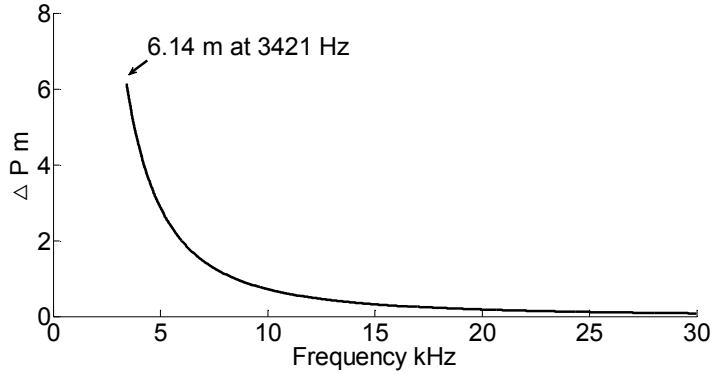

Fig. 4-13 Fault Location Step (ΔP) with New Resonant Frequencies.

From these results, the maximum fault location error, ΔP_{max}, can be obtained for given frequency step Δf,

$$\Delta P_{max} = \left(1 - \frac{3419}{3419 + \Delta f}\right) 10500 \tag{4-6}$$

This ΔP_{max} can be considered as minimum accuracy for given frequency step. In other words, when the frequency step is 0.33 Hz, it gives at least 1 m accuracy on fault location and higher new resonant frequencies give higher accuracies.

4.2.2 TR Power System

Three 10.2 kV / 154 kV step up transformers (116 MVA, 116 MVA, 58 MVA) for high voltage transmission are connected between the generators and power cable as shown in Fig. 4-14.

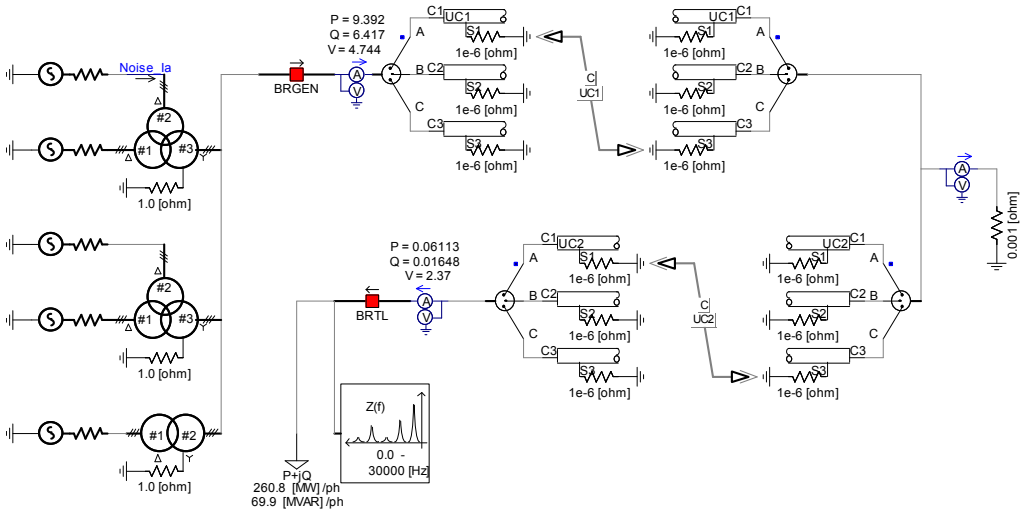

Fig. 4-14 PSCAD Simulation for TR Power System.

The resonant frequencies found using the frequency scan on the TR power system are compared with that of the cable power system in Fig. 4-15, and the resonant frequencies are 102, 6848, 13720, 20660, and 27632 Hz.

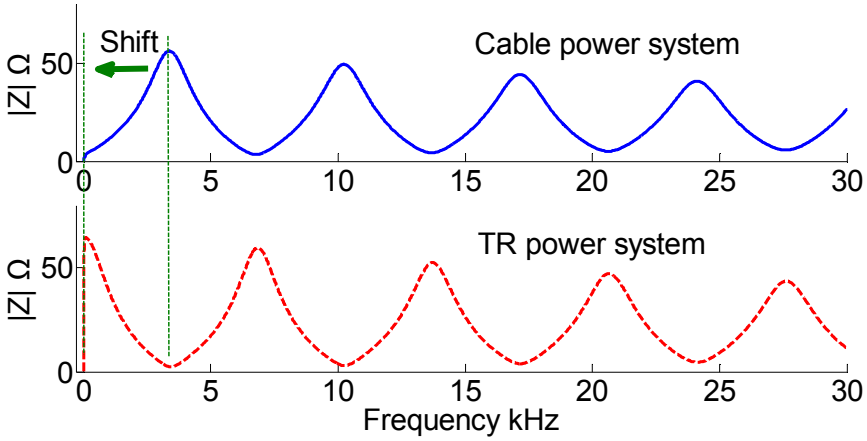

Fig. 4-15 Resonant Frequency Shift in TR Power System.

The first peak frequency of 102 Hz results from the $\cosh(\gamma l)$ term in Eq. (3-39) and it is hard to discriminate from the 60 Hz harmonics and other unknown low frequency components; therefore, we regard the second peak frequency, 6848 Hz, as the first observable resonant frequency.

Considering 3378 Hz is the first resonant frequency for the cable power system, the approximate resonant frequency for the TR power system is 6756 Hz (= 3378 * 2) by Eq. (3-21) and (3-40). This is close to the first resonant frequency 6848 Hz with a small difference (92 Hz), which is caused by the approximate calculation neglecting the $\cosh(\gamma l)$ term.

However, these results verify the prior theoretical studies in Chapter 3 that the TR shifts the resonant frequency of cable power system approximately by the value of the first resonant frequency.

(a) Resonant frequencies under various load conditions

The behavior of the resonant frequencies under various loads in the TR power system is studied using the frequency scan tool in PSCAD and the load conditions are the same as the cable power system cases of 10% to 100% of 270 MVA and the power factor is cos(15°).

The resulting resonant frequencies are depicted in Fig. 4-16 and it shows a similar behavior with the cable power system cases in Fig. 4-5 in that the resonant frequencies are nearly constant under variable loads. In other words, the shifted resonant frequencies under various loads for the cable power system are very close to that of the TR power system.

The resonant frequencies under different power factors from -cos(45°) to cos(45°) show an identical behavior with the cases of the cable power system as shown in Fig. 4-17. The resonant frequencies are nearly constant for positive power factors, but show considerable movements for negative power factors. The similarity with the cable power system and shift effect in the TR power system can be better understood when Fig. 4-17 is compared with power cable case, Fig. 4-6.

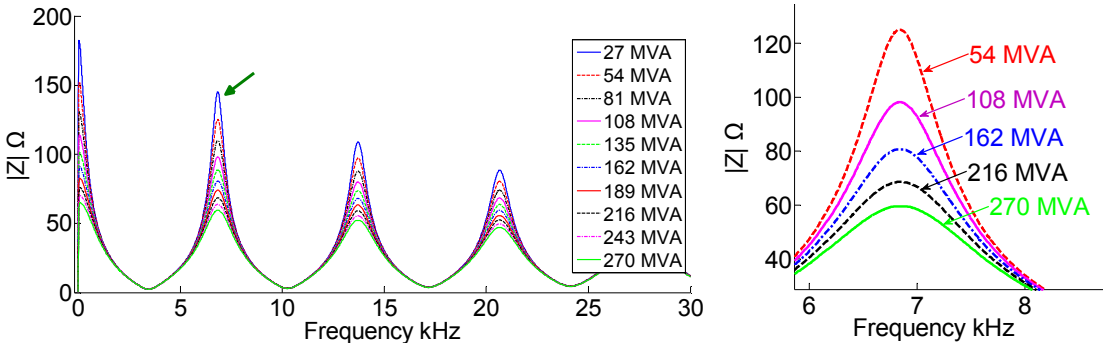

Fig. 4-16 Resonant Frequencies for Various Loads (TR Power System).

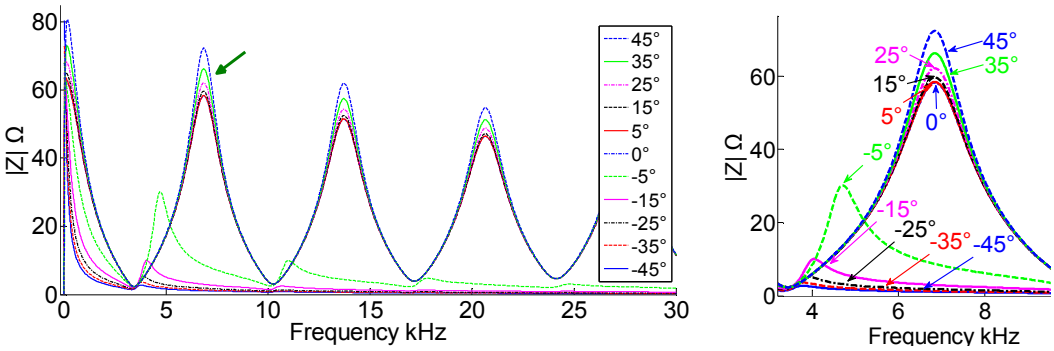

Fig. 4-17 Resonant Frequencies for Various Power Factors (TR Power System).

(b) Resonant frequencies under various fault positions

The results of the frequency-impedance calculation using the frequency scan for the faulted (R_F = 1 mΩ) TR power system with different fault positions are shown in Fig. 4-18, and its new resonant frequencies are listed in Table 4-5.

Comparing these new resonant frequencies with those of the previous cable power system fault cases (Fig. 4-9 and Table 4-4), the new resonant frequencies in both cases are very close to each other. The differences between these two cases are calculated in Table 4-6 and the largest difference in the first resonant frequency is 54 Hz at the 20% fault position.

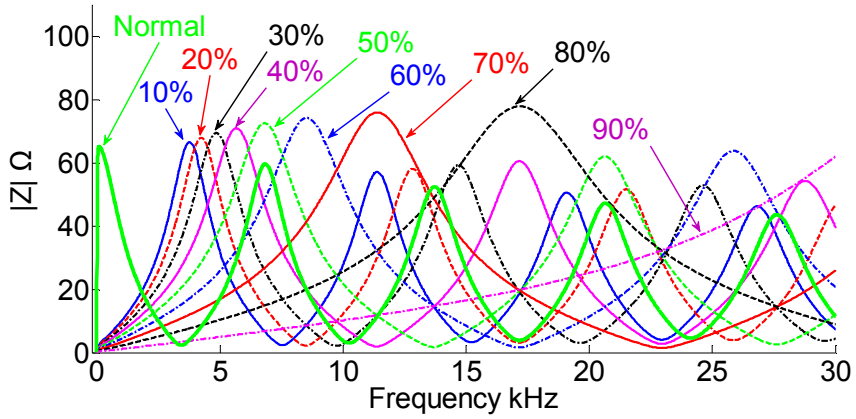

Fig. 4-18 Resonant Frequencies for Various Fault Locations (TR Power System).

Table 4-5 New Resonant Frequencies (Hz) for Various Fault Locations (TR Power System).

Location	10%	20%	30%	40%	50%	60%	70%	80%	90%
1st Peak	3746	4240	4852	5678	6854	8502	11398	17156	-
2nd Peak	11390	12842	14664	17162	20658	25886	-	-	-
3rd Peak	19100	21494	24624	28758	-	-	-	-	-
4th Peak	26854	-	-	-	-	-	-	-	-

Table 4-6 Resonant Frequency Differences between TR and Cable Power System (Hz).

Location	10%	20%	30%	40%	50%	60%	70%	80%	90%
1st Peak	28	54	44	20	-28	22	48	36	-
2nd Peak	60	20	0	8	-6	36	-	-	-
3rd Peak	56	-10	-140	-18	-	-	-	-	-
4th Peak	24	-	-	-	-	-	-	-	-

4.3 Frequency Analysis on Artificial Power Signals

4.3.1 Frequency Analysis and Noise

This section verifies characteristics of the resonant frequencies using frequency analysis on artificial power signals produced from PSCAD simulations. Various loads and fault points conditions are simulated for both cable and TR power systems and the power spectral density (PSD) for the resulting voltage and current signals are analyzed.

The power spectral density (PSD) tells us where the average power is distributed as a function of frequency. In other words, the PSD shows at which frequency variations are strong or weak. The PSD, $S_x(f)$, can be expressed as average power of signal $x(t)$ and is defined in terms of Fourier transform, $x_F(\omega)$ [73] [74],

$$S_x(f) = \lim_{T\to\infty} \mathbf{E}\{|x_F(\omega)|^2\} = \lim_{T\to\infty} \mathbf{E}\left\{\frac{1}{2T}\left|\int_{-T}^{T} x(t)e^{-j\omega t}dt\right|^2\right\} \tag{4-7}$$

Here $\mathbf{E}$ denotes the expected value as [74]

$$\mathbf{E}[|x_F(\omega)|^2] = \mathbf{E}\left[\frac{1}{T}\int_0^T x^*(t)e^{j\omega t}dt \int_0^T x(\tau)e^{-j\omega\tau}d\tau\right] \tag{4-8}$$

where x^* denotes the complex conjugate of x. Also, this PSD is equivalent with the Fourier transform of the auto-correlation function (R_x) as [74]

$$S_x(f) = \int_{-T}^{T} R_x(\tau)e^{-j\omega t}dt, \qquad R_x(\tau) = \mathbf{E}\{x(t)x^*(t+\tau)\} \tag{4-9}$$

The input signal, source voltage V_s, is transformed to the frequency domain by fast Fourier transform (FFT), and then this is multiplied by the transfer function in order to obtain the output signal, load voltage V_R, in the frequency domain.

$$V_R(s) = H_E(s)V_S(s) \tag{4-10}$$

In an ideal condition, the source voltage is a pure 60 Hz sine wave, thus only the 60 Hz component of frequency will be shown in the load voltage because the frequency response is dependent on the frequency composition of the source voltage and transfer function. In other words, an additional input signal containing a spread frequency spectrum (e.g., a sweep signal) is required to reveal resonant frequency components in the output signal.

To overcome this problem, we focus on inherent normally distributed fluctuations (so called white noise) in the power system, because their power spectral density, $S_{XX}(f)$, is constant (flat) across the entire frequency spectrum by Weiner Khintchine Theorem [75]

$$S_{XX}(f) = \int_{-\infty}^{\infty} \sigma^2 \delta(\tau) e^{-j2\pi f\tau} d\tau = \sigma^2 \tag{4-11}$$

where σ^2 is the signal variance, and $\delta(\tau)$ is the unit impulse sequence.

Thus, the noise will act as a testing input signal as described in Fig. 4-19, and this is proved by Matlab calculation and PSCAD simulation.

The source voltage signal, V_s is provided with noise as follows,

$$V_s(t) = \sqrt{2} \cdot 154 \cdot 10^3 \cdot \sin(2\pi \cdot 60 \cdot t) + noise(t), \qquad 0 \le t \le 1 \tag{4-12}$$

The noise signal is generated using the normally distributed pseudorandom number function in Matlab and added to the source voltage. In terms of noise level, the percentage of source voltage peak is used for an easy interpretation of noise magnitude. For example, 1% noise level means random numbers that are randomly distributed at every time instant within ±1% (= ±2.178 kV) of the source voltage peak (= $\sqrt{2} \cdot 154$ kV).

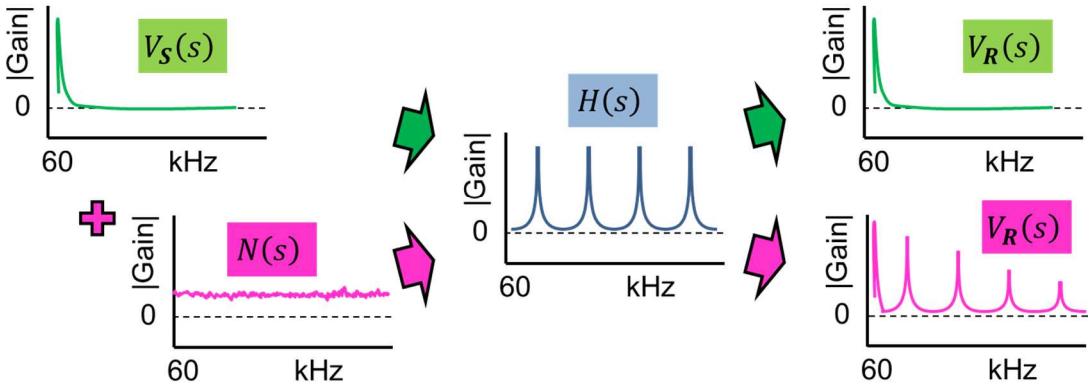

Fig. 4-19 Contribution of Noise in Frequency Analysis.

Fig. 4-20 shows frequency spectrums of the source voltage, load voltage and the transfer function. The source voltage is a pure 60 Hz sine wave without noise and the resulting frequency spectrum of the load voltage is very small values that can be considered as zeros except a 60 Hz component. In the graph, the source voltage spectrum is multiplied by 10^5 to avoid curve overlay.

In contrast, Fig. 4-21 shows frequency spectrums for 0.1% noise contained source voltage. Obviously, the resonant frequencies are found in the spectrum of load voltage and these frequencies are identical to those of the transfer function.

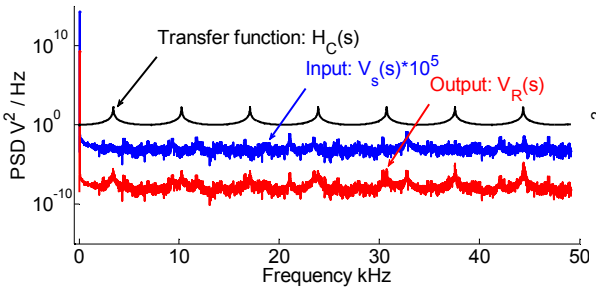

Fig. 4-20 Spectrums for Noiseless V_S.

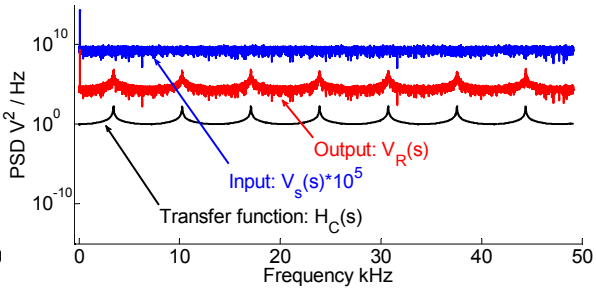

Fig. 4-21 Spectrums for Noised V_S.

Now, it is apparent that the noise adds all components of frequencies to the source voltage signal and it enables the transfer function to be reflected in the load voltage signal, and then we can obtain the resonant frequencies from the load voltage signal without knowledge of a deterministic input signal.

The result of Fig. 4-21 shows that the noise in the source voltage plays a key role in obtaining the resonant frequencies from the load voltage. Therefore, whether the transmission system has sufficient noise sources is one of the issues for this new passive methodology.

Similar studies are implemented using PSCAD as shown in Fig. 4-22. A 10 μs sampling rate is used to obtain high frequency spectrum resolution as 50 kHz bandwidth.

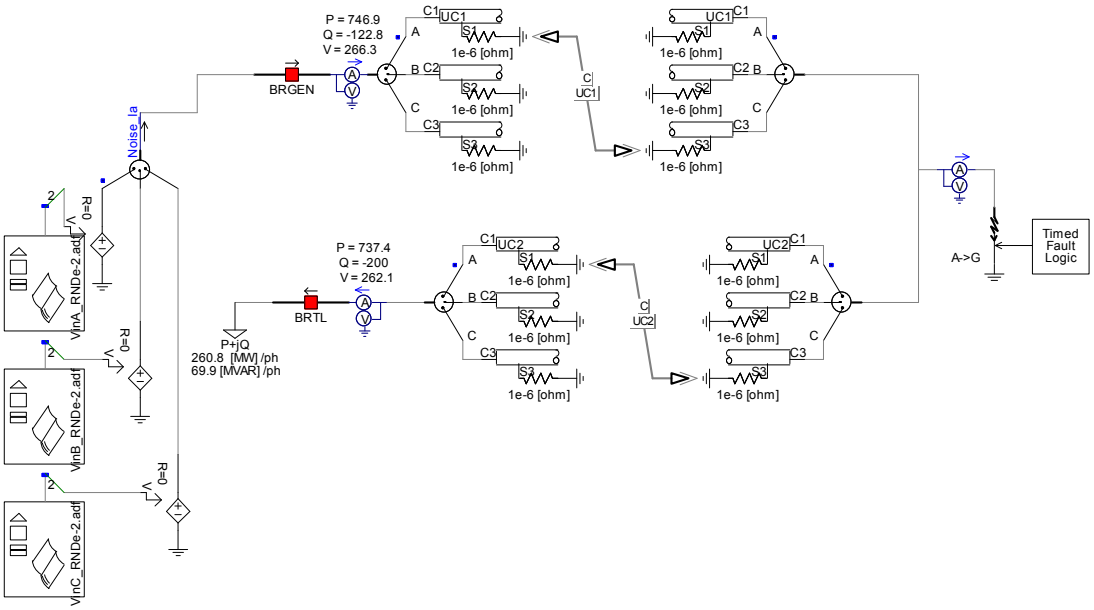

Fig. 4-22 Simulation Circuit with Noise Contained Voltage Source.

The noise contained external voltage signal is injected into the power cable using voltage input modules. These voltage signals are generated by Matlab, and from 0.2% to 1% noise levels are tested to find the minimum noise level for discernible frequency analysis.

Under the reference load condition (270 MVA, power factor 0.966), the frequency spectrums of the load voltage for different noise levels are depicted in Fig. 4-23. It is quickly noted that higher noise levels in the source voltage lead to a more pronounced appearance of the resonant frequencies in the spectrum.

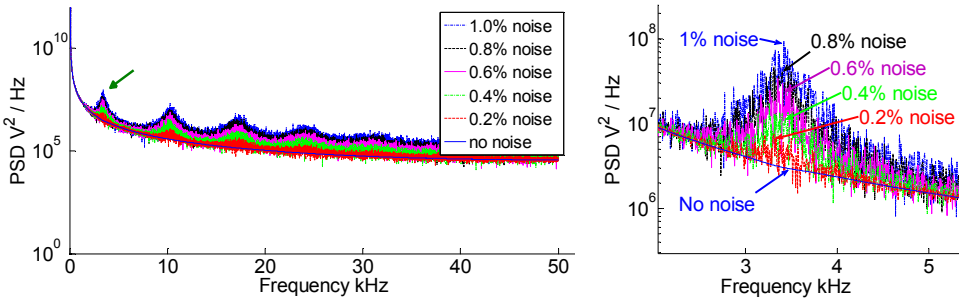

Fig. 4-23 Frequency Spectrum of V_R for Different Noise Levels.

Consequently, when the noise level is lower than 0.4%, it is not easy to distinguish the resonant frequencies in the spectrum. The resonant frequencies are attenuated and flattened in the higher frequency ranges, so it is very difficult to differentiate them after the fourth resonant frequency.

These results are a bit different from the earlier theoretical analysis results that a 0.1% level of noise is sufficient to recognize the resonant frequency and does not have an attenuation of peaks. The main reason for this difference is that the PSCAD simulation case has a connected electrical load and includes the attenuation factor (e.g., losses) in circuits.

4.3.2 Cable Power System

The characteristics of resonant frequencies under various power system conditions are verified by frequency analysis for the PSCAD simulation power signals.

(a) Resonant frequencies under various load conditions

The frequency spectra of the load voltage, V_R for the different load conditions (from 10% to 100% of 270 MVA) with a power factor of 0.966 (= cos15°) are shown in Fig. 4-24. In addition, the frequency spectrum of the source current I_S is shown in Fig. 4-25.

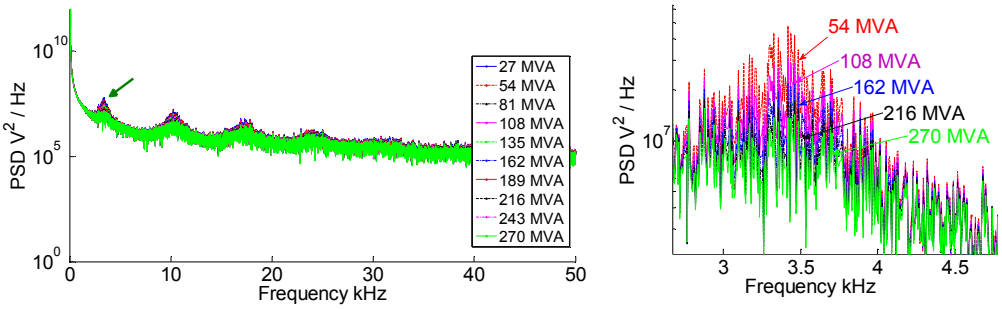

Fig. 4-24 Frequency Spectrum of V_R for Various Loads.

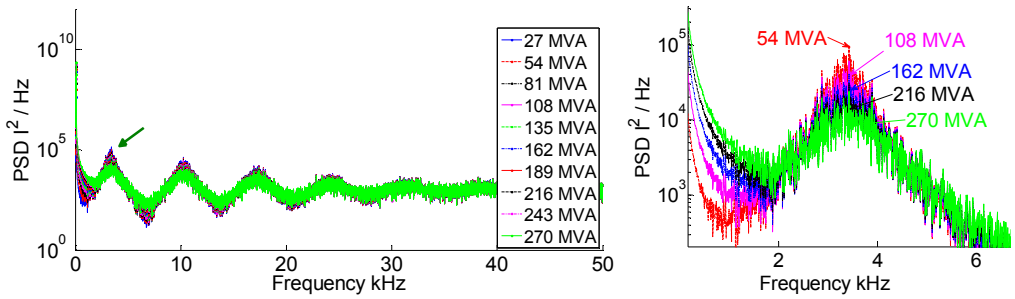

Fig. 4-25 Frequency Spectrum of I_S for Various Loads.

Both cases show nearly constant resonant frequencies for the load changes. Also, the graphs show the increment of gain magnitudes with the decrement of loads, which results from the fact that the same magnitude of noise is relatively bigger and more effective for smaller voltage and current signals.

Because the current signal is more sensitive to power system conditions than the voltage signal, the source current gives clearer results within the frequency spectrums for differentiating resonant frequencies as shown in Fig. 4-25. However, the effective signal for resonant frequency analysis can be obtained on both ends of the cable: source and load.

The resulting frequency spectrum of the load voltages with 270 MVA load and different power factors (from -45° to 45°) is shown in Fig. 4-26.

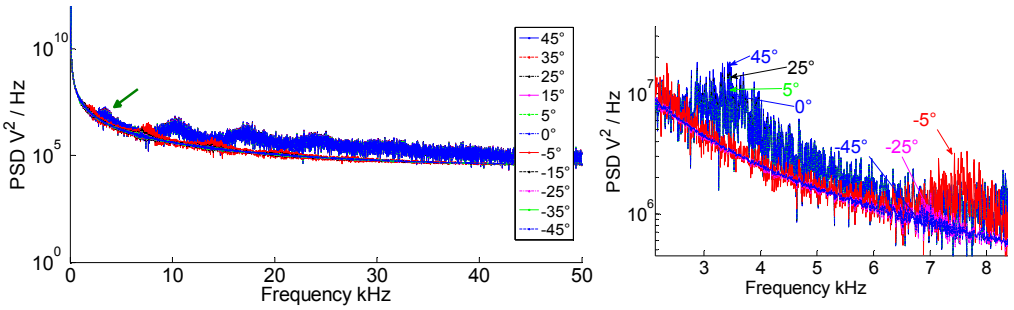

Fig. 4-26 Frequency Spectrum of V_R for Various Power Factors.

Similar to the results of the previous study using the frequency-impedance scan, the resonant peak frequencies are nearly stationary for positive power factors (i.e., inductive loads), but in the negative power factor cases (i.e., capacitive loads), the resonant peak frequencies decrease noticeably as 2124 Hz for -cos(5°), 1099 Hz for -cos(25°) and 842 Hz for –cos(45°). These resonant frequency characteristics are more apparent in the frequency spectrum of the source currents as shown in Fig. 4-27.

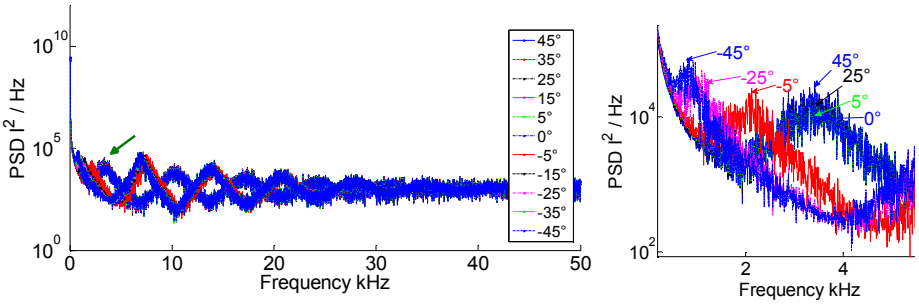

Fig. 4-27 Frequency Spectrum of I_S for Various Power Factors.

(b) Resonant frequencies under various fault positions

The resonant frequency characteristics for different fault positions (10% to 90%) are verified by PSCAD simulation. A ground fault is triggered at 0.5 sec with a 1 mΩ fault resistor. The circuit breaker on the source side (BRGEN in Fig. 4-22) starts its operation to cut fault current after 20 ms (=1.2 cycles) and it opens the circuit at the moment of zero current, 0.527 sec.

The measured fault signals (V_S, V_R, I_S and I_R) are depicted in Fig. 4-28 with the data segment that is selected for frequency analysis. This segment has 2^{11} data points and it consists of 58.6% fault signal and 41.4% normal condition signal by time.

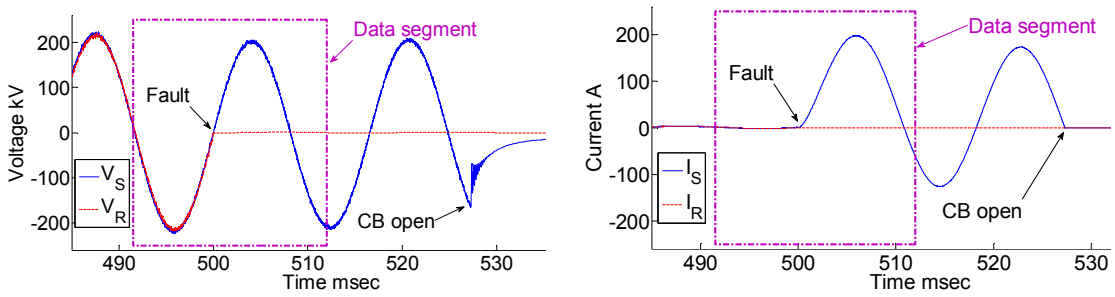

Fig. 4-28 Fault Signal and Data Segment (npts = 2^{11}, Fault Data = 58.6% Segment).

The frequency spectrum of these fault signals is depicted in Fig. 4-29 and all curves are vertically shifted by successive multiplication with some factor (e.g., 100) for effective comparison except the plot of the normal case, which is placed on the bottom, and this method is applied to all graphs for spectrum comparison.

The behavior of the resonant frequencies for different fault positions is shown in the source current signal, while it is hard to differentiate changes of resonant frequencies in the other signals. That is caused by insufficient fault data, which is related to the fault duration time and segment selection.

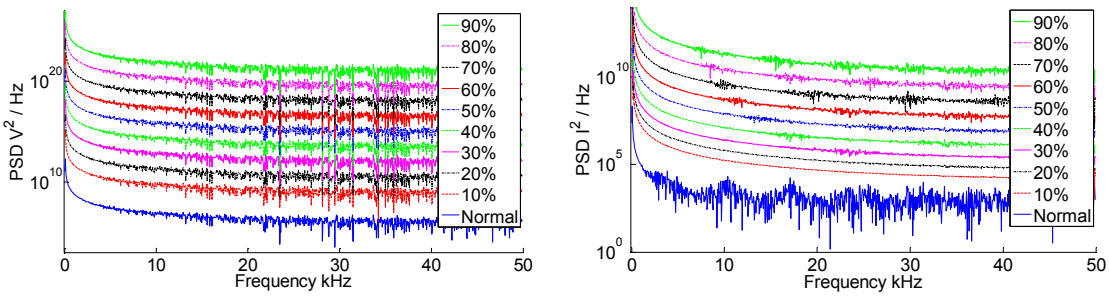

(a) Spectrum for V_S (b) Spectrum for I_S

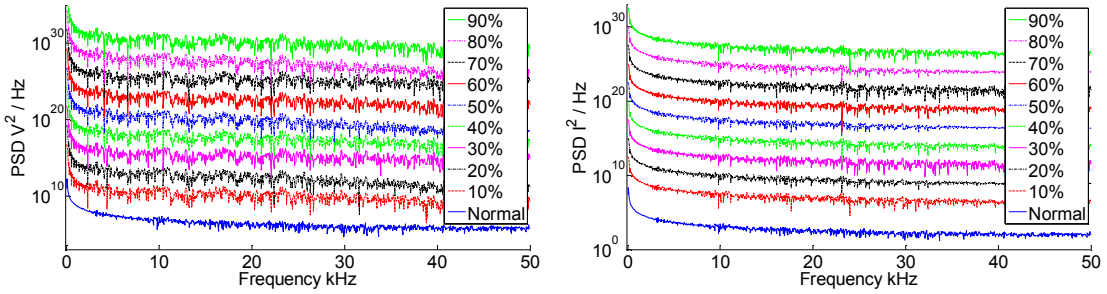

(c) Spectrum for V_R (d) Spectrum for I_R

Fig. 4-29 Frequency Spectrum of Fault Signals (npts = 2^{11}).

When the data segment after the previous case is selected, it contains fault data in 74.6% of the segment as shown in Fig. 4-30.

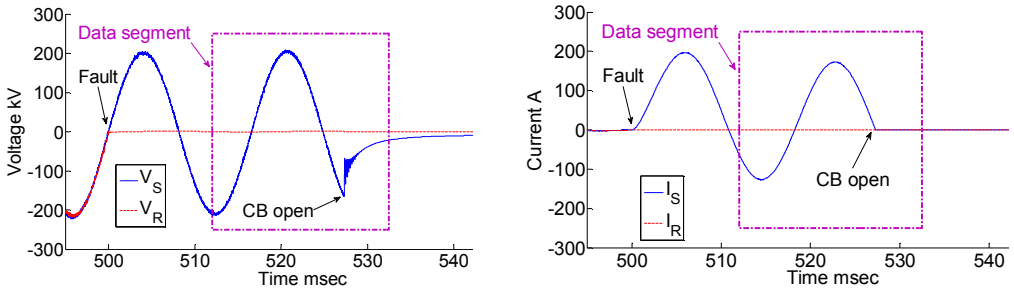

Fig. 4-30 Fault Signal and Data Segment (npts = 2^{11}, Fault Data = 74.6% Segment).

With a similar analysis, Fig. 4-31 provides the results of the frequency spectrum for this segment data, which contains 74.6% fault signal.

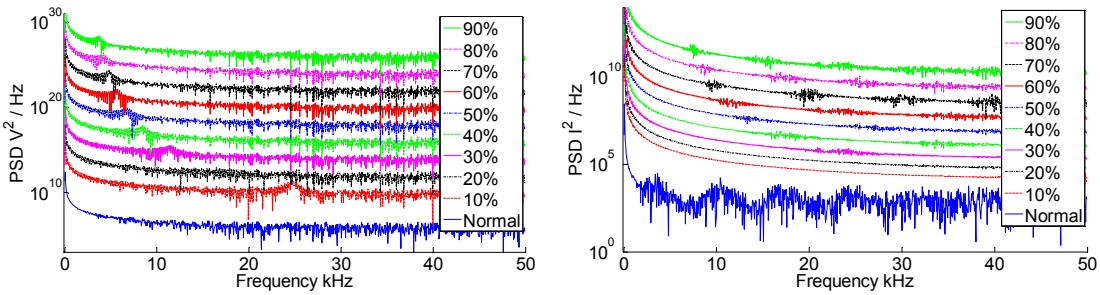

(a) Spectrum for V_S

(b) Spectrum for I_S

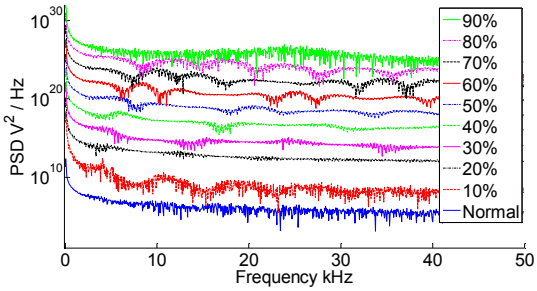

(c) Spectrum for V_R

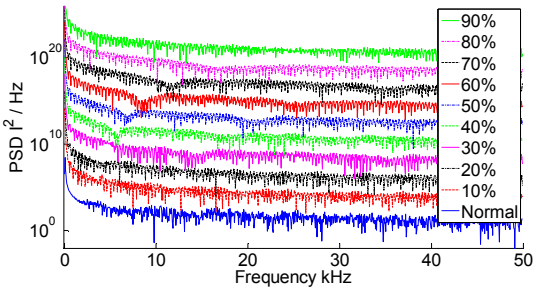

(d) Spectrum for I_R

Fig. 4-31 Frequency Spectrum of Fault Signals (npts = 2^{11}).

All spectrums show resonant frequency behavior for different fault positions and it is found that the source side signals are more sensitive to the fault conditions and give clearer discrimination of resonant frequencies.

Fig. 4-32 shows expanded data segments that have a larger number of fault data points, specially 2^{12} from 50 msec (3 cycles) fault condition with a 1 Ω fault resistor.

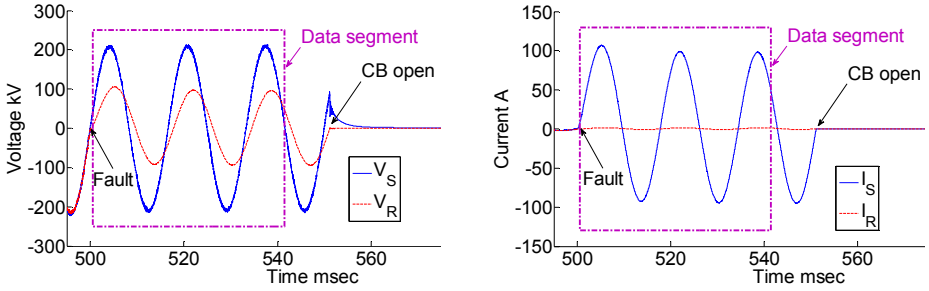

Fig. 4-32 Fault Signal and Data Segment (npts = 2^{12}, Fault Data = 100% Segment).

The frequency spectrums for this expanded segment is shown in Fig. 4-33. As our expectation, the resonant frequencies are more discernable.

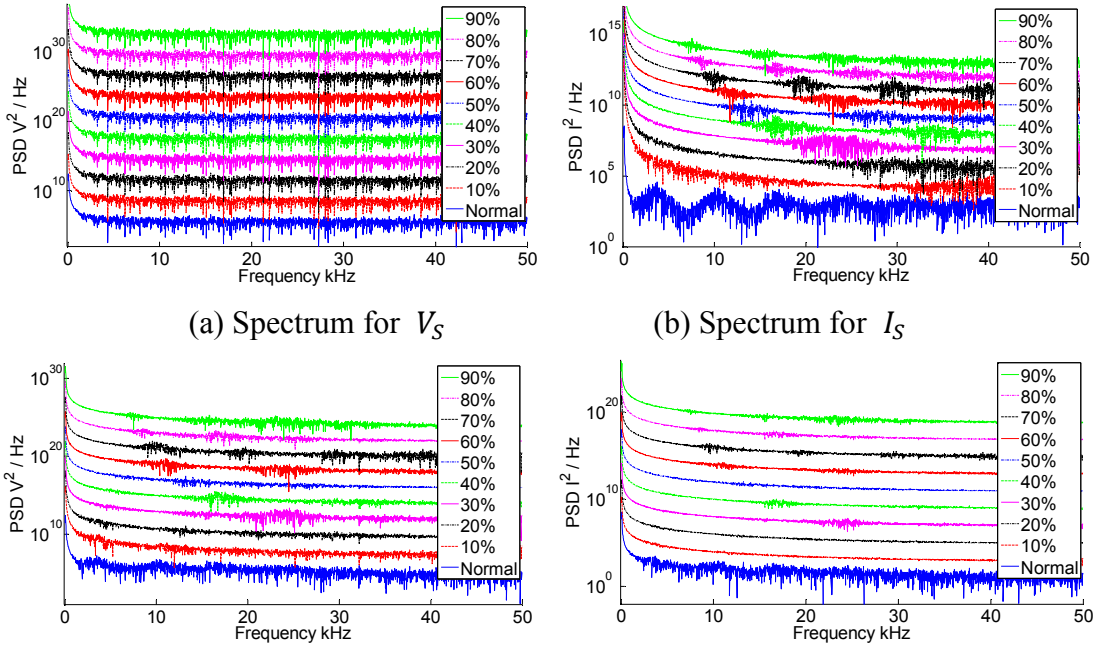

(a) Spectrum for V_S (b) Spectrum for I_S

(c) Spectrum for V_R (d) Spectrum for I_R

Fig. 4-33 Frequency Spectrum of Fault Signals (npts = 2^{12}).

From the results of the fault signal frequency spectrum, it can be stated that the resonant frequencies in fault signal give information about the fault position and its accuracy can be improved by proper fault signal selection.

4.3.3 TR Power System

(a) Filtering effect by transformer

A power transformer has inherent internal characteristics of capacitance, resistance and leakage inductance. The considerable leakage inductance in the primary winding is related to the primary flux that is not shared with the secondary winding. This inductance is based on the air gap, as the thicker the air gap, the lower the leakage

inductance [76]. The internal capacitance and inductance act as a filter to attenuate noise and removes high frequency.

Each generator in the simulation model for the TR power system (Fig. 4-14) is substituted with a 10.2 kV voltage source including 1% level noise. Fig. 4-34 and Fig. 4-35 show signals which are measured on both sides of the transformer; i.e., V_{Gen} and I_{Gen} are at the low voltage side, V_S and I_S are at the high voltage side of the transformer. It can be seen that the transformer attenuates noises in the V_{Gen} and I_{Gen}.

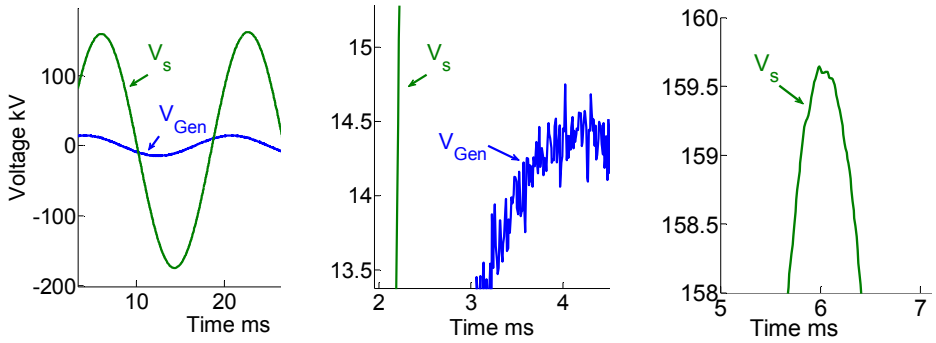

(a) V_{Gen} and V_S (b) V_{Gen} (before TR) (c) V_S (after TR)

Fig. 4-34 Filtered Voltage Signal by TR; Before (V_{Gen}) And After (V_S).

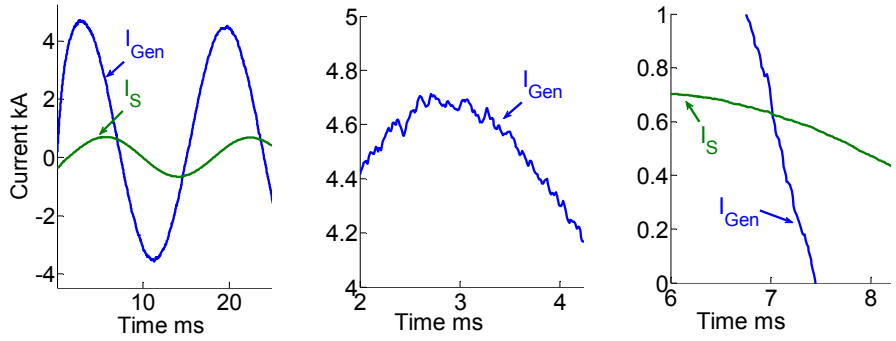

(a) I_{Gen} and I_S (b) I_{Gen} (before TR) (c) I_S (after TR)

Fig. 4-35 Filtered Current Signal by TR; Before (I_{Gen}) And After (I_S).

(b) Resonant frequencies under various load conditions

Fig. 4-36 shows the frequency spectrum (npts = 2^{14}) for V_R and I_S signals under various loads in the TR power system. Comparing to spectrums of the cable power system in Fig. 4-24 and Fig. 4-25, the resonant frequencies are hardly discernible due to the noise reduction effects in the TR power system signals.

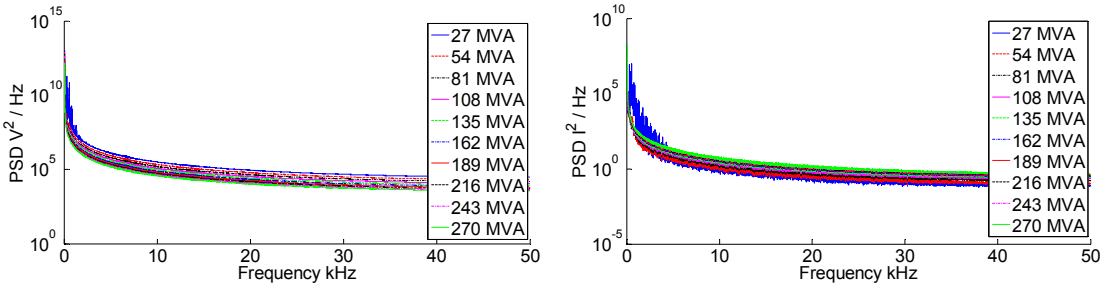

Fig. 4-36 Spectrum of V_R (Left) and I_S (Right) for Various Loads (TR Power System).

Also, the frequency spectrum (npts = 2^{14}) for V_R and I_S signals under various power factors (from -cos(45°) to cos(45°)) in the TR power system is shown in Fig. 4-37, and these are not easy to differentiate resonant frequencies either.

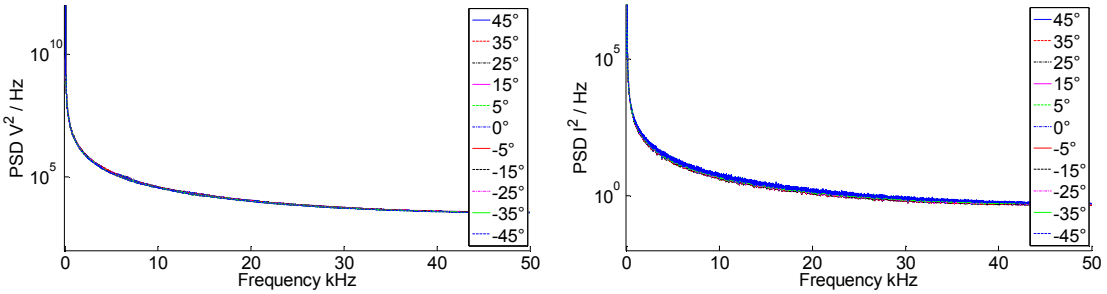

Fig. 4-37 Spectrum of V_R (Left) and I_S (Right) for Various Power Factors (TR Power System).

(c) Resonant frequencies under various fault positions

The same fault simulation process is applied to the TR power system. The ground fault with a 1 mΩ fault resistor is triggered at 0.5 sec and the source side circuit

breaker starts its operation 20 ms after fault. The 2^{11} samples of the data segment are selected to be the same as the previous case that contains 58.6% fault data in the segment.

Fig. 4-38 plots the frequency spectrums for fault signals and it shows new resonant frequency behaviors along with fault positions. Especially the source voltage shows good discernible shapes for the resonant frequencies.

The new resonant frequencies look reversed from each other when comparing source and load side spectrums, which means that the new resonant frequency is the smallest at 90% fault position for a source side signal but this is opposite for load side signals. This can be explained with impedance estimation. When the measuring point is on the load side, the impedances on the source side, including fault resistor are nearly zero due to the very small fault resistor, thus new resonant frequencies are dependent mostly on load side impedances and vice versa.

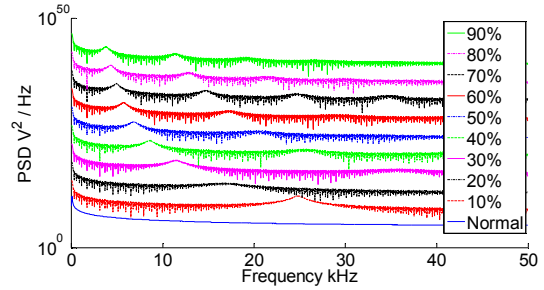

(a) Spectrum for V_S

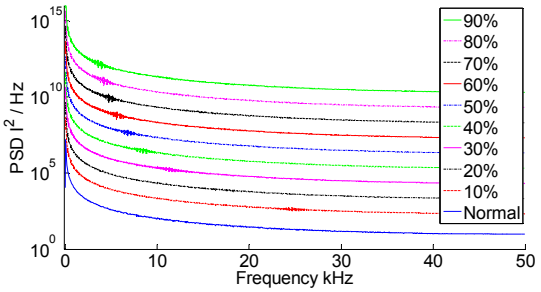

(b) Spectrum for I_S

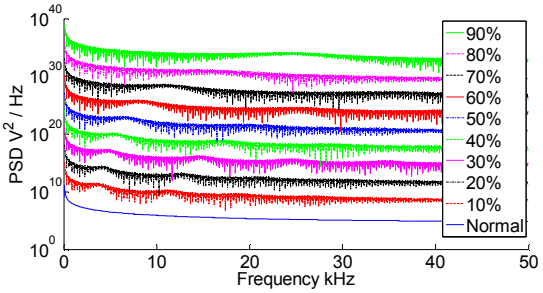

(c) Spectrum for V_R

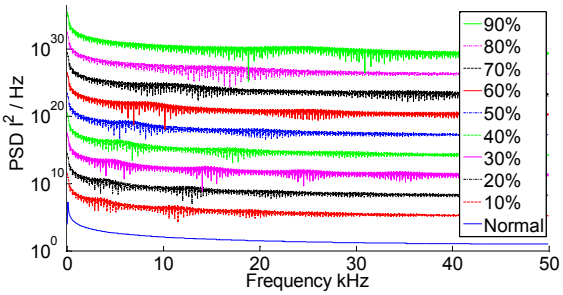

(d) Spectrum for I_R

Fig. 4-38 Frequency Spectrum of Fault Signals (TR Power System, npts = 2^{11}).

The TR power system more closely represents a real power system than the cable power system. The resonant frequencies are different between the TR power system and the cable power system, but their characteristics under various load conditions and fault positions are identical to each other. The filtering effect of the TR attenuates noise in the signal and it causes difficulties in resonant frequency distinction for various load conditions, but the fault signals show moderate resonant frequencies behaviors in accordance with fault positions.

4.4 Improving Resonant Frequency Discernment

Some frequency analysis results (especially in the TR power system) do not have sufficient precision to distinguish the resonant frequencies and these problems can be improved by applying a window function to the signals.

This section studies about windowing signals for better resonant frequency discernment. Mainly five window functions (Blackman, Haming, Hann, Kaiser and Rectangular) are applied to signals, which are used in previous cases and their results are compared.

4.4.1 Leakage Effect and its Reduction

One of the important drawbacks of the FFT is the effect of leakage, which occurs when the FFT is computed from a block of non-periodic time frame data. Theoretically, it is possible to obtain a perfect FFT without any leakage when the sampled data begin and end at the same phase of the signal.

This can be done using a sampled data set whose length is an integral number of wavelengths as shown in Fig. 4-39, which is sampled for exactly 3 cycles of the power frequency. Otherwise, Fig. 4-40 shows the leakage effect when 3.5 cycle data are sampled for FFT analysis [77] [78].

But it is not easy to obtain exact cycled data, which satisfy both sampling interval Δt and data points (npts = 2^n) requirements for real conditions; e.g. for 2^{14} npts, ts should be 1.017 μs, 3.052 μs, 5.086 μs, 7.121 μs, or 9.155 μs and so forth.

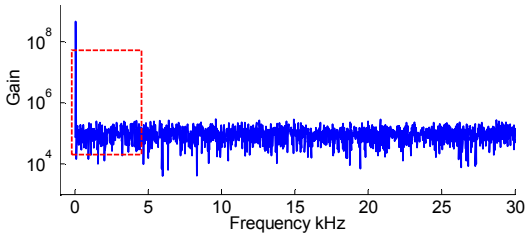

Fig. 4-39 Perfect FFT (No Leakage Effect).

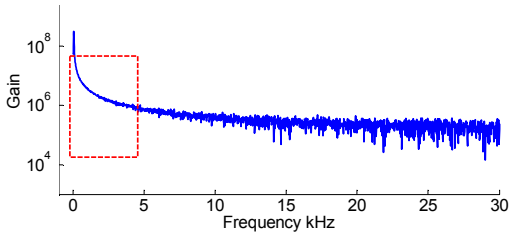

Fig. 4-40 Leakage Effect.

The zero padding method is known as one way of reducing leakage effects. It consists of using an integer number of 60 Hz cycles data and zeros for remainder; e.g., a segment of 2^{17} (= 131072) data points contains 78 cycles of signal data and 1072 points of zeros (= 0.8% segment data) for 10 μs sampling interval condition.

The leakage effect can be reduced by using the appropriate window function, which removes the discontinuity of the measured signal. This window function, $W(t)$ for the signal x, can be defined in the time domain and frequency domain as,

$$x^w(t) = x(t) * W(t), \qquad X^w(f) = X(f) \otimes \mathrm{W}(f) \tag{4-13}$$

The time series values from the window function are multiplied to the original signal before executing the FFT. Usually the shape of window function starts and ends with zero, and maximizes at the center of the time series values [79].

4.4.2 Windowing Signals in Cable Power System

Five window functions are applied to the voltage and current signals on both source and load sides for 100% (270 MVA) load and power factor cos(15°) condition. Their frequency spectrums are graphed in Fig. 4-41 (npts = 2^{14}).
Every windowed signal shows a good performance for the leakage effect reduction, and a great improvement in resonant frequency discernment. Mostly the Hann, Hamming and Blackman window functions show a very good shape of the resonant frequencies.

When the Hann window function is applied to V_R and I_S signals under various power factor (-cos(45°) to cos(45°)) conditions, they are very clear for monitoring the behavior of the resonant frequencies as shown in Fig. 4-42. Stationary resonant frequencies are found for positive power factors and considerable changes observed for negative power factors. All plots are distributed in accordance with orders of legend on the right side (i.e. the top is for the +45° case and bottom is for the -45° case) and this applies to all figures in the document.

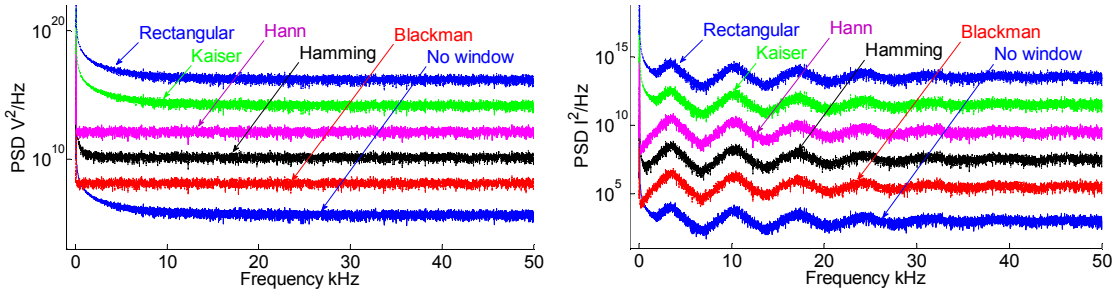

(a) Spectrum for Windowed V_S (b) Spectrum for Windowed I_S

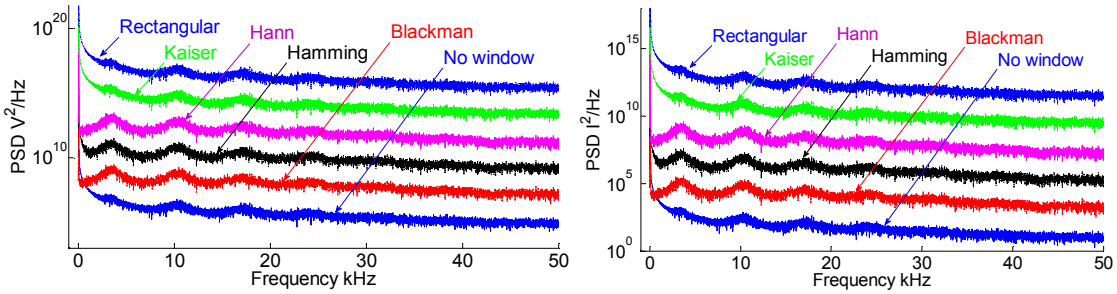

(c) Spectrum for Windowed V_R (d) Spectrum for Windowed I_R

Fig. 4-41 Spectrum of Windowed Signals.

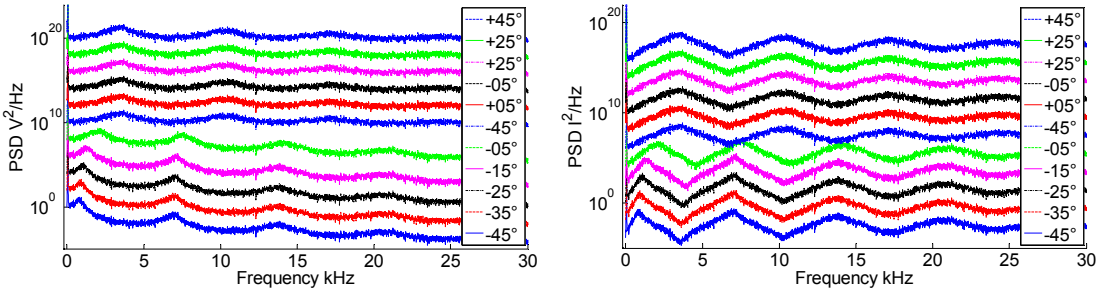

Fig. 4-42 Spectrum of Hann Windowed V_R(Left) and I_S(Right) for Various Power Factors.

Also, the window function can improve the accuracy for cable fault location as shown in Fig. 4-43, which represents frequency spectrums (npts = 2^{11}) for Hann windowed load voltage and source current with various fault positions. This can be better understood when they are compared with the previous case in Fig. 4-31 for which the same fault data segment is used.

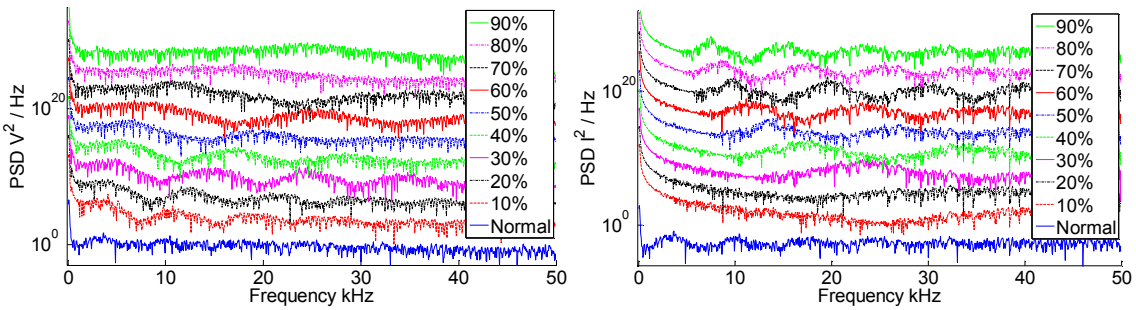

Fig. 4-43 Spectrum of Hann Windowed V_R(left) and I_S(right) for Various Fault Locations.

4.4.3 Windowing Signals In TR Power System

The effectiveness of the window function is more apparent when it is applied to noise reduced signals in the TR power system as shown Fig. 4-44. Without the window function as shown in the case of 'No window' on the bottom of the graphs, it is nearly impossible to distinguish the resonant frequencies, but the Hann and Blackman window functions show an obvious improvement for resonant frequency extraction. The windowed source voltage signal shows the most effective results while the windowed source current signal shows good leakage reductions but does not show distinctive resonant frequencies.

Fig. 4-45 shows frequency spectrums for Hann windowed voltage and current signals under different power factors (-cos(45°) to cos(45°)) in the TR power system. The windowed V_S signal is most useful to monitoring resonant frequencies under variable power factors, but I_S is hard to read resonant frequencies even it is windowed. These results can be compared with previous case in Fig. 4-36.

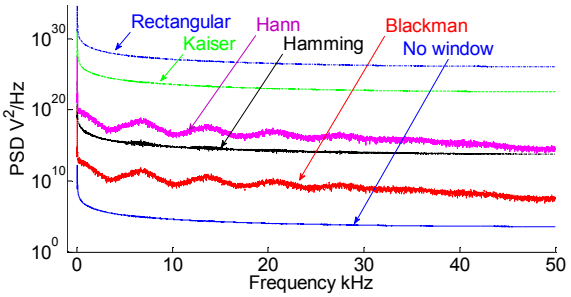

(a) Spectrum of Windowed V_S

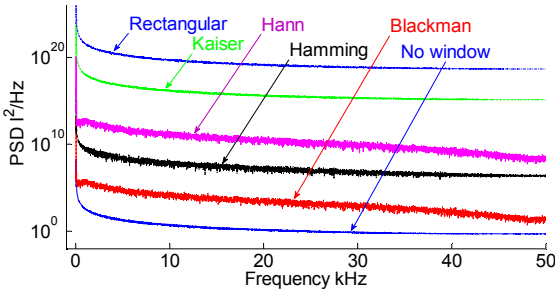

(b) Spectrum of Windowed I_S

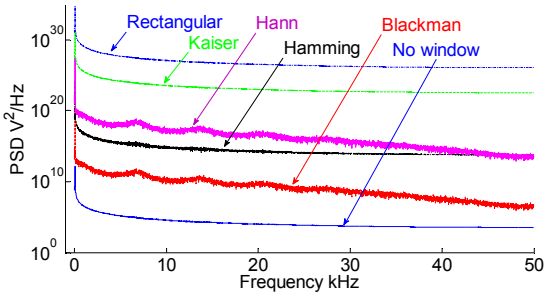

(c) Spectrum of Windowed V_R

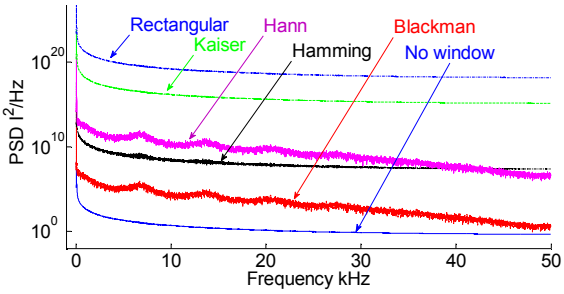

(d) Spectrum of Windowed I_R

Fig. 4-44 Spectrum of Windowed Signals (TR Power System).

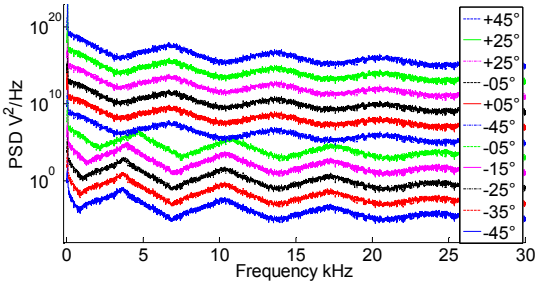

(a) Spectrum of Windowed V_S

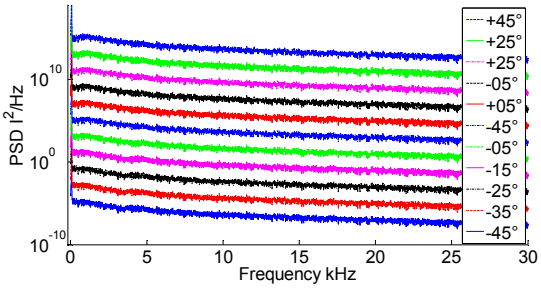

(b) Spectrum of Windowed I_S

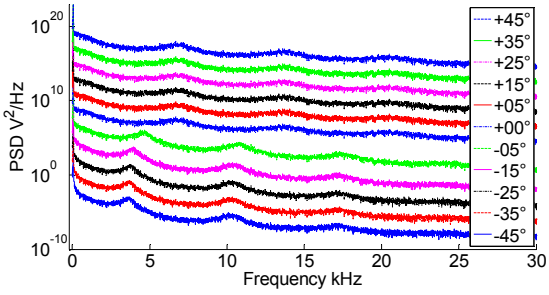

(c) Spectrum of Windowed V_R

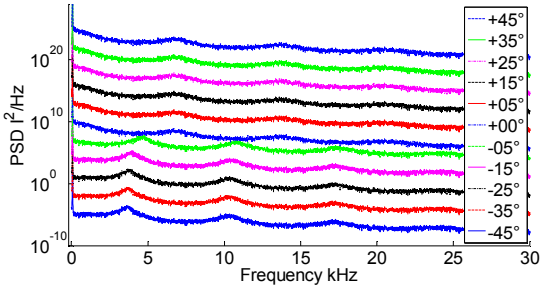

(d) Spectrum of Windowed I_R

Fig. 4-45 Spectrum of Hann Windowed Signals for Various Power Factors (TR Power System).

Also, applying the Hann window function to the fault signals in the TR power system improves resonant frequency discernment as shown in Fig. 4-46. All signals (especially source side signals) from the power system show good features of resonant frequency behaviors in fault positions.

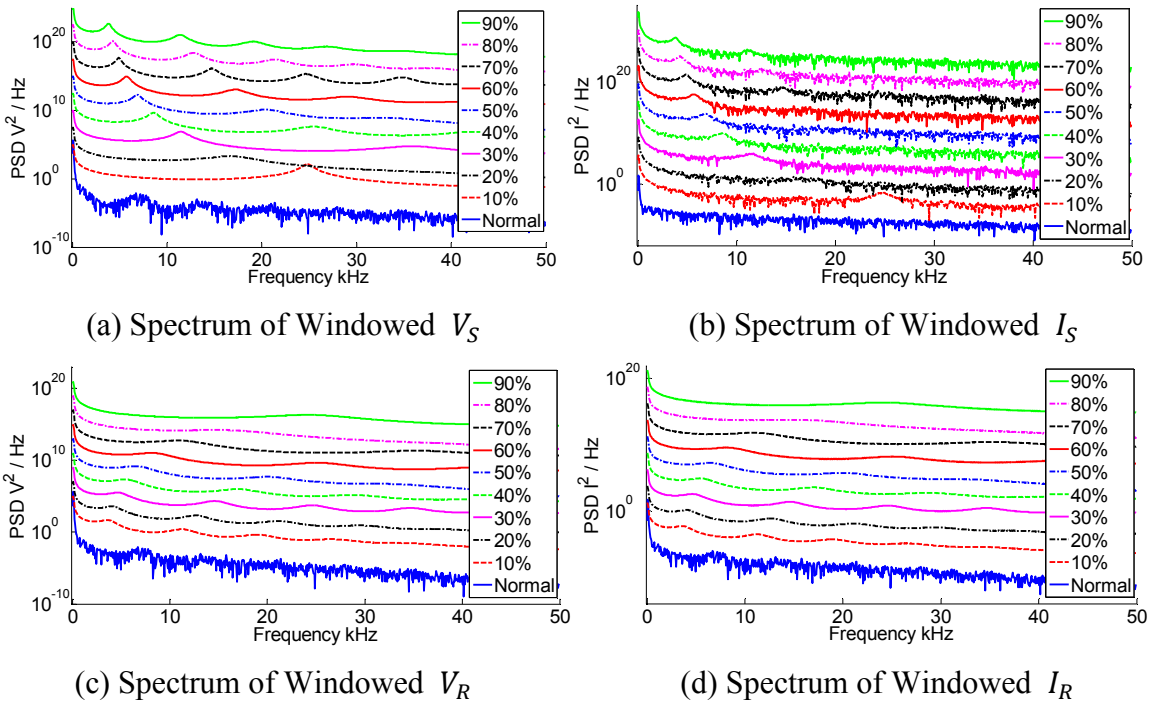

(a) Spectrum of Windowed V_S (b) Spectrum of Windowed I_S

(c) Spectrum of Windowed V_R (d) Spectrum of Windowed I_R

Fig. 4-46 Spectrum of Hann Windowed Signals for Various Fault Locations (TR Power System).

These results verify that the online resonant frequency monitoring can be implemented using power signals at both the source and load sides. The application of a proper window function improves resonant frequency discernment even when the noise is reduced by the TR.

As revealed in the *Westinghouse Transmission and Distribution Reference Book,* 70% of distribution faults are line-to-ground faults [80]. Therefore, the studies of fault condition are primarily focused on the one phase grounding fault. Because all three

phases need to be monitored, the behaviors of resonant frequencies for various fault types (e.g., line-to-line fault, three-phase fault and line-to-line-to-ground fault) including faults on the different phases should be studied as one of future works.

CHAPTER 5

REAL DATA ANALYSIS

This chapter presents the noise level estimation and frequency analyses for real signals from a power plant. The moving average method and variance calculation are used to quantify the noise level. The resonant frequencies in the real signals are identified by power spectral density (PSD) analysis using Matlab. Finally, the results for noise estimation and PSD analysis are discussed from the viewpoint of the application for resonant frequency monitoring in the field.

5.1 Data Selection

The power cable signals (voltage and current) are measured from the potential transformer (PT) and current transformer (CT) at the circuit breaker in the power plant. This circuit breaker is placed on the high voltage side of the TR as was done for the TR power system simulated in PSCAD. Therefore, the measured real signals can be regarded as the source voltage V_S and current I_S in the previous studies. A power analyzer (DEWE-2600-PM-8, manufactured by DEWETRON GmbH) is used for measurement with 2 μs sampling interval and deactivating high frequency filtering.

Fig. 5-1 shows the A-phase voltage and current signals, which are measured during an 8 min 46 second time period. Six parts of the A-phase voltage and current data are selected and named from D1 to D6 as marked with rectangular symbols in Fig. 5-1. D1, D2, D3 are selected from a stable state and D4, D5, D6 are selected from an oscillating state. All selected data have a 4 second length, which contains 240 cycles of 60 Hz signals, and the original signals are used without considering CT and PT ratios.

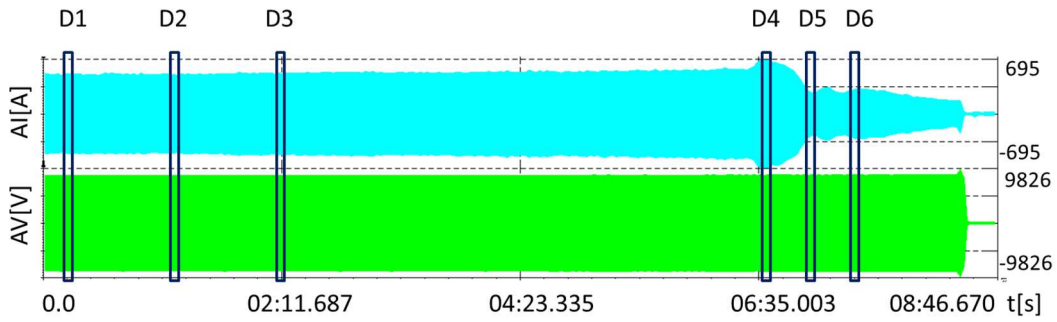

Fig. 5-1. Selected 6 Data Segments in the Voltage (top) and Current (bottom) Signals.

5.2 Noise Level Estimation

In Chapter 4, it was shown that the noise in a signal can play a role as an input testing frequency for resonant frequency analysis. Therefore, it is important to know how much noise the real signal contains.

The noise level is estimated by calculating the averaged square root of the difference between the real signal and an artificial reference signal. This estimation method is similar to the variance concept and the noise level N_L and its standard deviation STD_L are

$$N_L = \frac{1}{\text{npts}} \sum_{n=1}^{\text{npts}} \big(M(n) - R(n)\big)^2 , \qquad STD_L = \sqrt{N_L} \tag{5-1}$$

Where n is a data point, npts is the total number of data points, and $M(n)$ and $R(n)$ are n^{th} datum in the reference and the real signal respectively. The reference signal, MAVG (moving average) is created based on simple moving average process, which calculates a series of averages in adjacent data points from the real signal as,

$$M(n) = \frac{R(n-k) + \cdots + R(n-1) + R(n) + R(n+1) + \cdots + R(n+k)}{2k+1} \qquad (5\text{-}2)$$

where $2k+1$ is an odd integer number for averaging points, and this process repeats several iterations (r) to obtain the best smooth ideal signal. If k is small, the noise will not be removed effectively in the resulting MAVG signal; however, when k is large, the reference signal becomes flatter and more distant from the original signal.

Fig. 5-2 shows current data in the 119th segment (npts = 2^{14}) from D1 and the MAVG signal by the simple moving average process with different numbers of averaging points (k = 3, 5, 20, 100) and iterations (r = 1, 10, 20). In this study, k = 5 and r = 10 are selected since the resulting MAVG signal shows comparatively smoother shape and closer to the real signal. Usually the arrowed point in graph (a) is magnified in graph (b) in this dissertation.

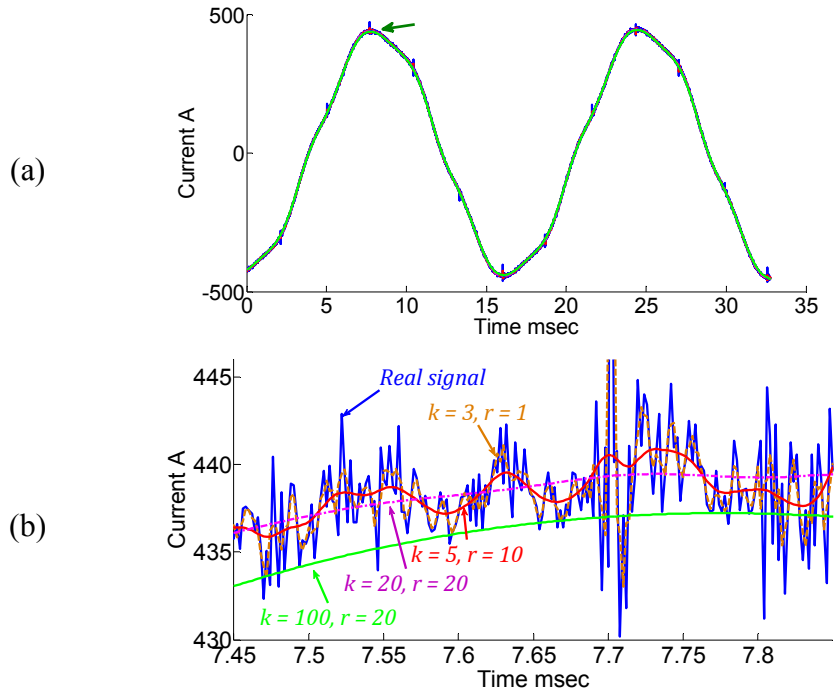

Fig. 5-2. Moving Average with Different Averaging Points and Iterations.

It is helpful to define the percentage of noise standard deviation to the reference signal peak, P_{STD}, which represents the relative noise level to the real signal peak.

$$P_{STD} = \frac{STD_L}{M_{peak}} \tag{5-3}$$

where, M_{peak} is the peak value of reference signal.

The 'MAVG + noise' signal is made by adding 1% noise to this MAVG signal and the 'Sine signal' represents a theoretically perfect 60 Hz sine signal, which best fits to the MAVG signal in their peak values. They are added on the purpose of easy understanding about noise level and distortion of real signals, and Fig. 5-3 shows these signals for 119th segment (npts = 2^{14}) voltage data in D1.

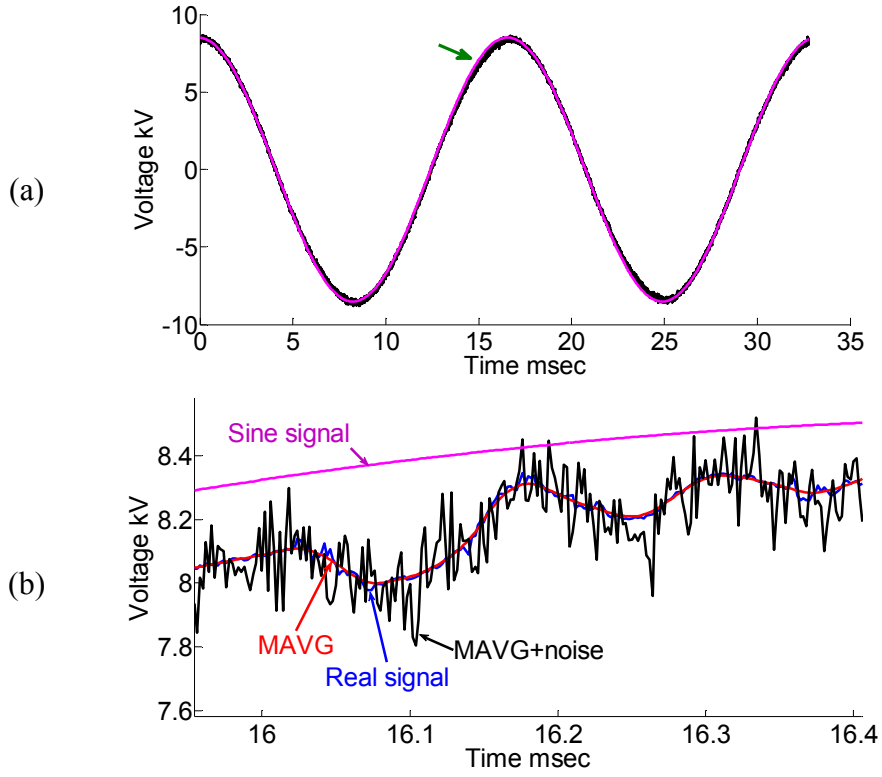

Fig. 5-3. Noise Level Estimation of Real Voltage Signal.

The noise level of this segment is calculated as 128.6 V and some additional values are compared with those of the MAVG + noise signal in Table 5-1.

Table 5-1 Noise Level of 119th Segment in D1 Voltage Data.

Signal	Real signal	MAVG + noise
N_L	128.6 V	7093.3 V
STD_L	$\sqrt{128.6} = 11.4$ V	$\sqrt{7093.3} = 84.2$ V
M_{peak}	8519.2 V	8519.2 V
P_{STD}	11.4 / 8519.2 = 0.13%	84.2 / 8519.2 = 0.99%

Table 5-2 lists noise level estimation results for all voltage and current data from D1 to D6. The noise levels vary from 123 V to 140 V for voltage signals and 4.9 A to 5.5 A for current signals. The P_{STD} is nearly constant for the voltage signals, but it shows considerable changes in the current signals because the current signals have higher variation in peak magnitude. However, stationary noise levels are shown in both the voltage and current signals, but there are relatively higher fluctuations in the current signals than in the stable voltage signals. The 95th segment of Data 5 has the highest P_{STD} as 1.23% as shown in Fig. 5-4.

Table 5-2 Noise Level of Real Data D1 to D6 (npts = 2^{14}).

	Data	D1	D2	D3	D4	D5	D6	Average
Voltage	N_L (V)	126.28	140.36	139.57	144.98	122.54	136.65	135.06
	STD_L (V)	11.24	11.85	11.81	12.04	11.07	11.69	11.62
	M_{peak} (V)	8519.16	8514.46	8516.67	8556.69	8556.23	8614.10	8546.22
	P_{STD} (%)	0.13	0.14	0.14	0.14	0.13	0.14	0.14
Current	N_L (A)	4.98	5.01	5.52	5.32	4.86	5.10	5.13
	STD_L (A)	2.23	2.24	2.35	2.31	2.20	2.26	2.26
	M_{peak} (A)	479.25	451.08	464.89	609.40	207.88	262.89	412.57
	P_{STD} (%)	0.47	0.50	0.51	0.38	1.06	0.86	0.63

(a)

(b)

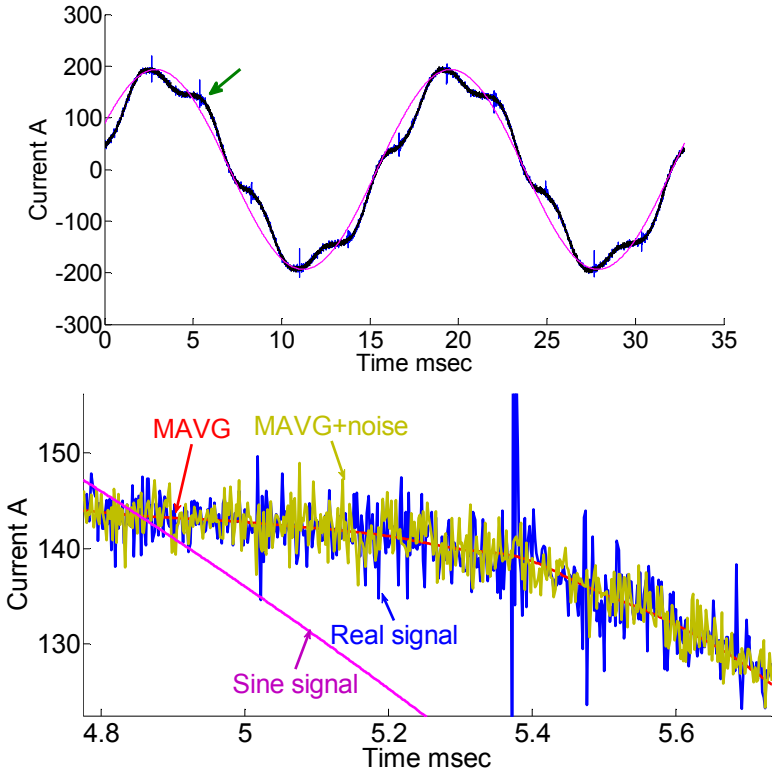

Fig. 5-4 The Highest Noise Level in Real Current Signal.

5.3 Frequency Analysis

The sampling interval (Δt) and the number of data points (npts, N) determine the sampling frequency (f_S) and frequency resolution (Δf);

$$f_S = \frac{1}{\Delta t}, \qquad \Delta f = \frac{f_S}{N} = \frac{1}{N\Delta t} \tag{5-4}$$

All real data have a 2 μs sampling interval, hence the frequency can be analyzed up to 250 kHz (Nyquist frequency, $f_S/2$). When Δt is given, the Δf can be defined by the N; a larger npts provides a higher frequency resolution.

The data are divided into several segments based on the npts and the resulting PSDs from all segments are averaged as the final PSD result. Table 5-3 lists the properties of the data segments for different npts. The number of cycles (N_{cyc}) represents how many cycles of 60 Hz are contained in a segment and N_{seg} denotes number of segments in a data.

Table 5-3 Data Segment Properties for Various npts, Δt = 2 μs.

npts	2^{11}	2^{12}	2^{13}	2^{14}	2^{15}	2^{16}	2^{17}	2^{18}
	2048	4096	8192	16384	32768	65536	131072	262144
N_{cyc}	0.25	0.49	0.98	1.97	3.93	7.86	15.73	31.46
N_{seg}	976	488	244	122	61	30	15	7
Δf (Hz)	244.14	122.07	61.04	30.52	15.26	7.63	3.81	1.91

Fig. 5-5 and Fig. 5-6 show voltage and current PSDs for D5 with different npts (from 2^{12} to 2^{18}). The PSD from 2^{12} data points does not show a useful frequency spectrum, because each segment does not have sufficient frequency resolution.
In contrast, the PSD from 2^{18} data points shows highest frequency resolution, and shows the most detailed frequency spectrum, but it requires longer processing time. However, all spectrums show similar shapes with identical dominant frequency components, which are mostly 60 Hz harmonics except 2^{12} npts case.

(a)

(b)

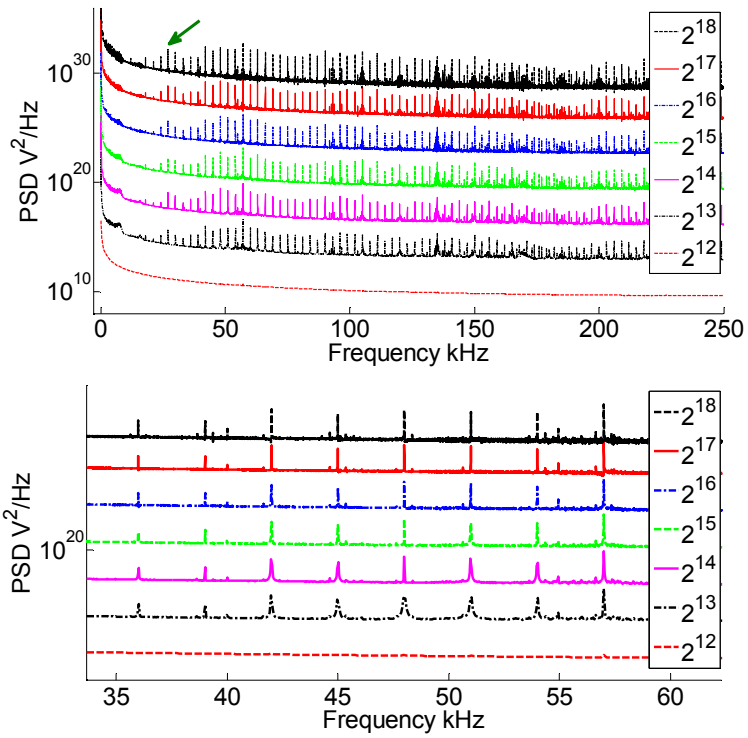

Fig. 5-5 Voltage Signal PSD for Various npts (D5).

(a)

(b)

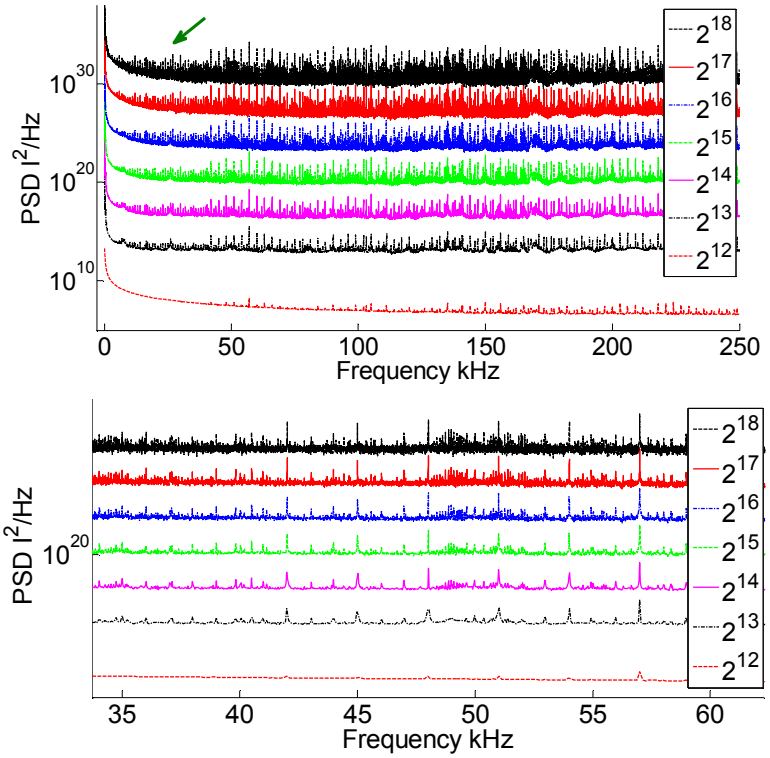

Fig. 5-6 Current Signal PSD for Various npts (D5).

Fig. 5-7 shows the PSD for all data (D1 to D6) with 2^{17} npts. It also can be seen that all data have a similar spectral shape and identical dominant frequency components even though each data has different load conditions.

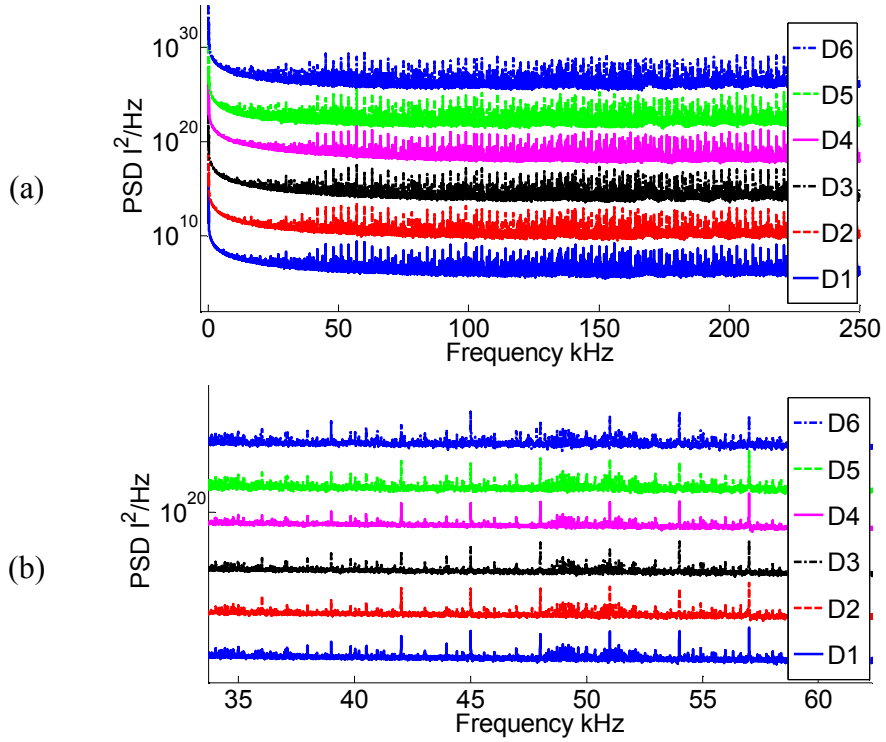

Fig. 5-7 Current Signal PSD for D1 to D6 (npts = 2^{17}).

Table 5-4 lists the frequency analysis elements for the 10 μs sampling interval case, which is 5 times the previous sampling interval case.

Table 5-4 Data Segment Properties for Various npts, Δt = 10 μs.

npts	2^{11}	2^{12}	2^{13}	2^{14}	2^{15}	2^{16}	2^{17}	2^{18}
	2048	4096	8192	16384	32768	65536	131072	262144
N_{cyc}	1.23	2.46	4.92	9.83	19.66	39.32	78.64	157.29
N_{seg}	195	97	48	24	12	6	3	1
Δf (Hz)	48.83	24.21	12.21	6.10	3.05	1.53	0.76	0.38

A comparison of the two different sampling interval cases is illustrated in Fig. 5-8. The longer sampling interval (Δt = 2*5 = 10 μs) data are obtained by taking every 5th point data from the original data (Δt = 2 μs), that is, down sampling the data.

The down sampling (10 μs) case has higher frequency resolution than the original sampling interval (2 μs) case; therefore, the down sampling case shows new frequency components which are hidden in the original sampling interval case. On the other hand, the down sampling case has a narrower frequency bandwidth than the original sampling interval case under the same npts condition. No antialiasing filters are applied during the down sampling process.

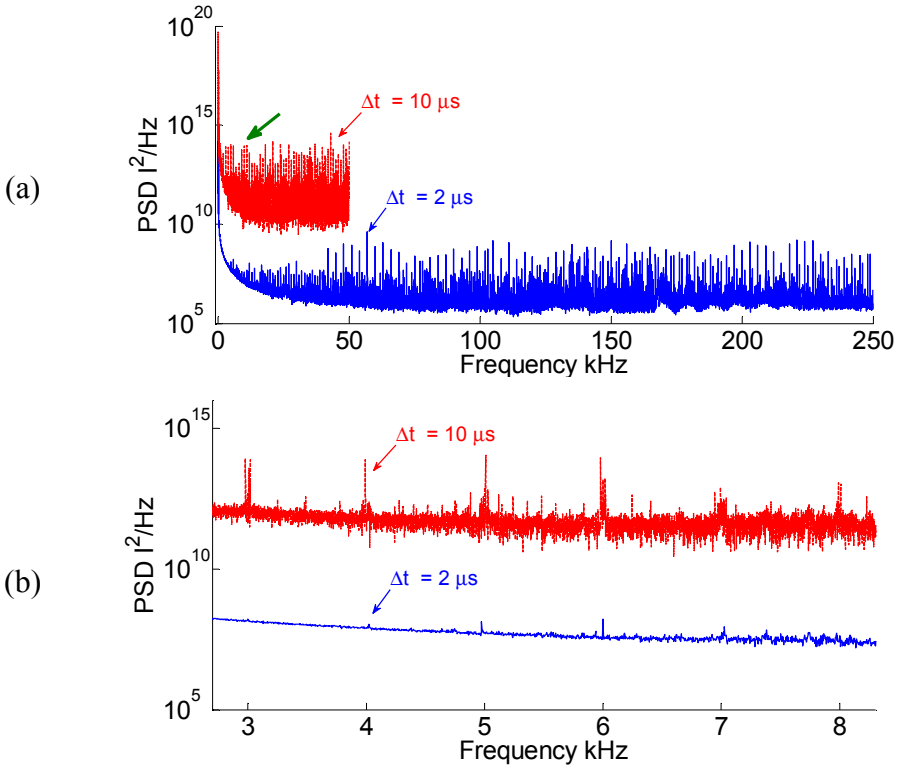

Fig. 5-8 PSD for Different Sampling Intervals (D5, I_S, npts = 2^{17}).

5.4 Validation of Resonant Frequency from Real Signal

This section validates the resonant frequencies in the real signals. Because the real signal contains a lot of unknown frequency components, it is important to extract exact resonant frequency components.

As an effective technique for resonant frequency discrimination, iterative taking 'peaks of peaks' method is used. The '1st step peaks' are peaks that are selected from the signal PSD spectrum then the '2nd step peaks of peaks' selects new peaks from this '1st step peaks' and '3rd step peaks of peaks' selects another new peaks from the '2nd step peaks of peaks'. These processes reduce the number of peaks by removing unnatural small and high peaks and eventually yields a smooth spectrum shape as shown in Fig. 5-9. It can be seen that the peaks of peaks method removes valleys and gives a neatly shaped frequency spectrum with the remaining higher valued dominant frequencies.

(a)

(b)

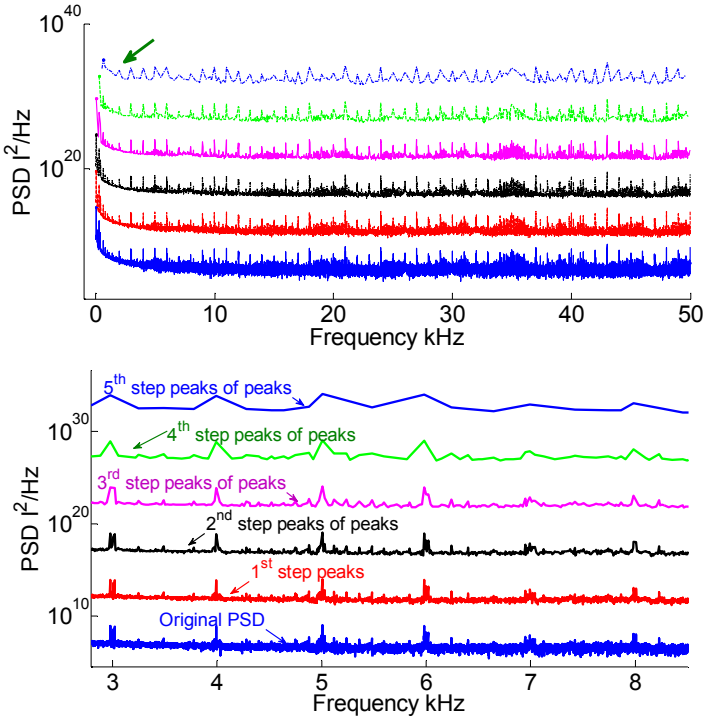

Fig. 5-9 Peaks of Peaks (D5, I_S, npts = 2^{17}).

5.4.1 Real Signal PSD Analysis

Fig. 5-10 shows the PSD analysis for D5 current data with 2^{17} npts. It is very hard to determine the resonant frequency shapes from the original PSD and the 2nd step peaks of peaks, which filtered small peaks from the original PSD shows better shapes, but it is not clear enough to distinguish the resonant frequencies for online monitoring.

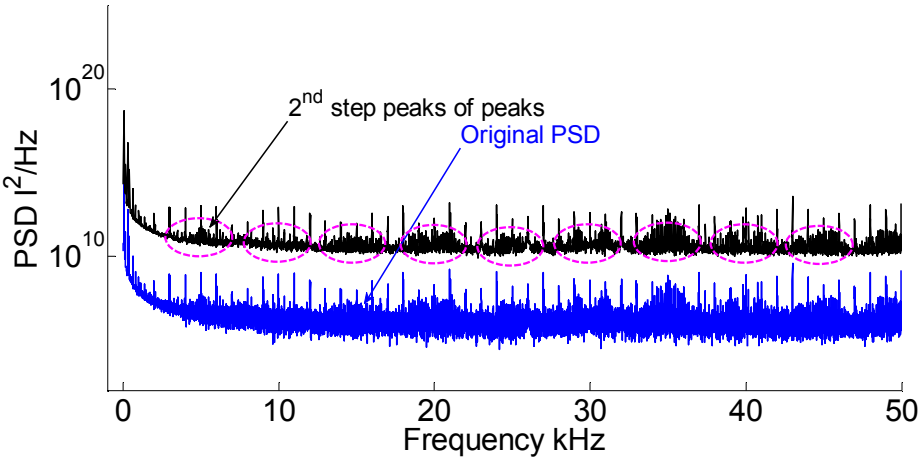

Fig. 5-10 Validation of Resonant Frequency (D5, I_S, Δt = 10 μs, npts = 2^{17}).

When the PSD of the voltage signal from D5 is analyzed, it is extremely hard to discern resonant frequencies even for the 2nd step peaks of peaks case as shown in Fig. 5-11.

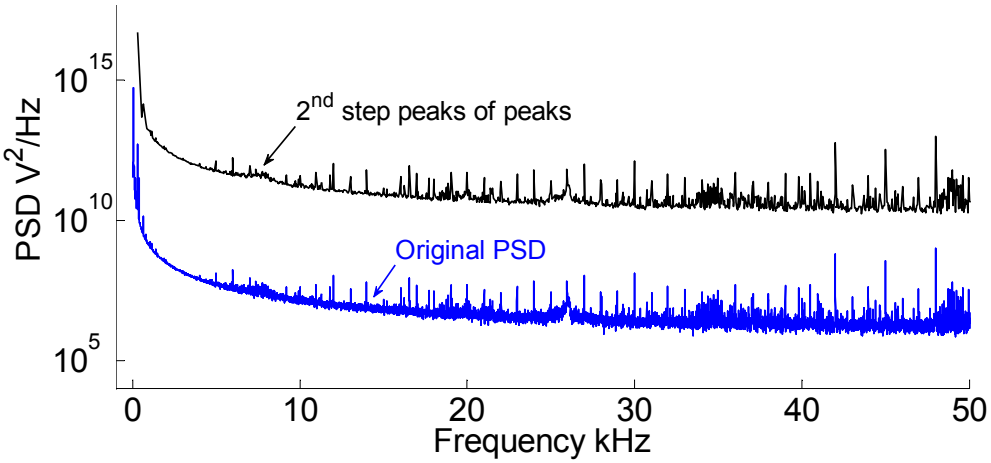

Fig. 5-11 Validation of Resonant Frequency (D5, V_S, Δt = 10 μs, npts = 2^{17}).

Another PSD analysis result for the D5 current with down sampling (Δt = 20 μs) is shown in Fig. 5-12. This case gives a higher frequency resolution, but the frequency bandwidth is reduced from 50 kHz to 25 kHz. Even though the resolution is higher, the discrimination of resonant frequencies is not obvious.

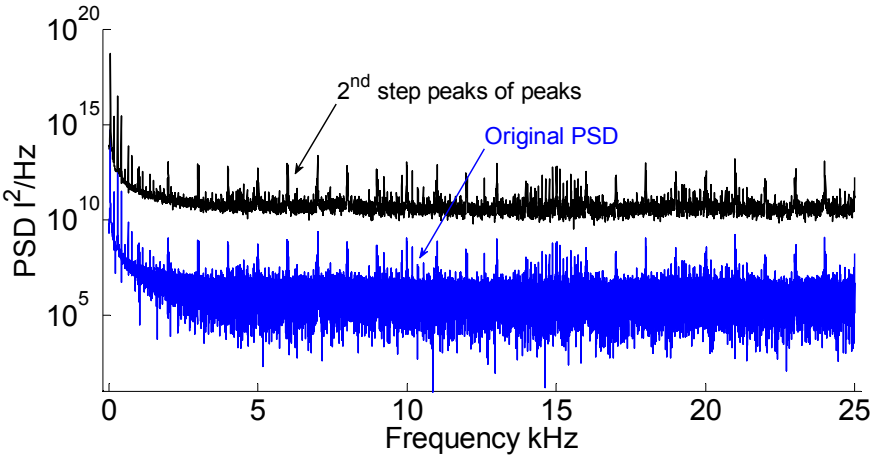

Fig. 5-12 Validation of Resonant Frequency (D5, I_S, Δt = 20 μs, npts = 2^{17}).

5.4.2 Windowing Real Signal

Window functions are applied to the voltage and current signals of D5. The results of PSD analysis for 2^{17} npts are shown in Fig. 5-13 and Fig. 5-14 with 2 μs and 10 μs sampling intervals, respectively.

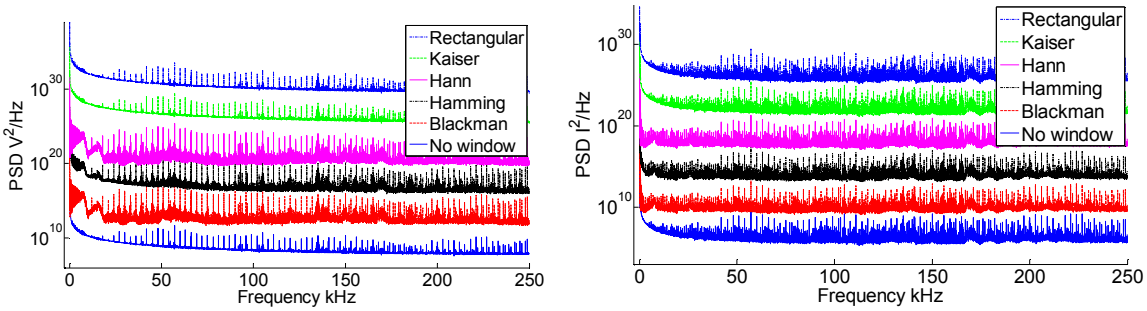

Fig. 5-13 PSD for Windowed Signals (D5, V_S (left), I_S (right), Δt = 2 μs, npts = 2^{17}).

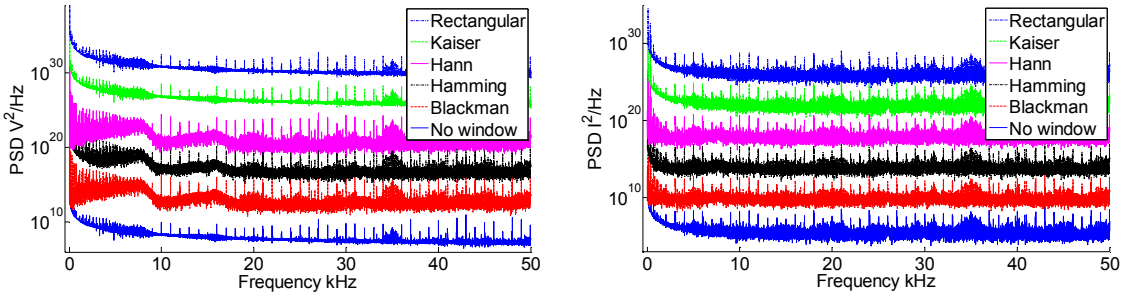

Fig. 5-14 PSD for Windowed Signals (D5, V_S (left), I_S (right), Δt = 10 μs, npts = 2^{17}).

Similar to the simulated signal analysis cases, the Hann, Hamming and Blackman windows functions show better results for the voltage signal.

Considering the shift effect by the transformer (denoted as sft) and the characteristic that the resonant frequencies (denoted as fr) follow an odd order multiple sequence, the frequency spectrum of the TR power system consists of

$$fr + sft, \qquad 3fr + sft, \qquad \dots, \qquad (2n-1)fr + sft \qquad \text{for } n = 1, 2, 3 \dots \tag{5-5}$$

The resonant frequency of power cable and shift can be found by

$$fr = \frac{\{(fr + sft) - (3fr + sft)\}}{2}, \qquad sft = (fr + sft) - fr \tag{5-6}$$

Fig. 5-15 and Fig. 5-16 examine resonant frequencies from the PSD spectrum (npts = 2^{17}) for Hann windowed D5 voltage signal with sampling interval 2 μs and 10 μs, respectively.

To improve resonant frequency distinction, the 'Peak of peak' removes unnatural small and high peaks by comparing neighboring peaks (usually the 3rd step peak of peak provides good results) and the 'Trending' smooths this result using a moving average

method. Finally, the 'Transfer function' describes the ideal resonant frequency shapes using a transfer function that corresponds to the selected resonant frequencies. These methods help to differentiate resonant frequencies and expecting resonant frequencies are marked on the bottom with green bars.

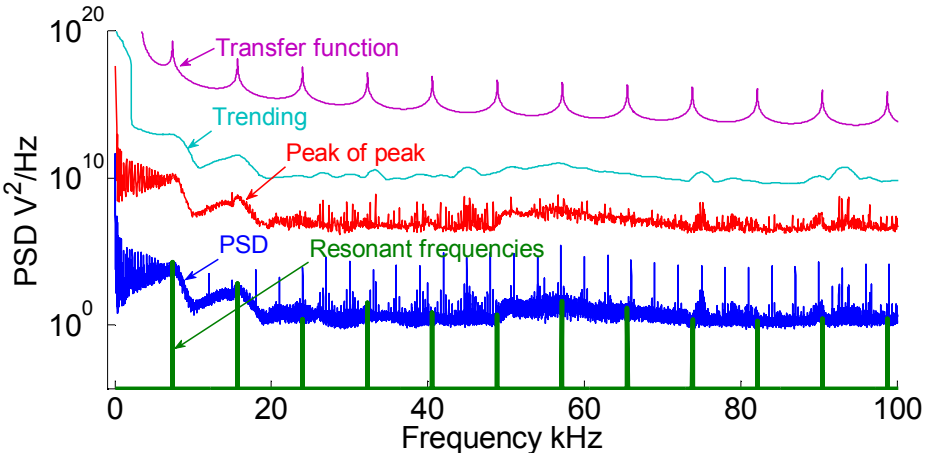

Fig. 5-15 Validation of Resonant Frequencies (V_S, Δt = 2 μs, Hann Window).

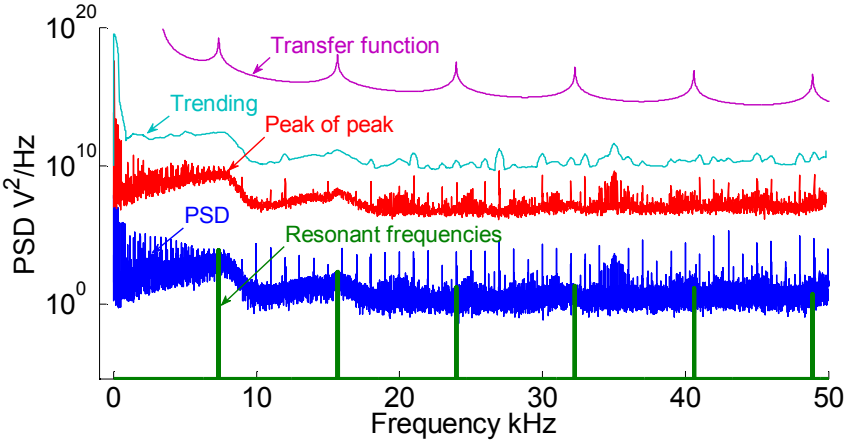

Fig. 5-16 Validation of Resonant Frequencies (V_S, Δt = 10 μs, Hann Window).

The frequencies which are best matching with resonant frequencies shape are 7732 Hz and 15667 Hz. When these frequencies are applied to Eq. (5-6), the first resonant frequency of power cable is 3967 Hz and it is shifted 3765 Hz because of the TR.

The resonant frequencies from the real data are a bit different with those from simulated data (i.e. 6848, 13720 Hz) because the real power system has additional components such as additional impedances in a power plant (generator control unit, indoor TRs, exciter charger, etc.), power cable joints, load conditions in power grid.

As shown in Fig. 5-13 and Fig. 5-14, the resonant frequencies in the windowed current signal are difficult to differentiate and this concurs with the case for the windowed signals in the TR power system simulation of Fig. 4-44 in Chapter 4.

The PSD (npts = 2^{17}) for the Hann windowed D5 V_S and I_S signals are compared in Fig. 5-17. The 2nd segment PSD (2nd V_S and 2nd I_S) is coarser than the Avg V_S and Avg I_S, which are averages of the PSD results for all segments. But they have identical shapes to each other.

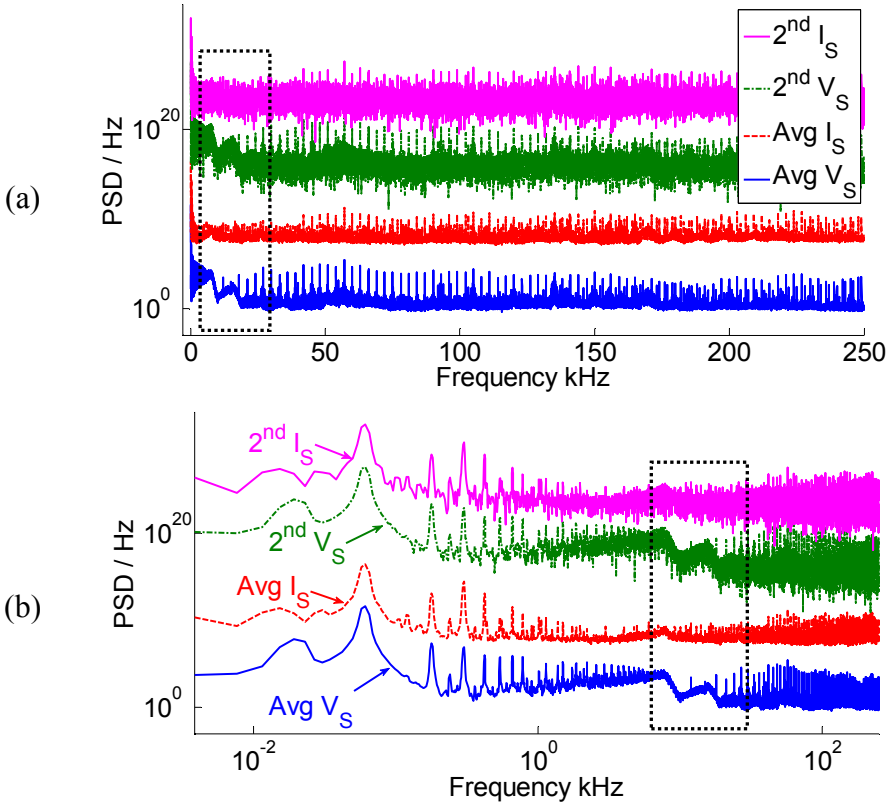

Fig. 5-17 PSD for Windowed V_S and I_S (Δt = 2 μs, Hann Window).

The resonant frequencies are apparent in the voltage signal, but ambiguous in the current signal as shown in Fig. 5-17 (a). These resonant frequencies are more obvious when the frequency axis is log scaled as shown in Fig. 5-17 (b) in which the current signal shows a small peak at the first resonant frequency of 7732 Hz.

A similar comparison is done for the 10 μs sampling interval with the same data. The resonant frequencies are easily found in the windowed voltage signal, but remain hard to find in the windowed current signal even though the frequency resolution is higher.

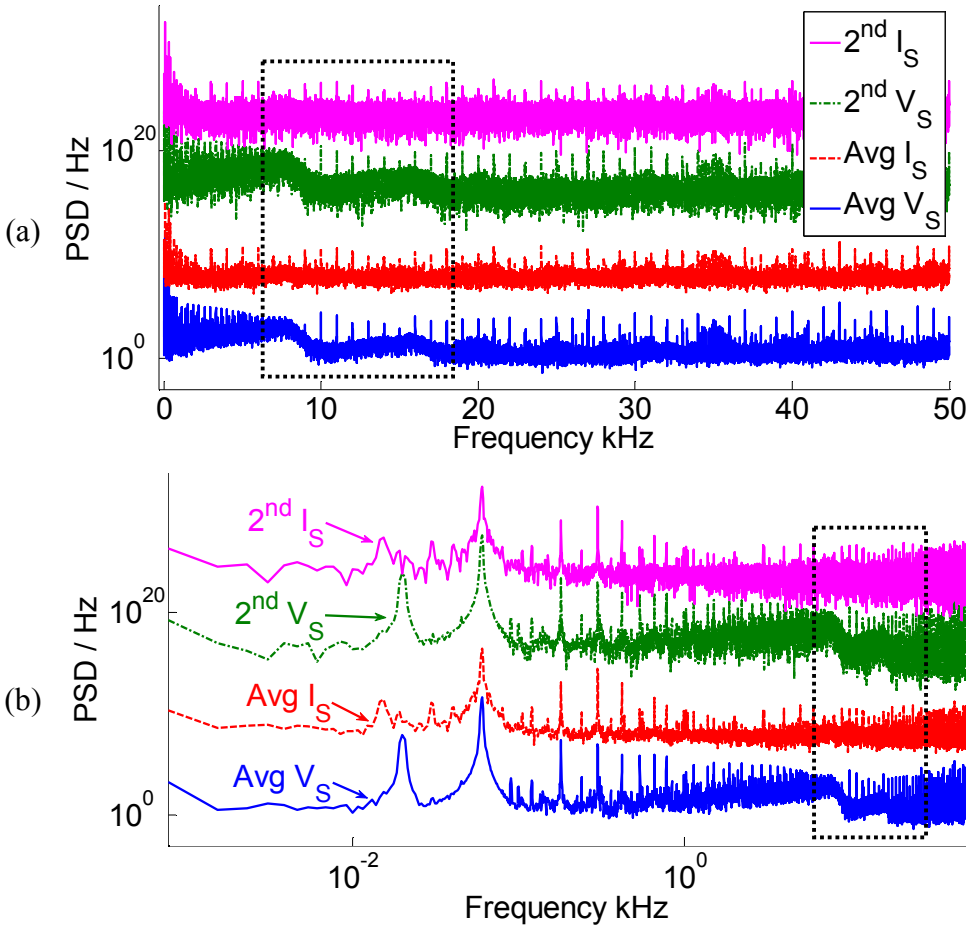

Fig. 5-18 PSD for Windowed V_S and I_S (Δt = 10 μs, Hann Window).

Fig. 5-19 magnifies the low frequency part of Fig. 5-18, and the first peak (100 Hz), which is caused by $\cosh(\gamma l)$ term in Eq. (3-39) in the TR power system can be seen in V_S signal.

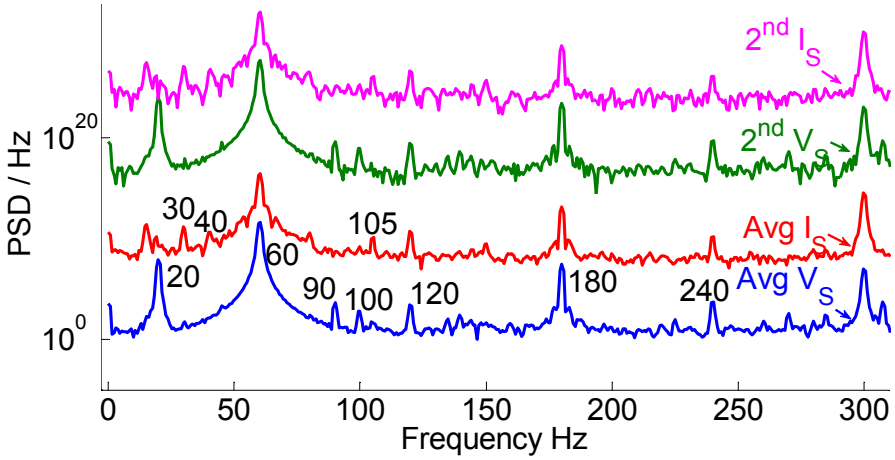

Fig. 5-19 Low Frequency Part in PSD for V_S and I_S (Δt = 10 μs, Hann Window).

The resonant frequencies are examined in all voltage signals in D1 to D6 and compared in Fig. 5-20 and Fig. 5-21. The Hann window is applied to the signals and the PSD is obtained for 2^{17} npts with 2 μs and 10 μs sampling interval, respectively.

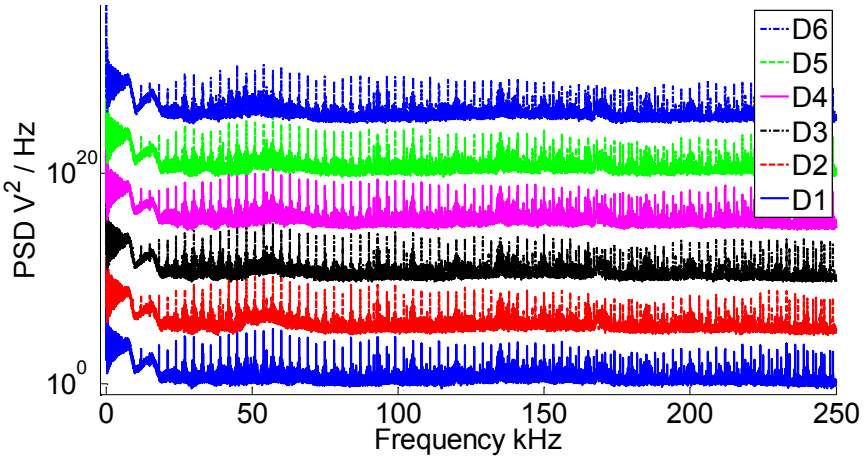

Fig. 5-20 Validation of Resonant Frequencies in All Data (V_S, Δt = 2 μs, Hann Window).

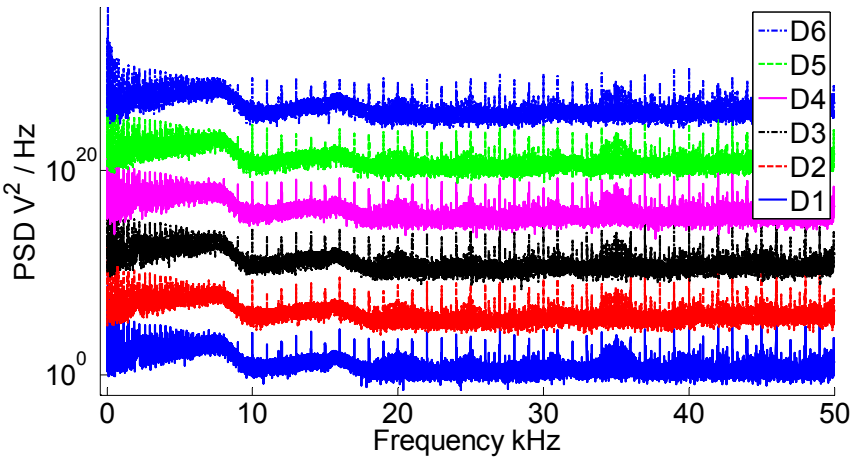

Fig. 5-21 Validation of Resonant Frequencies in All Data (V_S, Δt = 10 μs, Hann Window).

All data show very similar resonant frequencies of 7732 Hz and 15667 Hz and the first and second resonant frequencies for the 2 μs time interval cases are listed in Table 5-5.

Table 5-5 Resonant Frequencies in Real Voltage Data D1 to D6 (npts = 2^{17}).

Data	D1	D2	D3	D4	D5	D6
1st resonant frequency	7740.0	7724.8	7736.2	7721.0	7732.4	7721.0
2nd resonant frequency	15670.8	15529.6	15800.5	15659.3	15667.0	15682.2

The maximum first resonant frequency is 7740 Hz on D1 and the minimum is 7721 Hz on D4 with a difference of 19 Hz. The average first resonant frequency is 7729.2 Hz, and substituting it into the equation for the TR power system resonant frequencies in Eq. (3-40), yields

$$fr_{T1} \cong \frac{1}{2\sqrt{LC}} = 7729.2 \rightarrow \frac{1}{4\sqrt{LC}} \cong 3864.6 \qquad (5\text{-}7)$$

For the given sampling interval (Δt = 2 μs) and number of points (npts = 2^{17}), the frequency resolution Δf is 3.81 Hz from Eq. (5-4). When these values are applied to Eq. (4-4), the maximum fault location error ΔP_{max} is 10.34 m. If 5 kHz is detected as the first new resonant frequency, this indicates a fault at 2389.7 m with accuracy of 6.18 m, and 10 kHz is a fault at 6643.2 m with 1.55 m accuracy, etc.

$$\Delta P_{max} = \left(1 - \frac{3864.6}{3864.6 + 3.81}\right) 10500 = 10.34\ m \tag{5-8}$$

However, considering that all data have different load conditions, these analyses verify the behavior of resonant frequencies for various load conditions. However the resonant frequency is validated in real data using a window function and it proves that the resonant frequency can be monitored in a real power system.

CHAPTER 6

CONCLUSION AND FUTURE WORKS

Effective power cable monitoring and fault location has become one of the most attractive research subjects with increasing power cable usage and request for higher power quality.

This dissertation reviewed several cable diagnosis methods such as Tan δ and partial discharge test. The Tan δ method measures insulation degradation (mainly water trees) in a power cable using the phase difference between the input AC voltage and the resulting current. The partial discharge method detects impulse signals or acoustic waves from partial discharge occurrence. But these methods give information about averaged defects or only about measuring points. Moreover, they give an only good or bad assessment, they require highly experienced skills and suffer from intrinsic tiny measuring signals with noise. The distributed temperature monitoring system, which uses fiber optic is reviewed as a commercialized technique for a power cable monitoring system. But using the temperature to detect original cable defects is difficult because temperature is very dependent on the operational conditions of the power system.

The overview of recent fault location methods is listed in two categories as on-line and off-line data based methods. The off-line methods ensure an accurate result for the fault location with simple principles, but they require time consuming processes and selection of an appropriate method considering the power cable fault types, installation conditions, etc. The on-line methods are fast and do not require cable disconnection from the grid. The impedance based method is the simplest method, but the accuracy is highly

dependent on the transmission system impedance calculation and some assumptions that could be weakened in the real field conditions.

The traveling wave methods are considered as one technique that can improve accuracy of fault location by the signal analysis. The time-frequency domain approach especially will lead to a great improvement in fault location accuracy by performing a detailed frequency analysis without losing time domain resolution, but the extraction of the exact travelling wave and the identification of relative time differences from one or two end signals are still challenging problems to solve.

The partial discharge method locates fault by sensing discharges at susceptible points, but it requires specific sensors to detect tiny signals, high qualified filters to remove ambient noises and highly experienced technicians.

As its main purpose, this dissertation proposes a new passive methodology for power cable monitoring and fault location based on resonant frequency analysis, and its feasibility is studied by theoretical analyses, simulation verifications and real data validations.

As examples of resonant frequency applications, the transformer fault detection method, SFRA, is reviewed. This method measures the resonant frequency of the transformer windings and estimates their defects or deformation by the comparing historical records of measurements. Also, a leakage detection and location method for hydraulic pipe system is described. This method analyzes the change of patterns in the resonant frequencies from the transient pressure signals from valves [81].

We realize that the resonant frequencies of power system can be analyzed from the voltage or current signals when these signals contain sufficient fluctuating noises and this is verified by theoretical calculation using Matlab and PSCAD simulation.

The behavior of the resonant frequency under various load conditions and fault positions were investigated by theoretical analysis and PSCAD simulation based on the installed underground power cable transmission system. It is found that the resonant frequencies are nearly constant under various loads with positive power factors conditions, which can be regarded as the daytime power system operational conditions, but the resonant frequencies can be significantly affected under negative power factor changes such as an overcompensated power factor operation by capacitor banks at nighttime.

The cable fault with a lower fault resistance gives apparent effects on the resonant frequencies by producing new resonant frequencies, which follow odd order multiple sequences of the first resonant frequency. These new resonant frequencies appear in accordance with fault positions and this relationship can be defined as a function of frequency and fault location. On the other hand, the new resonant frequencies are not found for larger fault resistances (i.e., >10 Ω), and this can limit the sensitivity of fault detection.

The TR shifts cable resonant frequencies by an amount equal to the first resonant frequency of the cable, but the behaviors of the resonant frequencies under various load conditions and fault positions are the same as the cable only system.

All resonant frequency characteristics are verified by frequency impedance calculation using PSCAD and frequency analysis of artificial power signals from

simulations. Also spectral window functions are applied to the signal for the sake of improving resonant frequency discernment.

Finally, the resonant frequencies are examined in real signals, which are obtained from the selected sample power plant. First, the noise of the real signals is estimated and it is found that the noises are distributed consistently in both voltage and current signals, but the current signals show relatively higher noise levels because of their higher fluctuations than the voltage signals. However, extraction of the resonant frequencies is accomplished better using the voltage signals than the current signals.

The same resonant frequencies are found in all real voltage data and this proves that the resonant frequency can be monitored and they are stationary in usual load conditions.

We believe that such signature analysis has a promise for application to power systems; hence, the reason for the foundational work presented in this document. When this method is applied to the real power system, it could be an effective, simple and economic online power cable diagnosis and fault location system because it can provide real time cable monitoring and instant fault location using only ordinary power signals.

In summary, we reviewed recent techniques for cable diagnosis and fault location and they still have difficulties for direct online cable defect monitoring and accurate fault locations. As a solution to this, we found that the unique power system resonant frequencies can be derived using the transfer function of an equivalent pi model and it is verified by theoretical analysis.

As a method for the extraction of these resonant frequencies, we proposed the use of the inherent normally distributed noise. This possibility is verified by PSCAD simulation.

We studied the behavior of the resonant frequencies under various load and fault conditions with theoretical analysis and PSCAD simulation. It resulted in that the resonant frequency monitoring can offer an effective diagnosis for the power cable internal parameter changes and the fault positions. Finally the resonant frequencies are validated in real signals from the power cable transmission system in a power plant.

For the practical justification, we may need real data acquired during faults. But the data should not be filtered to remove the needed noise, and the length of power cable or the sampling interval should be sufficient to achieve the monitoring frequency bandwidth. Even obtaining real fault data from the field is extremely hard because the faults do not continuously occur and most protection systems use filters for the preventing malfunction from the noise signal.

The major contributions of this dissertation work include

- A new passive methodology is developed based on resonant frequencies for online cable diagnosis and fault location. This will likely stimulate the frequency analysis scope in power engineering to expand its traditional low frequency range (some hundred Hz for harmonic analysis) to higher frequency range (some tens kHz for resonant frequencies analysis).
- New models for load connection, TR connection and cable fault conditions are applied and verified by theoretical analysis and simulation.

- Utilization of inherent noise in the signal is proposed for resonant frequency analysis and it is verified by computer simulation and analysis of real data.
- The noise level of real signal is estimated using modified method. It compares real signal and reference signal, which is generated by the moving average method.
- For improving resonant frequency discernment, several techniques are introduced such as peak of peaks, trending analysis using the moving average method

Future works can include validation of resonant frequencies behaviors on real fault signals and studies on practical schemes for an online resonant frequency analysis and monitoring system, which will consist of data acquisition, fast frequency analysis, defect or fault recognition and generating events for fault location. Eventually this new methodology should be validated on experimental data or in the field.

REFERENCES

[1] Mejía, Jean Carlos Hernández, Characterization of Real Power Cable Defects by Diagnostic Measurements, Ph.D Dissertation, Georgia Institute of Technology, 2008.

[2] Butler-Purry, K.L.; Cardoso, J., "Characterization of underground cable incipient behavior using time-frequency multi-resolution analysis and artificial neural networks," *Power and Energy Society General Meeting - Conversion and Delivery of Electrical Energy in the 21st Century,* pp. 1-11, July 2008.

[3] Sidhu, T.S.; Xu, Zhihan, "Detection of incipient faults in distribution underground cables," *Transactions on Power Delivery,* vol. 25, pp. 1363-1371, July 2010.

[4] W. Charytoniuk, "Arcing fault detection in underground distribution networks-feasibility study," *IEEE Transactions on Industry Applications,* vol. 36, no. 6, pp. 1756-1761, Dec 2000.

[5] Izykowski, Murari Mohan Saha Jan, Fault Location on Power Networks, Springer London Dordrecht Heidelberg New York, Oct. 2009.

[6] Swift, G.W., "The spectra of fault-induced transients," *IEEE Transactions on Power Apparatus and Systems,* Vols. PAS-98, no. 3, pp. 940-947, May 1979.

[7] Wu, Lin-Yong; He, Zheng-You; Qian, Qing-Quan, "A new single ended fault location technique using travelling wave natural frequencies," in *Power and Energy Engineering Conference, APPEEC*, 2009.

[8] Z. Haifeng, Q. Yulin and J. Huibin, "Medium voltage distribution network traveling wave fault location method based on wavelet packet energy spectrum," vol. 3, pp. 1650-1655, 2011.

[9] IEEE, "Guide for Field Testing and Evaluation of the Insulation of Shielded Power Cable Systems," IEEE Std. 400-2001, Apr. 2002.

[10] R., Bartnikas; Srivastava, K., Power and communication cables: theory and applications, New York, NY: IEEE Series on Power Engineering, 1999.

[11] "PDExplorer® Rel. 1.0 - STANDARD Edition," PRPDA GmbH, Forst Germany, 2013.

[12] Walker, P; Pathak, A.; Boggs, S.;, "Partial discharge XXII: high frequency attenuation in shielded solid dielectric power cable and implications thereof for PD location," *IEEE Electrical Insulation Magazine,* vol. 12, no. 1, pp. 736-743, May/June 2002.

[13] Fauser, E; Hiller, W; Brosche, T;, "Novel characterization of PD signals by real-time measurement of pulse parameters," *IEEE Transactions on Dielectrics and Electrical Insulation,* vol. 6, no. 1, pp. 51-59, Feb. 1999.

[14] Sonneveld, W.; Wiemer, A.; Wezelenburg, M.; Kreuger, F., "Partial discharge part XVIII: errors in the location of partial discharges in high voltage solid dielectric cables," *EEE Electrical Insulation Magazine,* vol. 9, no. 6, pp. 15-22, Nov./Dec. 1993.

[15] Tithi, Fahmida Hossain; Md, M. S. Islam; Tanna, Tawhidul Anwar, "Overview of Stimulated Brillouin Scattering Effect and Various Types of Method to Eliminate this Effect," *International Journal of Computer Applications,* vol. 92, no. 7, pp. 23-26, 2014.

[16] Thevenaz , Luc; Nikles, Marc; Fellay, Alexandre; Facchini, Massimo; Robert, Philippe A., "Truly distributed strain and temperature sensing using embedded optical fibers," in *Smart Structures and Materials*, San Diego, 1998.

[17] Peck, David; Seebacher, Peter, "Distributed Temperature Sensing using Fibre-Optics (DTS Systems)," in *Annual Conference*, Auckland, New Zealand, 2000.

[18] Sensortran, "Application note:transmission & distribution power cable monitoring," SensorTran, Austin, 2011.

[19] Radiodetection, "SPX," [Online]. Available: http://www.radiodetection.com/Document_links.asp?sec_id=2726. [Accessed 6 2 2013].

[20] Agilent Technologies, "Time Domain Reflectometry Theory Application Note 1304-2," Agilent Technologies, May 2005.

[21] Radiodetection,SPX, "Cable and Cable Fault Locating-Part 3," 2003. [Online]. Available: http://www.radiodetection.com/Document_links.asp?sec_id=2726. [Accessed Feb 2013].

[22] Neier, Ing. Tobias, "Cable Fault Location in LV, MV and HV Underground Cable Networks," ETL, Apr. 2009.

[23] Kanoun, O.; Troeltzsch, U.; Qinghai, Shi;, "Detection and localization of cable faults by time and frequency domain measurements," in *Systems Signals and Devices (SSD), 2010 7th International Multi-Conference*, 2010.

[24] JDSU, "FDR - Frequency Domain Reflectometer, manual," JDS Uniphase Corporation, Milpitas, CA, 2000.

[25] Dodds, D.E.;, "Single-Ended FDR to Locate and Specifically Identify DSL Loop Impairments," in *IEEE International Conference Communications, ICC '07.* , 2007.

[26] S.M.Shahrtash, Babak Badrzadeh, "Partial discharge site location in power cables:application to on-line and off-line approach," in *Australasian Universities Power Engineering Conference(AUPEC)2002*, Melbourne, Australia, Oct.2002.

[27] NIASAR, MOHAMAD GHAFFARIAN;, Partial Discharge Signatures of Defects in Insulation Systems Consisting of Oil and Oil-impregnated Paper, Ph.D Dissertation, Stockholm, Sweden : KTH Royal Institute of Technology, Dec. 2012.

[28] Mulroy, P.; Hurtado, A.; Badetz, D., "On-line partial discharge monitoring system for distribution networks," *International Conference on Condition Monitoring and Diagnosis (CMD),* pp. 542 - 545, Sep 2012.

[29] Borghettia, A.; Corsib, S.; Nuccia, C.A.; Paolonea, M.; Perettoa, L.; Tinarellia, R.;, "On the use of continuous-wavelet transform for fault location in distribution power systems," *International Journal of Electrical Power & Energy Systems,* vol. 28, no. 9, p. 608–617, Nov. 2006.

[30] He, Zhengyou; Zhang, Jun; Li, Wei-hua; Lin, Xiangning, "Improved Fault-Location System for Railway Distribution System Using Superimposed Signal," *IEEE Transactions Power Delivery,* vol. 25, no. 3, pp. 1899-1911, July 2010.

[31] Jiang, Zhen; Miao, Shihong; Xu, Hao; Liu, Pei; Zhang, Buhan, "An effective fault location technique for transmission grids using phasor measurement units," *International Journal of Electrical Power & Energy Systems,* vol. 42, no. 1, p. 653–660, November 2012.

[32] Xu, Guoqing; Zhou, Yimin; Chen, Yanfeng, "Model-Based Fault Location with Frequency Domain for Power Traction System," *Energies,* vol. 6, no. 7, pp. 3097-3114, 2013.

[33] Standards, IEEE, IEEE Guide for Determining Fault Location on AC Transmission and Distribution Lines, IEEE PC37.114/D9, 2014, pp. 1-72.

[34] Elhaffar, Abdelsalam Mohamed, Power Transmission Line Fault Location based on Current Travelling Waves, Ph.D Dissertation, Espoo, Finland: Helsinki University of Technology, 2008.

[35] K., Zimmerman; D. , Costello, "Impedance-based fault location experience," in *Rural Electric Power Conference*, 2006.

[36] Evans, R.D.; Wagner, C.F.;, Symmetrical Components, McGraw-Hill, 1933.

[37] Eriksson, Leif, Eriksson; Saha, M.M; Rockefeller, G.D.;, "An Accurate Fault Locator With Compensation For Apparent Reactance In The Fault Resistance Resulting From Remore-End Infeed," *IEEE Transactions Power Apparatus and Systems,* Vols. PAS-104, no. 2, pp. 423-436, Feb. 1985.

[38] Ji, Chaoq, Impedance-based Fault Location Methods for Transmission Line Connecting Wind Farm Plants, MS Dissertation, Clemson University, 2012.

[39] H. Yin and L. Fan, "PMU data-based fault location techniques," in *North American Power Symposium (NAPS)*, Arlington, TX , Sept. 2010.

[40] Z.Q., Bo; G., Weller; F., Jiang; Q.X, Yang, "Application of GPS based fault location scheme for distribution system," in *Power System Technology*, 1998.

[41] "Improved GPS travelling wave fault locator for power cables by using wavelet analysis," *International Journal of Electrical Power & Energy Systems,* vol. 23, no. 5, p. 403–411, June 2001.

[42] Chen, Ping; Xu, Bingyin; Li , Jing, "A Traveling Wave Based Fault Locating System for HVDC Transmission Lines," in *Power System Technology, 2006. PowerCon 2006. International Conference*, 2006.

[43] Clarke, E., “Circuit analysis of AC power systems: symmetrical and related components, New York: Wiley, 1943.

[44] Paithankar, Y.G.; Sant, M.T.;, "A new algorithm for relaying and fault location based on autocorrelation of travelling waves," *Electric Power Systems Research,* vol. 8, no. 2, pp. 179-185, March 1985.

[45] Faybisovich, V.; Khoroshev, M.I.;, "Frequency domain double-ended method of fault location for transmission lines," in *Transmission and Distribution Conference and Exposition*, 2008.

[46] Kim, Chul Hwan, "Wavelet transforms in power systems. Part 1: General introduction to the wavelet transforms," *Power Engineering Journal,* vol. 14, no. 2, pp. 81-87, 2000.

[47] Charytoniuk, W., "Arcing fault detection in underground distribution networks-feasibility study," *IEEE Transactions on Industry Applications,* vol. 36, no. 6, pp. 1756-1761, Dec 2000.

[48] Robertson, D.C.; Camps, O.I.; Mayer, J.S.; Gish, William B.;, "Wavelets and electromagnetic power system transients," *IEEE Transactions on Power Delivery,* vol. 11, no. 2, pp. 1050-1058, 1996.

[49] Shannon, C.E., "A mathematical theory of communication," *Bell System Technical Journal,* vol. 27, no. 3, pp. 379-423, 1948.

[50] Baseer, Mohammad Abdul, "Travelling waves for finding the fault location in transmission lines," *Electrical and Electronic Engineering,* vol. 1, no. 1, pp. 1-19, 2013.

[51] Memon, Aslam Pervez; Uqail, Muhammad Aslam; Memon, Zubair Ahmed, "Combined Approach of PNN and Time-Frequency as the Classifier for Power System Transient Problems," *Mehran University Research Journal of Engineering & Technology,* vol. 32, no. 4, 2013.

[52] Lee, Pedro J; Vítkovský, John P. ; Lambert, Martin F.; Simpson, Angus R.; Liggett, James A., "Leak Detection in Pipelines Using an Inverse Resonance Method," in *Environmental and Water Resources Systems Analysis (EWRSA) symposium*, Virginia, USA, 2002.

[53] Leea, Pedro J.; Vítkovskýa, John P.; Lamberta, Martin F.; Simpsona, Angus R.; Liggettb, James A., "Leak location using the pattern of the frequency response diagram in pipelines: a numerical study," *Sound and Vibration,* vol. 284, no. 3–5, p. 1051–1073, June 2005.

[54] Lee, Pedro J.; Vítkovský, John P.; Lambert, Martin F.; Simpson, Angus R.; Liggett, James A., "Frequency Domain Analysis for Detecting Pipeline Leaks," *Journal of Hydraulic Engineering,* vol. 131, no. 7, pp. 596-604, July 2005.

[55] Ryder, S.A.;, "Transformer diagnosis using frequency response analysis: results from fault simulation," in *Power Engineering Society Summer Meeting*, Chicago, 2002.

[56] Kraetge, A.; Krüger, M.; Velásquez, J. L.;, "Aspects of the Practical Application of Sweep Frequency Response Analysis (SFRA) on Power Transformers," in *6'th Southern Africa Regional Conference*, 2009.

[57] Islam, Asif; Khan, Shahidul Islam; Hoque, Aminul, "Detection of Mechanical Deformation in Old Aged Power Transformer Using Cross Correlation Co-Efficient Analysis Method," *Energy and Power Engineering,* vol. 3, no. 4, pp. 585-591, September 2011.

[58] George G., Karady; Keith E., Holbert;, Electrical Energy Conversion and Transport 2nd edition, Hoboken, New Jersey: John Wiley & Sons, Inc., Aug.2013.

[59] Nasser Tleis, in *Power Systems Modelling and Faults Analysis:Theory and Practice*, Elsevier Ltd, 2008.

[60] Llorente Garcia, David; Gudmundsdottir, Unnur Stella, Analysis of overvoltages caused by resonance in the energized high voltage network, University of Zaragoza, Polytechnic Center, 2010.

[61] Haginomori, Eiichi, Applied ATP-EMTP to Highly-sophisticated Electric Power Ssystems, Tokyou Institute of Technology and Kyushu Institute of Technology, August 2003.

[62] Kang, Lin; Keith E., Holbert;, "Applying the equivalent pi circuit to the modeling of hydraulic pressurized lines," *Mathematics and Computers in Simulation,* vol. 79, no. 7, p. 2064–2075, March 2009.

[63] Amornvipas, C.; Hofmann, L.;, "Resonance analyses in transmission systems: Experience in Germany," in *Power and Energy Society General Meeting*, 2010.

[64] Xu, Wilsun; Huang, Zhenyu; Cui, Yu; Wang, Haizhen, "Harmonic resonance mode analysis," *IEEE Transactions on Power Delivery ,* vol. 20, no. 2, pp. 1182-1190, April 2005.

[65] Rauma, K.; Md Hasan, K.N.; Gavriluta, C.; Citro, C.;, "Resonance analysis of a wind power plant with modal approach," in *Industrial Electronics (ISIE), 2012 IEEE International Symposium*, 2012.

[66] Md Hasan, K.N; Kalle, Rauma; Alvaro, Luna; J. Ignacio, Candela; Rodriguez, P.;, "Harmonic Resonance Study for Wind Power Plant," in *International Conference on Renewable Energies and Power Quality*, Santiago de Compostela (Spain), 2012.

[67] "Modeling and simulation of the propagation of harmonics in electric power networks. I. Concepts, models, and simulation techniques," *IEEE Transactions on Power Delivery,* vol. 11, no. 1, pp. 452-465, Jan. 1996.

[68] Mohaddes, Mojtaba; Annakkage, Udaya, "Northwest Transmission Line Project Construction Power Study," British Columbia Transmission Corporation, 2008.

[69] Juan A. Martinez-Velasco, Power System Transients: Parameter Determination, CRC Press, Oct 14, 2009.

[70] Craig Muller, P.Eng. Software Development Manager, USER'S GUIDE on the use of PSCAD, Manitoba Canada: Manitoba HVDC Research Centre, Feb, 2010.

[71] Craig Muller, P.Eng. Software Development Manager, Applications of PSCAD ® / EMTDC ™, Manitoba Canada: Manitoba HVDC Research Centre, 2007.

[72] Y. Gong, M. M. Mynam, . A. Guzmán and G. Benmouyal, "Automated Fault Location System for Nonhomogeneous Transmission Networks," in *2012 65th Annual Conference for Protective Relay Engineers*, College Station, TX, April 2012.

[73] Fred, Rieke; William, Bialek; David, Warland;, Spikes: Exploring the Neural Code (Computational Neuroscience), MIT Press, 1999.

[74] S. Millers and D. Childers, Probability and Random Processes, Academic Press, 2012, p. 370–375.

[75] Kay, Steven M.;, Intuitive Probability and Random Processes using MATLAB, Kingston: Springer, 2005.

[76] Pleite, J. ; Valdivia., V; Zumel, P; Gonzalez, C., "Transformer and Series Inductance Integration for Harmonic Filtering in PWM Inverters Based in a Simple Design Procedure," in *IEEE International Symposium on Industrial Electronics*, Vigo, 2007.

[77] LDS AN014, "Understanding FFT Windows application note," LDS an SPX company, 2008.

[78] Cimbala, John M., Introduction to Mechanical Engineering Measurements, Penn State University, 2011.

[79] S. Steven W, The Scientist and Engineer's Guide to Digital Signal Processing, California: California Technical Publishing, 1997.

[80] Holbert, Keith E.; Karady, George G.;, Electrical Energy Conversion and Transport: An Interactive Computer-Based Approach, John Wiley & Sons, May, 2013.

[81] Lee, P.J.; Vítkovský, J.P.; Lambert, M.F.; Simpson, A.R.; Liggett, J.A., "Leak location using the pattern of the frequency response diagram in pipelines: a numerical study," *Journal of Sound and Vibration,* vol. 284, pp. 1051-1073, 2005.

[82] Keith E., Holbert; Ryan M., Wilding;, "Leak Detection, Isolation and Characterization Using a Pressure Sensing Line Frequency Response Function," *Seventh American Nuclear Society International Topical Meeting on Nuclear Plant Instrumentation,* pp. 775-785, 22-26 July 2012.

APPENDIX A

RESONANT FREQUENCIES IN CABLE POWER SYSTEM

From Fig. 3-5, the line impedance and capacitive reactance are

$$z = R_x + j\omega L_x, \qquad y = j\omega C_x$$

The voltage loop equation and current node point equation using the equivalent circuit are

$$\frac{d}{dx}V_o(x) = z \cdot I(x), \qquad \frac{d}{dx}I(x) = y \cdot V_o(x)$$

Taking the derivative of the first equation and substituting the second equation into the first one results in:

$$\frac{d^2}{dx^2}V_o(x) = \frac{d}{dx}\left(\frac{d}{dx}V_o(x)\right) = \frac{d}{dx}\big(z \cdot I(x)\big) = z \cdot y \cdot V_o(x) \tag{1}$$

The solution is

$$V_o(x) = A_1 e^{\gamma x} + A_2 e^{-\gamma x}, \qquad \gamma = \sqrt{z \cdot y} = \sqrt{(R_x + j\omega L_x)j\omega C_x} = \alpha + j\beta$$

Where, γ is the propagation constant, α is the attenuation constant (Np/m), and β is the phase constant (rad/m). The current can be calculated from Eq. (1).

$$I(x) = \frac{1}{z}\left(\frac{d}{dx}V_o(x)\right) = \frac{1}{z}\left[\frac{d}{dx}(A_1 e^{\gamma x} + A_2 e^{-\gamma x})\right] = \frac{\gamma}{z}(A_1 e^{\gamma x} + A_2 e^{-\gamma x})$$

The derivation of the surge or characteristic impedance is

$$Z_c = \frac{z}{\gamma} = \frac{z}{\sqrt{z \cdot y}} = \sqrt{\frac{z^2}{z \cdot y}} = \sqrt{\frac{z}{y}} = \sqrt{\frac{1}{j\omega C_x}(R_x + j\omega L_x)}$$

$$I(x) = \frac{(A_1 e^{\gamma x} + A_2 e^{-\gamma x})}{Z_c}$$

The boundary conditions are: $I(0) = I_R,\ V_o(0) = V_R$

$$A_2 = V_R - A_1, \qquad I_R Z_c = A_1 - V_R + A_1$$

$$V_o(0) = A_1 e^{\gamma \cdot 0} + A_2 e^{-\gamma \cdot 0}, \qquad I(x) = \frac{(A_1 e^{\gamma \cdot 0} + A_2 e^{-\gamma \cdot 0})}{Z_c}$$

$$V_R = A_1 + A_2, \qquad I(x) = \frac{A_1 + A_2}{Z_c}$$

$$A_2 = V_R - A_1, \qquad I_R Z_c = A_1 - V_R + A_2$$

$$A_1 = \frac{V_R + I_R Z_c}{2}, \qquad A_2 = V_R - \frac{V_R + I_R Z_c}{2} = \frac{V_R - I_R Z_c}{2}$$

The voltage equation is

$$V_o(x) = A_1 e^{\gamma x} + A_2 e^{-\gamma x} = \frac{V_R + I_R Z_c}{2} e^{\gamma x} + \frac{V_R - I_R Z_c}{2} e^{-\gamma x}$$

$$V_o(x) = V_R \left(\frac{e^{\gamma x} + e^{-\gamma x}}{2}\right) + (I_R Z_c)\left(\frac{e^{\gamma x} - e^{-\gamma x}}{2}\right) = V_R \cosh(\gamma x) + I_R Z_c \sinh(\gamma x)$$

The current equation is

$$I(x) = \frac{(A_1 e^{\gamma x} + A_2 e^{-\gamma x})}{Z_c} = \frac{\frac{V_R + I_R Z_c}{2} e^{\gamma x} - \frac{V_R - I_R Z_c}{2} e^{-\gamma x}}{Z_c}$$

$$I(x) = \frac{V_R}{Z_c}\left(\frac{e^{\gamma x} + e^{-\gamma x}}{2}\right) + I_R\left(\frac{e^{\gamma x} + e^{-\gamma x}}{2}\right) = \frac{V_R}{Z_c}\sinh(\gamma x) + I_R\cosh(\gamma x)$$

The transmission line equations are

$$V_o(x) = V_R\cosh(\gamma x) + Z_c I_R\sinh(\gamma x)$$

$$I(x) = \frac{V_R}{Z_c}\sinh(\gamma x) + I_R\cosh(\gamma x)$$

Where l is the length of transmission system, and its ABCD parameters are

$$\begin{bmatrix} A & B \\ C & D \end{bmatrix} = \begin{bmatrix} \cosh(\gamma l) & Z_c\sinh(\gamma l) \\ \frac{\sinh(\gamma l)}{Z_c} & \cosh(\gamma l) \end{bmatrix}$$

The equivalent circuit for a transmission line is shown in Fig. 3-6, which called as equivalent pi (π) model. The ABCD parameters of this equivalent pi model are

$$\begin{bmatrix} A' & B' \\ C' & D' \end{bmatrix} = \begin{bmatrix} 1 + \frac{Z'Y_1'}{2} & Z' \\ \frac{Z'Y_1'Y_2' + 2Y_1' + 2Y_2'}{4} & 1 + \frac{Z'Y_1'}{2} \end{bmatrix}$$

Let $zl = Z,\ yl = Y$.

$$Z_S = Z' = Z_c\sinh(\gamma l) = \sqrt{\frac{z}{y}}\sinh(\gamma l) = zl\frac{\sinh(\gamma l)}{l\sqrt{yz}} = Z\frac{\sinh(\gamma l)}{\gamma l}$$

$$\frac{1}{Z_P} = \frac{Y_1'}{2} = \frac{Y_2'}{2} = \frac{1}{Z_c}\frac{\cosh(\gamma l) - 1}{\sinh(\gamma l)} = \frac{1}{Z_c}\tanh\left(\frac{\gamma l}{2}\right)$$

$$= \sqrt{\frac{y}{z}}\tanh\left(\frac{\gamma l}{2}\right) = \frac{\gamma l}{2}\frac{\tanh\left(\frac{\gamma l}{2}\right)}{\frac{l}{2}\sqrt{yz}} = \frac{Y}{2}\frac{\tanh\left(\frac{\gamma l}{2}\right)}{\frac{\gamma l}{2}}$$

These equations give the voltage and current distribution along the line. The transfer function for transmission line voltage can be expressed as

$$\frac{V_R}{V_S} = \frac{\frac{2}{Y'}}{Z' + \frac{2}{Y'}} = \frac{Z_P}{Z_S + Z_P}$$

Again,

$$Z_S = Z_C \sinh(\gamma l), \qquad Z_P = \frac{Z_C}{\tanh\left(\frac{\gamma l}{2}\right)}$$

$$\frac{V_R}{V_S} = \frac{\frac{Z_C}{\tanh\left(\frac{\gamma l}{2}\right)}}{Z_C \sinh(\gamma l) + \frac{Z_C}{\tanh\left(\frac{\gamma l}{2}\right)}} = \frac{\frac{1}{\tanh\left(\frac{\gamma l}{2}\right)}}{\sinh(\gamma l) + \frac{1}{\tanh\left(\frac{\gamma l}{2}\right)}}$$

$$= \frac{\frac{\cosh\left(\frac{\gamma l}{2}\right)}{\sinh\left(\frac{\gamma l}{2}\right)}}{\sinh(\gamma l) + \frac{\cosh\left(\frac{\gamma l}{2}\right)}{\sinh\left(\frac{\gamma l}{2}\right)}} = \frac{\frac{\cosh\left(\frac{\gamma l}{2}\right)}{\sinh\left(\frac{\gamma l}{2}\right)}}{2\sinh\left(\frac{\gamma l}{2}\right)\cosh\left(\frac{\gamma l}{2}\right) + \frac{\cosh\left(\frac{\gamma l}{2}\right)}{\sinh\left(\frac{\gamma l}{2}\right)}}$$

$$= \frac{\frac{1}{\sinh\left(\frac{\gamma l}{2}\right)}}{2\sinh\left(\frac{\gamma l}{2}\right) + \frac{1}{\sinh\left(\frac{\gamma l}{2}\right)}} = \frac{1}{2\sinh^2\left(\frac{\gamma l}{2}\right) + 1}$$

$$= \frac{\frac{1}{\sinh\left(\frac{\gamma l}{2}\right)}}{2\sinh\left(\frac{\gamma l}{2}\right) + \frac{1}{\sinh\left(\frac{\gamma l}{2}\right)}} = \frac{1}{2\sinh^2\left(\frac{\gamma l}{2}\right) + 1}$$

$$= \frac{1}{\cosh(\gamma l)} = \frac{1}{\cosh\left(l\sqrt{(R_x + j\omega L_x)j\omega C_x}\right)} \tag{2}$$

Using the cable length, each component is

$$R = R_x l, \qquad L = L_x l, \qquad C = C_x l$$

Finally, the transfer function for cable power system H_C is,

$$H_C = \frac{V_R}{V_S} = \frac{1}{\cosh\left(\sqrt{(R + j\omega L)j\omega C}\right)}$$

It can be expressed in the s-domain as

$$H_C(s) = \frac{V_R(s)}{V_S(s)} = \frac{1}{\cosh\left(\sqrt{(R + sL)sC}\right)} \tag{3}$$

The resonant peak frequencies of this model are the roots of the denominator of Eq. (3).

To solve for the roots of the hyperbolic cosine function, assume that

$$\sqrt{(R+sL)sC} = jq \tag{4}$$

The denominator of Eq. (3) can then be written as

$$\cosh\left(\sqrt{(R+sL)sC}\right) = \cosh(jq) = \cos(q)$$

Solving $\cos(q) = 0$, the roots are

$$q_n = \frac{(2n-1)\pi}{2}, \qquad n = 1, 2, 3, \ldots \tag{5}$$

Substituting Eq. (5) into Eq. (4), the poles are identified as

$$\sqrt{(R+sL)sC} = j\frac{(2n-1)\pi}{2} \implies LCs^2 + RCs + \left(\frac{(2n-1)\pi}{2}\right)^2 = 0$$

Solving this,

$$s_{Cn} = \frac{-RC \pm \sqrt{R^2C^2 - 4LC\left(\frac{(2n-1)\pi}{2}\right)^2}}{2LC}$$

$$= -\frac{R}{2L} \pm \sqrt{\frac{R^2}{4L^2} - \frac{LC\left((2n-1)\pi\right)^2}{4L^2C^2}}$$

$$= -\frac{R}{2L} \pm j\frac{1}{2}\sqrt{\frac{\left((2n-1)\pi\right)^2}{LC} - \frac{R^2}{L^2}}, \qquad n = 1, 2, 3, \ldots$$

Typically, $1/(L_xC_x) \gg (R_x/L_x)^2$, such that the approximate roots are

$$s_{Cn} \cong -\frac{R}{2L} \pm j\frac{(2n-1)\pi}{2\sqrt{LC}}, \qquad n = 1, 2, 3, \ldots \tag{6}$$

The resonant peak appears when the frequency is equal to the imaginary part of Eq. (6). Therefore, the approximate resonant peak frequencies of the exact sensing line model can be expressed as [62]

$$\omega_{Cn} \cong \frac{(2n-1)\pi}{2\sqrt{LC}}, \qquad n = 1, 2, 3, \ldots$$

$$fr_{Cn} \cong \frac{(2n-1)}{4\sqrt{LC}}, \qquad n = 1, 2, 3, \ldots$$

APPENDIX B

RESONANT FREQUENCIES IN LOAD CONNECTED CABLE POWER SYSTEM

From the equivalent circuit for the load connected power cable system in Fig. 3-7, the series and parallel impedances are

$$Z_S = Z_C \sinh(\gamma l), \qquad Z_P = \frac{Z_C}{\tanh\left(\frac{\gamma l}{2}\right)}$$

The transfer function for the load connected cable power system is

$$H_{CL} = \frac{V_R}{V_S} = \frac{\frac{Z_P Z_L}{Z_P + Z_L}}{Z_S + \frac{Z_P Z_L}{Z_P + Z_L}}$$

$$= \frac{\frac{Z_P Z_L}{Z_P + Z_L}}{\frac{Z_S(Z_P + Z_L) + Z_P Z_L}{Z_P + Z_L}} = \frac{Z_P Z_L}{Z_S Z_P + Z_S Z_L + Z_P Z_L}$$

$$= \frac{1}{\frac{Z_S Z_P + Z_S Z_L + Z_P Z_L}{Z_P Z_L}} = \frac{1}{\frac{Z_S}{Z_L} + \frac{Z_S}{Z_P} + 1}$$

$$= \frac{1}{\frac{Z_C \sinh(\gamma l)}{Z_L} + \frac{\frac{Z_C \sinh(\gamma l)}{Z_C}}{\tanh\left(\frac{\gamma l}{2}\right)} + 1}$$

$$= \frac{1}{\frac{Z_C \sinh(\gamma l)}{Z_L} + \sinh(\gamma l)\tanh\left(\frac{\gamma l}{2}\right) + 1}$$

$$= \frac{1}{\frac{Z_C \sinh(\gamma l)}{Z_L} + \sinh(\gamma l)\left(\frac{\cosh(\gamma l) - 1}{\sinh(\gamma l)}\right) + 1}$$

$$= \frac{1}{\frac{Z_C \sinh(\gamma l)}{Z_L} + \cosh(\gamma l) - 1 + 1} = \frac{1}{\frac{1}{Z_L} Z_c \sinh(\gamma l) + \cosh(\gamma l)}$$

Again, the transfer function for a load connected cable power system is

$$H_{CL} = \frac{V_R}{V_S} = \frac{1}{\frac{1}{Z_L} Z_c \sinh(\gamma l) + \cosh(\gamma l)} \tag{7}$$

APPENDIX C

RESONANT FREQUENCIES IN FAULTED CABLE POWER SYSTEM

From the system model for faulted cable power system in Fig. 3-13, the fault position p in ratio to cable length as $0 < p < 1$

Let, $a = \gamma pl, \quad b = \gamma(1-p)l$

$$a + b = \gamma l, \quad a - b = \gamma(2p-1)l, \quad b - a = \gamma(1-2p)l$$

$$Z_{S1} = Z_C \sinh(\gamma pl) = Z_C \sinh(a)$$

$$Z_{P1} = \frac{2}{Y_1'} = \frac{1}{\frac{1}{Z_c}\tanh\left(\frac{\gamma pl}{2}\right)} = \frac{Z_c}{\tanh\left(\frac{\gamma pl}{2}\right)} = \frac{Z_c}{\tanh\left(\frac{a}{2}\right)}$$

$$Z_{S2} = Z_C \sinh(\gamma(1-p)l) = Z_C \sinh(b)$$

$$Z_{P2} = \frac{2}{Y_2'} = \frac{Z_c}{\tanh\left(\frac{\gamma(1-p)l}{2}\right)} = \frac{Z_c}{\tanh\left(\frac{b}{2}\right)}$$

The transfer function is

$$\frac{V_R}{V_S} = \frac{\frac{1}{\frac{1}{Z_{P1}} + \frac{1}{Z_{P2}} + \frac{1}{R_F} + \frac{1}{Z_{S2}+Z_{P2}}}}{Z_{S1} + \frac{1}{\frac{1}{Z_{P1}} + \frac{1}{R_F} + \frac{1}{Z_{P2}} + \frac{1}{Z_{S2}+Z_{P2}}}} \frac{Z_{P2}}{Z_{S2}+Z_{P2}}$$

$$= \frac{\frac{Z_{P2}}{Z_{S2}+Z_{P2}}}{Z_{S1}\left(\frac{1}{Z_{P1}} + \frac{1}{Z_{P2}} + \frac{1}{R_F} + \frac{1}{Z_{S2}+Z_{P2}}\right) + 1}$$

$$= \frac{\dfrac{\dfrac{Z_c}{\tanh\left(\frac{b}{2}\right)}}{Z_C \sinh(b) + \dfrac{Z_c}{\tanh\left(\frac{b}{2}\right)}}}{Z_C \sinh(a)\left(\dfrac{1}{\dfrac{Z_c}{\tanh\left(\frac{a}{2}\right)}} + \dfrac{1}{\dfrac{Z_c}{\tanh\left(\frac{b}{2}\right)}} + \dfrac{1}{R_F} + \dfrac{1}{Z_C \sinh(b) + \dfrac{Z_c}{\tanh\left(\frac{b}{2}\right)}}\right) + 1}$$

$$= \frac{\dfrac{\dfrac{Z_c}{\tanh\left(\frac{b}{2}\right)}\tanh\left(\frac{b}{2}\right)}{Z_c\left(1 + \tanh\left(\frac{b}{2}\right)\sinh(b)\right)}}{Z_C \sinh(a)\left(\dfrac{\tanh\left(\frac{a}{2}\right)}{Z_c} + \dfrac{\tanh\left(\frac{b}{2}\right)}{Z_c} + \dfrac{1}{R_F} + \dfrac{\tanh\left(\frac{b}{2}\right)}{Z_c\left(1 + \tanh\left(\frac{b}{2}\right)\sinh(b)\right)}\right) + 1}$$

$$= \frac{\dfrac{1}{1 + \tanh\left(\frac{b}{2}\right)\sinh(b)}}{\sinh(a)\left(\tanh\left(\frac{a}{2}\right) + \tanh\left(\frac{b}{2}\right) + \dfrac{Z_c}{R_F} + \dfrac{\tanh\left(\frac{b}{2}\right)}{1 + \tanh\left(\frac{b}{2}\right)\sinh(b)}\right) + 1}$$

$$= \frac{\dfrac{1}{1 + \tanh\left(\frac{b}{2}\right)2\sinh\left(\frac{b}{2}\right)\cosh\left(\frac{b}{2}\right)}}{\sinh(a)\left(\tanh\left(\frac{a}{2}\right) + \tanh\left(\frac{b}{2}\right) + \dfrac{Z_c}{R_F} + \dfrac{\tanh\left(\frac{b}{2}\right)}{1 + \tanh\left(\frac{b}{2}\right)2\sinh\left(\frac{b}{2}\right)\cosh\left(\frac{b}{2}\right)}\right) + 1}$$

$$= \frac{\dfrac{1}{1 + 2\sinh^2\left(\frac{b}{2}\right)}}{\sinh(a)\left(\tanh\left(\frac{a}{2}\right) + \tanh\left(\frac{b}{2}\right) + \dfrac{Z_c}{R_F} + \dfrac{\tanh\left(\frac{b}{2}\right)}{1 + 2\sinh^2\left(\frac{b}{2}\right)}\right) + 1}$$

$$= \frac{\frac{1}{\cosh(b)}}{\sinh(a)\left(\tanh\left(\frac{a}{2}\right) + \tanh\left(\frac{b}{2}\right) + \frac{Z_c}{R_F} + \frac{\tanh\left(\frac{b}{2}\right)}{\cosh(b)}\right) + 1}$$

$$= \frac{\frac{1}{\cosh(b)}}{\sinh(a)\tanh\left(\frac{a}{2}\right) + \sinh(a)\tanh\left(\frac{b}{2}\right) + \frac{Z_c}{R_F}\sinh(a) + \frac{\sinh(a)\tanh\left(\frac{b}{2}\right)}{\cosh(b)} + 1}$$

$$= \frac{\frac{1}{\cosh(b)}}{2\sinh\left(\frac{a}{2}\right)\cosh\left(\frac{a}{2}\right)\frac{\sinh\left(\frac{a}{2}\right)}{\cosh\left(\frac{a}{2}\right)} + \sinh(a)\tanh\left(\frac{b}{2}\right) + \frac{Z_c}{R_F}\sinh(a) + \frac{\sinh(a)\tanh\left(\frac{b}{2}\right)}{\cosh(b)} + 1}$$

$$= \frac{\frac{1}{\cosh(b)}}{2\sinh^2\left(\frac{a}{2}\right) + 1 + \frac{Z_c}{R_F}\sinh(a) + \sinh(a)\tanh\left(\frac{b}{2}\right) + \frac{\sinh(a)\tanh\left(\frac{b}{2}\right)}{\cosh(b)}}$$

$$= \frac{\frac{1}{\cosh(b)}}{\cosh(a) + \frac{Z_c}{R_F}\sinh(a) + \sinh(a)\tanh\left(\frac{b}{2}\right) + \frac{\sinh(a)\tanh\left(\frac{b}{2}\right)}{\cosh(b)}}$$

$$= \frac{1}{\cosh(a)\cosh(b) + \frac{Z_c}{R_F}\sinh(a)\cosh(b) + \sinh(a)\tanh\left(\frac{b}{2}\right)\cosh(b) + \sinh(a)\tanh\left(\frac{b}{2}\right)}$$

$$= \frac{1}{\cosh(a)\cosh(b) + \frac{Z_c}{R_F}\sinh(a)\cosh(b) + \sinh(a)\tanh\left(\frac{b}{2}\right)(\cosh(b) + 1)}$$

$$= \frac{1}{\cosh(a)\cosh(b) + \frac{Z_c}{R_F}\sinh(a)\cosh(b) + \sinh(a)\tanh\left(\frac{b}{2}\right)2\cosh^2\left(\frac{b}{2}\right)}$$

$$= \frac{1}{\cosh(a)\cosh(b) + \frac{Z_c}{R_F}\sinh(a)\cosh(b) + \sinh(a)\frac{\sinh\left(\frac{b}{2}\right)}{\cosh\left(\frac{b}{2}\right)}2\cosh^2\left(\frac{b}{2}\right)}$$

$$= \frac{1}{\cosh(a)\cosh(b) + \frac{Z_c}{R_F}\sinh(a)\cosh(b) + \sinh(a)\,2\sinh\left(\frac{b}{2}\right)\cosh\left(\frac{b}{2}\right)}$$

$$= \frac{1}{\cosh(a)\cosh(b) + \frac{Z_c}{R_F}\sinh(a)\cosh(b) + \sinh(a)\sinh(b)}$$

$$= \frac{1}{\frac{1}{2}(\cosh(\mathrm{a}+\mathrm{b}) + \cosh(\mathrm{a}-\mathrm{b})) + \frac{1}{2}(\cosh(\mathrm{a}+\mathrm{b}) - \cosh(\mathrm{a}-\mathrm{b})) + \frac{Z_c}{R_F}\sinh(a)\cosh(b)}$$

$$= \frac{1}{\cosh(\mathrm{a}+\mathrm{b}) + \frac{Z_c}{R_F}\frac{1}{2}(\sinh(\mathrm{a}+\mathrm{b}) + \sinh(\mathrm{a}-\mathrm{b}))}$$

$$= \frac{1}{\cosh(\gamma l) + \frac{Z_c}{2R_F}(\sinh(\gamma l) + \sinh(\gamma(2p-1)l))} \qquad (8)\ [82]$$

$$= \frac{1}{\cosh(\gamma l) + \frac{Z_c}{2R_F}2\sinh(p\gamma l)\cosh(\gamma l - p\gamma l)}$$

$$= \frac{1}{\cosh(\gamma l) + \frac{Z_c}{R_F}\sinh(p\gamma l)\cosh(\gamma(1-p)l)} \qquad (9)$$

Considering the denominator in Eq. (8), the first term $\cosh(\gamma l)$ gives same solution as the fault-free condition, and the second term determines new resonant frequencies for fault conditions. The second term is

$$\sinh(p\gamma l)\cosh(\gamma(1-p)l) \tag{10}$$

Let the first part in Eq. (10) be zero,

$$\sinh(p\gamma l) = 0 \tag{11}$$

Converting to the s-domain, and let this be

$$\sinh\left(p\sqrt{(R+sL)sC}\right) = \cosh(jq) = \cos(q) = 0$$

$$q_n = n\pi, \qquad n = 1, 2, 3, \ldots$$

Solving this,

$$p\sqrt{(R+sL)sC} = jn\pi \Longrightarrow LCs^2 + RCs + \left(\frac{n\pi}{p}\right)^2 = 0$$

$$s_{1CFn} = \frac{-RC \pm \sqrt{R^2C^2 - 4LC\left(\frac{n\pi}{p}\right)^2}}{2LC} = -\frac{R}{2L} \pm \sqrt{\frac{R^2}{4L^2} - \frac{4LC(n\pi)^2}{4L^2C^2p^2}}$$

$$= -\frac{R}{2L} \pm j\frac{1}{2}\sqrt{\frac{4(n\pi)^2}{LCp^2} - \frac{R^2}{L^2}}, \qquad n = 1, 2, 3, \ldots$$

Typically, $1/(L_xC_x) \gg (R_x/L_x)^2$, such that the approximate roots are

$$s_{1CFn} \cong -\frac{R}{2L} \pm j\frac{n\pi}{p\sqrt{LC}}, \qquad n = 1, 2, 3, \ldots \tag{12}$$

The approximate new resonant frequencies for the faulted cable power system is

$$\omega_{1CFn} \cong \frac{n\pi}{p\sqrt{LC}}, \qquad fr_{1CFn} \cong \frac{n}{2p\sqrt{LC}} \tag{13}$$

Next, let the second part in Eq. (10) be zero

$$\cosh(\gamma(1-p)l) = 0$$

In a similar way,

$$\cosh\left((1+p)\sqrt{(R+sL)sC}\right) = \cosh(jq) = \cos(q) = 0$$

$$q_n = \frac{(2n-1)\pi}{2}, \qquad n = 1, 2, 3, \ldots$$

$$(1+p)\sqrt{(R+sL)sC} = j\frac{(2n-1)\pi}{2} \Longrightarrow LCs^2 + RCs + \left(\frac{(2n-1)\pi}{2(1-p)}\right)^2 = 0$$

$$s_{2CFn} = \frac{-RC \pm \sqrt{R^2C^2 - 4LC\left(\frac{(2n-1)\pi}{2(1-p)}\right)^2}}{2LC}$$

$$= -\frac{R}{2L} \pm \sqrt{\frac{R^2}{4L^2} - \frac{LC\left((2n-1)\pi\right)^2}{4L^2C^2(1-p)^2}}$$

$$= -\frac{R}{2L} \pm j\frac{1}{2}\sqrt{\frac{\left((2n-1)\pi\right)^2}{LC(1-p)^2} - \frac{R^2}{L^2}}, \qquad n = 1, 2, 3, \ldots$$

Typically, $1/(L_x C_x) \gg (R_x/L_x)^2$, such that the approximate roots are

$$s_{2CFn} \cong -\frac{R}{2L} \pm j\frac{(2n-1)\pi}{2\sqrt{LC}(1-p)}, \qquad n = 1, 2, 3, \ldots \tag{14}$$

The approximate new resonant frequencies for a faulted cable power system are

$$\omega_{2CFn} \cong \frac{(2n-1)\pi}{2\sqrt{LC}(1-p)}, \qquad fr_{2CFn} \cong \frac{(2n-1)}{4\sqrt{LC}(1-p)} \tag{15}$$

APPENDIX D

RESONANT FREQUENCIES IN TRANSFORMER CONNECTED POWER SYSTEM

From the equivalent circuit for the TR connected power system in Fig. 3-14,

$$Z_{TR} = R_{TR} + j\omega L_{TR}$$

Let, $\quad H_{S1} = \dfrac{Z_P}{Z_S + Z_P}$

The equivalent impedance, Z_{E1} is

$$Z_{E1} = \frac{1}{\frac{1}{Z_S + Z_P} + \frac{1}{Z_P}} = \frac{Z_P}{\frac{Z_P}{Z_S + Z_P} + \frac{Z_P}{Z_P}} = \frac{Z_P}{H_{S1} + \frac{Z_P}{Z_P}} = \frac{Z_P Z_P}{Z_P H_{S1} + Z_P}$$

$$H_T = \frac{V_R}{V_S} = \frac{Z_{E1}}{Z_{TR} + Z_{E1}} \frac{Z_P}{Z_S + Z_P} = \frac{Z_{E1}}{Z_{TR} + Z_{E1}} H_{S1}$$

$$= \frac{\frac{Z_P Z_P}{Z_P H_{S1} + Z_P}}{Z_{TR} + \frac{Z_P Z_P}{Z_P H_{S1} + Z_P}} H_{S1} = \frac{Z_P Z_P}{Z_{TR}(Z_P H_{S1} + Z_P) + Z_P Z_P} H_{S1}$$

$$= \frac{Z_P}{Z_{TR}(H_{S1} + 1) + Z_P} H_{S1} = \frac{\frac{Z_C}{\tanh\left(\frac{\gamma l}{2}\right)}}{Z_{TR}\left(\frac{1}{\cosh(\gamma l)} + 1\right) + \frac{Z_C}{\tanh\left(\frac{\gamma l}{2}\right)}} \frac{1}{\cosh(\gamma l)}$$

$$= \frac{Z_C}{Z_{TR} \tanh\left(\frac{\gamma l}{2}\right)\left(\frac{1}{\cosh(\gamma l)} + 1\right) + Z_C} \frac{1}{\cosh(\gamma l)}$$

$$= \frac{Z_C}{Z_{TR} \tanh\left(\frac{\gamma l}{2}\right)\left(\frac{1}{\cosh(\gamma l)} + 1\right) + Z_C} \frac{1}{\cosh(\gamma l)}$$

$$= \frac{Z_C}{Z_{TR}\tanh\left(\frac{\gamma l}{2}\right)(1+\cosh(\gamma l)) + Z_C\cosh(\gamma l)}$$

$$= \frac{Z_C}{Z_{TR}\tanh\left(\frac{\gamma l}{2}\right)2\cosh^2\left(\frac{\gamma l}{2}\right) + Z_C\cosh(\gamma l)}$$

$$= \frac{Z_C}{Z_{TR}\frac{\sinh\left(\frac{\gamma l}{2}\right)}{\cosh\left(\frac{\gamma l}{2}\right)}2\cosh^2\left(\frac{\gamma l}{2}\right) + Z_C\cosh(\gamma l)}$$

$$= \frac{Z_C}{Z_{TR}2\sinh\left(\frac{\gamma l}{2}\right)\cosh\left(\frac{\gamma l}{2}\right) + Z_C\cosh(\gamma l)}$$

$$= \frac{Z_C}{Z_{TR}\sinh(\gamma l) + Z_C\cosh(\gamma l)} = \frac{1}{\frac{Z_{TR}}{Z_C}\sinh\left(l\sqrt{zy}\right) + \cosh\left(l\sqrt{zy}\right)}$$

Again,

$$H_T = \frac{V_R}{V_S} = \frac{1}{\frac{Z_{TR}}{Z_c}\sinh(\gamma l) + \cosh(\gamma l)} \tag{16}$$

Because $Z_{TR}\frac{1}{Z_c}\sinh(\gamma l) \gg \cosh(\gamma l)$, then the transfer function can be simplified as

$$\frac{V_R}{V_S} = \frac{1}{Z_{TR}\frac{1}{Z_c}\sinh(\gamma l)} \tag{17}$$

By similar way with the previous solution in Eq. (11),

$$\gamma l = l\sqrt{yz} = jp$$

$$\sinh\left(l\sqrt{yz}\right) = \sinh(jp) = j\sin(p) = 0$$

In the s-domain,

$$l\sqrt{yz} = \sqrt{(R + sL)sC} = jn\pi, \qquad n = 1, 2, 3, \ldots$$

$$(R + sL)sC + (n\pi)^2 = LCs^2 + RCs + (n\pi)^2 = 0$$

Solving this,

$$s_{Tn} = \frac{-RC \pm \sqrt{R^2C^2 - 4LC(n\pi)^2}}{2LC} = -\frac{R}{2L} \pm \sqrt{\frac{R^2C^2}{4L^2C^2} - \frac{4LC(n\pi)^2}{4L^2C^2}}$$

$$= -\frac{R}{2L} \pm \sqrt{\frac{R^2}{4L^2} - \frac{4(n\pi)^2}{4LC}} = -\frac{R}{2L} \pm j\frac{1}{2}\sqrt{\frac{(2n\pi)^2}{LC} - \frac{R^2}{L^2}}, \qquad n = 1, 2, 3, \ldots$$

Typically, $1/(L_xC_x) \gg (R_x/L_x)^2$, such that the approximate resonant frequencies are

$$s_{Tn} \cong -\frac{R}{2L} \pm i\frac{2n\pi}{2\sqrt{LC}}, \qquad n = 1, 2, 3, \ldots \tag{18}$$

$$\omega_{Tn} \cong \frac{n\pi}{\sqrt{LC}}, \qquad f_{Tn} \cong \frac{n}{2\sqrt{LC}}, \qquad n = 1, 2, 3, \ldots \tag{19}$$